QUANTITATIVE STUDY OF SPIN HALL EFFECTS IN MESOSCOPIC THIN FILMS

by

Chuan Qin

A dissertation submitted to the Faculty of the University of Delaware in partial fulfillment of the requirements for the degree of Doctor of Philosophy in Physics

Fall 2017

QUANTITATIVE STUDY OF SPIN HALL EFFECTS IN MESOSCOPIC THIN FILMS

by

Chuan Qin

Approved: _____
Edmund R. Nowak, Ph.D.
Chair of the Department of Physics and Astronomy

Approved: _____
George H. Watson, Ph.D.
Dean of the College of Arts and Sciences

Approved: _____
Ann L. Ardis, Ph.D.
Senior Vice Provost for Graduate and Professional Education

I certify that I have read this dissertation and that in my opinion it meets the academic and professional standard required by the University as a dissertation for the degree of Doctor of Philosophy.

Signed: _____

Yi Ji, Ph.D.
Professor in charge of dissertation

I certify that I have read this dissertation and that in my opinion it meets the academic and professional standard required by the University as a dissertation for the degree of Doctor of Philosophy.

Signed: _____

Karl M. Unruh, Ph.D.
Member of dissertation committee

I certify that I have read this dissertation and that in my opinion it meets the academic and professional standard required by the University as a dissertation for the degree of Doctor of Philosophy.

Signed: _____

Matthew DeCamp, Ph.D.
Member of dissertation committee

I certify that I have read this dissertation and that in my opinion it meets the academic and professional standard required by the University as a dissertation for the degree of Doctor of Philosophy.

Signed: _____

Juejun Hu, Ph.D.
Member of dissertation committee

ACKNOWLEDGMENTS

I would like to express my gratitude to all the wonderful people I have met during this unforgettable journey. Without their help, the completion of this dissertation would have been impossible.

First and foremost, I would like to thank my advisor: Professor Yi Ji. He is an excellent physicist and a great mentor. His wisdom, expert guidance and encouragement always inspire and motivate me throughout my Ph.D. study.

Also, I would like to thank all my committee members: Professor Karl Unruh and Professor Matthew DeCamp at UD Department of Physics and Astronomy, and Professor Juejun Hu at MIT Department of Materials Science and Engineering, for their guidance and support.

I would like to thank all group members Dr. Han Zou, Dr. Shuhan Chen, Yunjiao Cai, Fatih Kandaz and Xingyu Shen for their enlightening discussion and constant help. Thanks to all other colleagues and friends in the department, including Dr. Hao Zhu, Dr. Xin Fan, Dr. Xiaoming Kou, Dr. Qi Lu, Dr. Xing Chen, Dr. Chong Bi, Dr. Jun Wu, Dr. Yang Zhou, Dr. Yunpeng Chen, Dr. Yunsong Xie, Muhammad Asif Warsi, Tao Wang, Harsha Kannan, Rasoul Barri, Dr. Wanfeng Li, Dr. Alex Gabay, Dr. Yuan Gao, Dr. Zhiyuan Chen, Dr. Sui Luo, Siyu Luo, Dr. Ryan Stearrett, Dr. Brian Kelly, Kevin Haughey, Onur Tosun and Vimal Deepchand. I enjoyed working with them and they made the life in the basement more colorful.

I would like to thank all the faculty and staff members at Department of Physics and Astronomy for their friendly assistant over these years. Many thanks to

our lab manager Dr. John Shaw for his kind help with my graduate teaching assistant work, which is a wonderful experience in my life.

I would like to thank our collaborators at Fudan University in China. They are Dr. Yizheng Wu, Dr. Yongming Luo, Chao Zhou and Mengwen Jia.

I would like to give my special thanks to my husband, my parents and my parents-in-law for their love, support, understanding and encouragement. I am also grateful to my best friends Dr. Jing Qu and Yao Yao, for all the emotional support, camaraderie and caring they provided.

TABLE OF CONTENTS

Appendix

LIST OF TABLES

LIST OF FIGURES

ABSTRACT

Spin Hall effect (SHE) can convert longitude charge current (j_c) into a transverse spin current (j_s), owing to the strong spin-orbit coupling in heavy nonmagnetic metals, such as Pt. Its reciprocal process, inverse spin Hall effect (ISHE), converts spin current into charge current. The conversion rate between charge current and spin current is described by a spin Hall angle $\alpha_H = j_s/j_c$. Also, the spin diffusion length λ of the material is an important parameter to analyze the SHE. In a thin film that is thicker than λ, either a large α_H or a large λ can enhance the spin accumulation on the surface of the film, and contribute positively to a large spin Hall signal. Therefore, the product of α_H and λ can be used as figures of merit to quantify the efficiency of spin Hall process.

In this work, the SHE and ISHE of Pt films with mesoscopic dimensions are explored by using nonlocal spin injection/detection method at 10 K. We fabricate nonlocal SHE/ISHE structure, which consists of a Pt stripe, a ferromagnetic spin injector/detector bridged by a Cu channel. All relevant physical quantities are determined in-situ on the same substrate, and a quantitative approach is developed to characterize all processes effectively. Extensive measurements with various Pt thickness values reveal an upper limit for the Pt spin diffusion length: $\lambda_{pt} \leq 0.8$ nm. The average product of α_H and λ is substantial: $\alpha_H\lambda_{pt} = (0.142 \pm 0.040)$ nm for 4 nm thick Pt, though a gradual decrease is observed at larger Pt thickness. It's noteworthy that the resistivity of the Pt film is 150 – 300 μΩ•cm because of mesoscopic lateral confinement, and this value is substantially larger than that of an extended film. The

high resistivity (thereby low conductivity) enhances the energy efficiency of the spin Hall effects.

Anomalous Hall effect (AHE) in ferromagnets shares the same physics and mechanism of SHE. While SHE generates a pure spin current, AHE generates a transverse spin current as well as a charge current. Due to the ferromagnetic nature and the presence of charge current, it complicates the direct detection of the spin currents that accompanies AHE. By using nonlocal AHE/ISHE structures, we detect the spin accumulation generated by AHE in mesoscopic ferromagnetic $Ni_{81}Fe_{19}$ (permalloy or Py) films electrically. By exploring a series of devices with various Py thicknesses (4nm, 8nm, and 12nm), the Py spin diffusion length λ_{Py} is found to be much shorter than the film thicknesses. The product of α_H and λ_{Py} is determined to be independent of thickness and resistivity: $\alpha_H\lambda_{Py}$= (0.066 ± 0.009) nm at 5 K and (0.041 ± 0.010) nm at 295 K. These values are comparable to those obtained from mesoscopic Pt films. It makes Py an intriguing alternative to Pt, because of its lower cost and existing ferromagnetic properties.

Chapter 1

INTRODUCTION

Since the discovery of giant magnetoresistance (GMR) by A. Fert [1] and P. Grünberg [2] in 1988, spintronics is blossoming with promising potential in the information technology. Spintronics, which utilizes the electron spins to store information, offers the prospect of scalable, ultrafast and low-energy electronic devices. The most well-known application of spintronic devices is the use of GMR spin valve in the hard disk drive read head. In 1995, T. Miyazaki [3] and J. S. Moodera [4] observed a more significant effect – the tunneling magnetoresistance (TMR) in magnetic tunnel junctions (MTJs) at room temperature. Because TMR shows a higher magnetoresistance value and a negligible temperature dependence, MTJs has now replaced GMR spin valves in modern hard disk drives. Also, it's an essential component of the magneto-resistive random access memory (MRAM) [5], which is a non-volatile memory. Further efforts are made to achieve lower power consumption and better scalability for MRAM using MTJs, such as spin-transfer torque magnetic random access memory (STT-MRAM) [6], which is promising as the next generation of memory technology.

A spin current is a flow of angular momenta, which is essential to various spintronic functionalities. In contrast to a spin-polarized charge current, a pure spin current is generated in the situation where electrons with opposite spins move in opposite directions. Therefore, a pure spin current only carries the spin angular momentum flow without any charge current. Utilization of pure spin currents in

nanoscale electronic devices can greatly reduce energy dissipation and electro-migration. Therefore, generation, manipulation, and transport of pure spin current have been actively pursued in spintronics. We can produce a pure spin current in the following ways: spin pumping with microwave [7-10], spin Seebeck effect under the influence of a temperature gradient [11-13] or an electrical injection in nonlocal spin valves [14-18]. These methods generate pure spin currents from ferromagnetic materials. Recently, spin Hall effect (SHE) has drawn tremendous attention, since a pure spin current can be generated without magnetic materials. Due to the strong spin-orbit coupling in heavy non-magnetic metals (such as Pt), a charge current can induce a transverse pure spin current. The conversion rate is described by a spin Hall angle α_H. Several different experimental techniques [19-22] have been explored in order to measure the spin Hall angle in Pt, however reported results vary by more than a factor of 20 [23]. The accurate determination of spin Hall angle is important to characterize the efficiency of spin Hall effect.

The first research focus of this thesis is the study of SHE in Pt thin film using mesoscopic lateral structure with oxide barrier. Fig. 1.1 illustrates a lateral SHE structure: a Pt stripe and a ferromagnetic electrode (e.g. $Ni_{81}Fe_{19}$, Permalloy, or Py) are connected with a nonmagnetic channel (such as Cu). The Pt stripe is where SHE occurs and the Py electrode works as a spin injector/detector to probe the spin signal. Low-resistance AlO_x layers are placed at all interfaces. This unique lateral heterostructure has several advantages: it avoids the direct contact between Pt layer and ferromagnetic injector/detector, therefore there are no other phenomena such as proximity effect [24] or Rashba effect at the interface; in addition, the mesoscopic dimension of the lateral structure gives possibility of probing SHE over a small area.

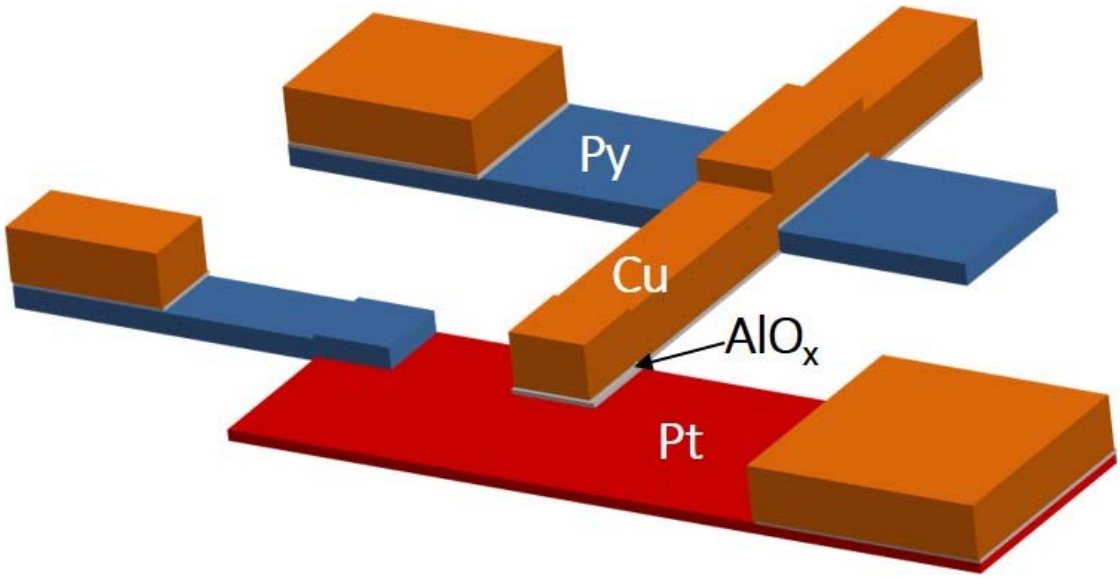

Figure 1.1: Three-dimensional view of nanoscale lateral SHE structure.

Also, anomalous Hall effect (AHE) in ferromagnetic materials (such as Py) shares the same physics and mechanism of SHE. The spin-orbit coupling generates an asymmetric deflection of the electrons depending on their spin orientations. Fig. 1.2 shows the family of spin-dependent Hall effects. In SHE as illustrated in Fig. 1.2 (a), equal numbers of electrons with opposite spins are deflected to opposite directions. The AHE is different from SHE, in that unequal numbers of electrons with opposite spins move to opposite directions because of the ferromagnetic nature of the metal. As a result, both spin current and charge current are generated as shown in Fig. 1.2 (b). It's interesting to see that their reciprocal processes – inverse spin Hall effect (ISHE) has similar scenario as shown in Fig. 1.2 (c) and (d). When a pure spin current is injected into a non-magnetic or ferromagnetic material, a transverse charge current is generated. Previous works to demonstrate the ISHE of Py have been carried out in the bilayer system of Py and ferromagnetic insulator yttrium iron garnet (YIG) [25-27].

However, because the spin accumulation owing to AHE is accompanied by a charge current and some other ferromagnetic effects coexist in Py, the direct detection of spin accumulation by AHE in ferromagnet is still lacking.

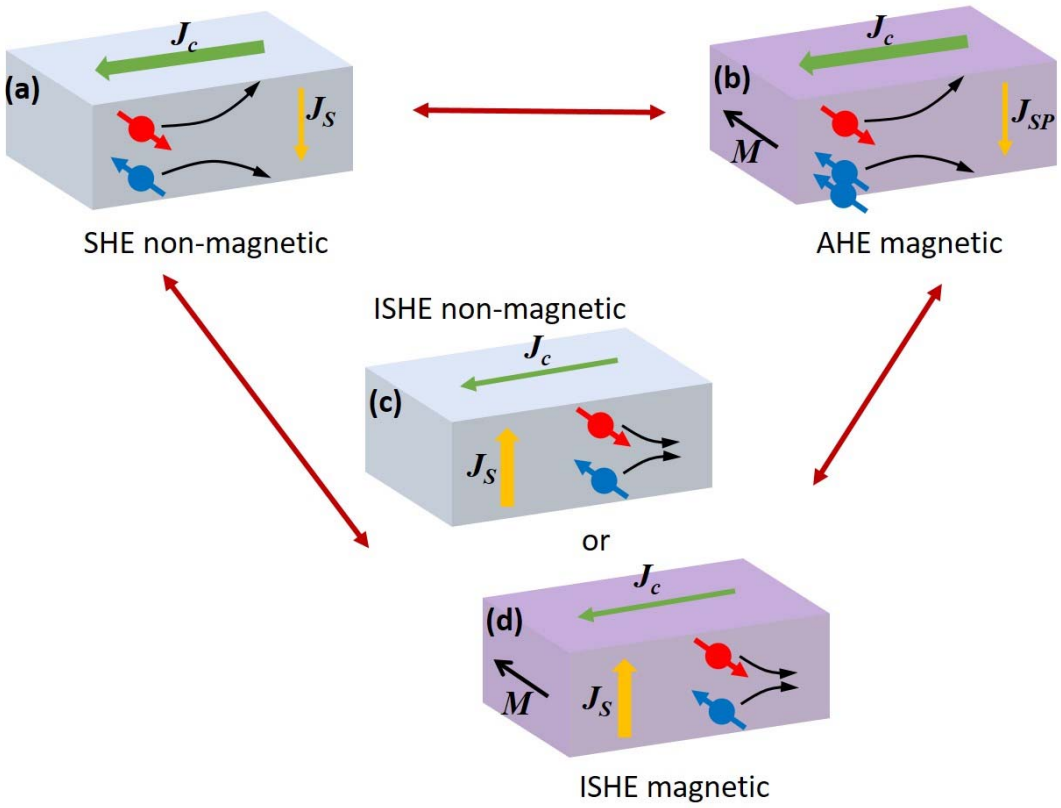

Figure 1.2: Illustrations of spin-dependent Hall effects family: (a) SHE and (c) ISHE in heavy non-magnetic metal, as well as (b) AHE and (d) ISHE in ferromagnetic metal. Parameters $\boldsymbol{J_C}$, $\boldsymbol{J_S}$ and $\boldsymbol{J_{SP}}$ denote charge current, spin current, and spin current accompanied by charge current, respectively. Parameter $\boldsymbol{M}$ represents the magnetization direction in ferromagnetic metal. Adapted from Ref. [25].

The second research focus of this thesis is the direct electrical detection of spin accumulation by AHE in Py. Similar mesoscopic lateral structure as those lateral SHE

structure in Fig. 1.1 is used by simply replacing the Pt stripe with Py, where the AHE is detected. With the alternating current (AC) modulation detection method, the AHE signals are extracted from the linear response of the nonlocal voltage difference between two polarities of large magnetic fields. Therefore, the signals are well separated from anomalous Nernst effects, anisotropic magnetoresistance, or regular nonlocal spin signals.

The thesis is organized in the following way. **Chapter 2** reviews the basic background of spintronics. Also, the fundamental theories and experiments of lateral spin valves, spin Hall effects and anomalous Hall effects will be discussed. **Chapter 3** covers the fabrication techniques involved in this dissertation including photolithography, electron beam lithography and electron beam evaporation. The measurement systems: the pulse tube variable temperature cryostat and electronic measurement setup, are presented as well. **Chapter 4** focuses on the observation of large SHE/ISHE signals in mesoscopic Pt thin films with lateral structure. A proper modeling and a quantitative approach are developed to characterize the SHE in Pt. At the same time, the thickness dependence of SHE for various Pt thin films is systematically studied. **Chapter 5** devotes to nonlocal electrical detection of spin accumulation generated by AHE in mesoscopic Py films. The efficiency of AHE in Py is also carefully quantified in this chapter.

REFERENCES

[1] M. N. Baibich, J. M. Broto, A. Fert, F. N. Vandau, F. Petroff, P. Eitenne, G. Creuzet, A. Friederich and J. Chazelas, Physical Review Letters **61** (21), 2472 (1988).

[2] G. Binasch, P. Grunberg, F. Saurenbach and W. Zinn, Physical Review B **39** (7), 4828 (1989).

[3] T. Miyazaki and N. Tezuka, Journal of Magnetism and Magnetic Materials **139** (3), L231 (1995).

[4] J. S. Moodera, L. R. Kinder, T. M. Wong and R. Meservey, Physical Review Letters **74** (16), 3273 (1995).

[5] B. N. Engel, J. Akerman, B. Butcher, R. W. Dave, M. DeHerrera, M. Durlam, G. Grynkewich, J. Janesky, S. V. Pietambaram, N. D. Rizzo, J. M. Slaughter, K. Smith, J. J. Sun and S. Tehrani, IEEE Transactions on Magnetics **41** (1), 132 (2005).

[6] M. Hosomi, H. Yamagishi, T. Yamamoto, K. Bessho, Y. Higo, K. Yamane, H. Yamada, M. Shoji, H. Hachino, C. Fukumoto, H. Nagao and H. Kano, IEEE International Electron Devices Meeting 2005, Technical Digest, 473 (2005).

[7] Y. Tserkovnyak, A. Brataas and G. E. W. Bauer, Physical Review Letters **88** (11), 4 (2002).

[8] S. Mizukami, Y. Ando and T. Miyazaki, Physical Review B **66** (10), 9 (2002).

[9] E. Shikoh, K. Ando, K. Kubo, E. Saitoh, T. Shinjo and M. Shiraishi, Physical Review Letters **110** (12), 5 (2013).

[10] Y. Ando, K. Ichiba, S. Yamada, E. Shikoh, T. Shinjo, K. Hamaya and M. Shiraishi, Physical Review B **88** (14), 6 (2013).

[11] K. Uchida, S. Takahashi, K. Harii, J. Ieda, W. Koshibae, K. Ando, S. Maekawa and E. Saitoh, Nature **455** (7214), 778 (2008).

[12] S. Bosu, Y. Sakuraba, K. Uchida, K. Saito, T. Ota, E. Saitoh and K. Takanashi, Physical Review B **83** (22), 6 (2011).

[13] K. Uchida, T. Nonaka, T. Ota and E. Saitoh, Applied Physics Letters **97** (26), 3 (2010).

[14] F. J. Jedema, A. T. Filip and B. J. van Wees, Nature **410**, 345 (2001).

[15] F. J. Jedema, H. B. Heersche, A. T. Filip, J. J. A. Baselmans and B. J. van Wees, Nature **416**, 713 (2002).

[16] Y. Ji, A. Hoffmann, J. S. Jiang and S. D. Bader, Applied Physics Letters **85** (25), 6218 (2004).

[17] Y. Ji, A. Hoffmann, J. E. Pearson and S. D. Bader, Applied Physics Letters **88** (5), 052509 (2006).

[18] X. J. Wang, H. Zou, L. E. Ocola and Y. Ji, Applied Physics Letters **95** (2), 3 (2009).

[19] E. Saitoh, M. Ueda, H. Miyajima and G. Tatara, Applied Physics Letters **88** (18), 182509 (2006).

[20] K. Ando, S. Takahashi, K. Harii, K. Sasage, J. Ieda, S. Maekawa and E. Saitoh, Physical Review Letters **101** (3), 036601 (2008).

[21] L. Q. Liu, O. J. Lee, T. J. Gudmundsen, D. C. Ralph and R. A. Buhrman, Physical Review Letters **109** (9), 096602 (2012).

[22] T. Kimura, Y. Otani, T. Sato, S. Takahashi and S. Maekawa, Physical Review Letters **98** (15), 156601 (2007).

[23] L. Q. Liu, R. A. Buhrman and D. C. Ralph, arXiv:1111.3702 (2011).

[24] S. Y. Huang, X. Fan, D. Qu, Y. P. Chen, W. G. Wang, J. Wu, T. Y. Chen, J. Q. Xiao and C. L. Chien, Physical Review Letters **109** (10), 5 (2012).

[25] B. F. Miao, S. Y. Huang, D. Qu and C. L. Chien, Physical Review Letters **111** (6), 5 (2013).

[26] H. Wu, C. H. Wan, Z. H. Yuan, X. Zhang, J. Jiang, Q. T. Zhang, Z. C. Wen and X. F. Han, Physical Review B **92** (5), 6 (2015).

[27] H. L. Wang, C. H. Du, P. C. Hammel and F. Y. Yang, Applied Physics Letters **104** (20), 4 (2014).

Chapter 2

BACKGROUND OF NONLOCAL SPIN VALVE AND SPIN HALL EFFECT

2.1 Introduction to Spintronics

2.1.1 Spin and Spin Current

With the development of the technology, people have realized that electrons play an important role in numerous physical phenomena, such as magnetism, electricity, thermal conductivity, etc. Early in 1897, J. J. Thomson performed a series of experiments indicating that electrons are unique charged particles and he estimated the charge and the mass of an electron [1]. Later in 1924, in order to describe the subatomic system, Wolfgang Pauli first proposed the concept of spin as "two-valued quantum degree of freedom". One year later, George Uhlenbeck and Samuel Goudsmit at Leiden University published their results, which supported Pauli's idea and hypothesized spin as another property of the electron [2, 3]. Then in 1928, when Paul Dirac derived his relativistic quantum mechanics theory, he explained why the electrons have peculiar spin angular momenta different from the orbital angular momenta [4]. His elegant equation pointed out that each electron spin has two quantum states $m_s\hbar$ in any direction, where $m_s = \pm\frac{1}{2}$ for spin-up (↑) or spin-down (↓) states and $\hbar$ as the reduced Plank constant. With the efforts of those physicists, people realized that for an electron, it not only has the mass m_e and charge $-e$, but also has spin m_s as its intrinsic property.

For a very long time, only the charge degree of freedom of an electron has been utilized in the conventional electronic devices by controlling the transport of electrons with an external electric field. In 1980s, the observation of spin-polarized electron injection from a ferromagnetic metal into a normal metal by Johnson and Silsbee (1985) [5] and the discovery of giant magnetoresistance (GMR) by A. Fert [6] and P. Grünberg [7] independently (1988) brought us into the era of spintronics. Spintronics, or spin electronics, is the study of how to exploit the spin properties instead of or in addition to the charge degree of freedom in solid state physics. Proper utilization of spin-dependent electron transport phenomena provides the possibility to produce spintronic devices with new functionalities, including non-volatility, faster data processing speed and lower energy consumption.

In order to better understand the spin-dependent electron transport, one can consider spin-up electrons and spin-down electrons flow through two channels [8, 9]. $I_{\uparrow}$ represents the current for spin-up channel and $I_{\downarrow}$ is the current for spin-down channel. A charge current is a net charge flow, defined as $I_C = I_{\uparrow} + I_{\downarrow}$. And the definition of a spin current is $I_S = I_{\uparrow} - I_{\downarrow}$, which refers to the flow of spin angular momentum. Figure 1.1 shows the differences between an unpolarized charge current, a spin-polarized current and a pure spin current. For an unpolarized charge current, same numbers of spin-up and spin down electrons flow in the same direction, and the flow of spin angular momentum cancels out. In a spin-polarized current, spin-up and spin-down electrons flow in one direction, but the number of up- and down-spins are not the same. If equal amount of spin-up and spin-down electrons flow in opposite directions as shown in the bottom panel of Fig. 2.1, we have a pure spin current with a spin angular momentum flow of $I_S = 2I_{\uparrow}$ and a zero charge flow ($I_C = 0$).

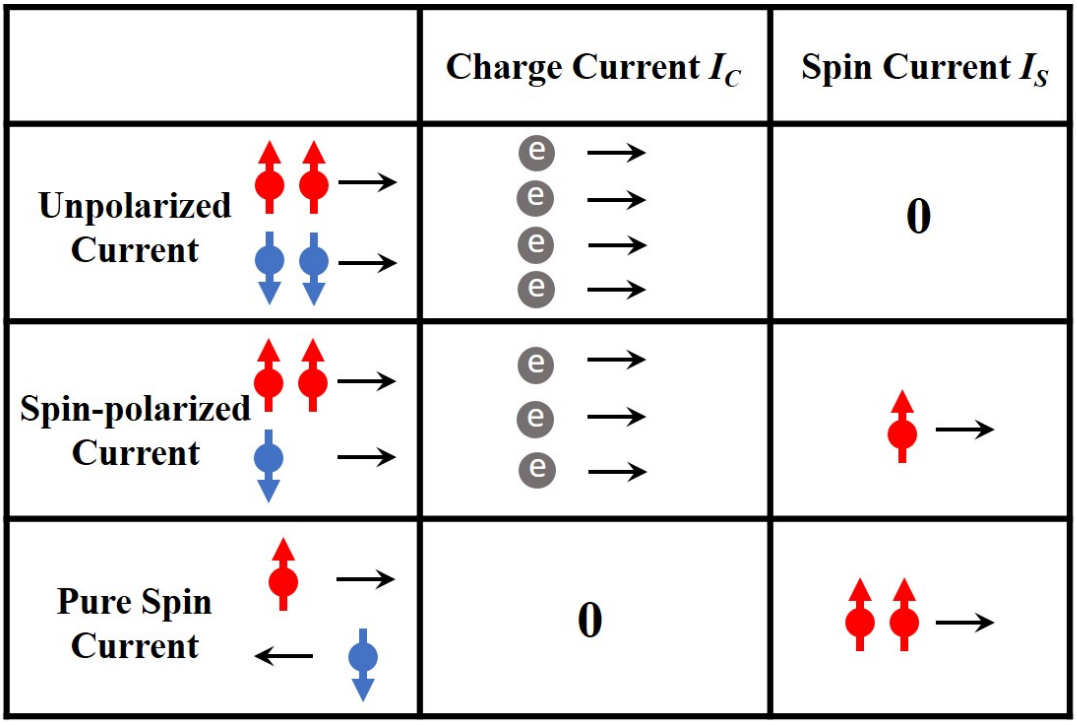

Figure 2.1: Table of the charge current and the spin current.

2.1.2 Electronic Band Structure of Metals and Spin Polarization

The spin-dependent transport in metals is closely related to the electronic band structures. For a normal metal, such as Cu, Al or Au, the d band is completely filled and Fermi energy lies in s or p band. The band structure can be described by Sommerfeld-Drude model [10]. As shown in Fig. 2.2 (a), the density of states (DOS) of spin-up and spin-down electrons are equal.

In a ferromagnetic metal, e.g., 3d transition metal (Fe, Ni or Co), the 3d band is not fully filled, hence it determines the magnetic property of the material. Due to the exchange interaction, the energy bands of spin-up and spin-down states split in the absence of an external magnetic field, causing an unequal occupancy of two spin

states as shown in Fig. 2.2 (b). According to the Heisenberg's model [10], the exchange interaction energy can be described as:

$$E_{ex} = -J_{ex}\, \boldsymbol{S_1} \cdot \boldsymbol{S_2} \tag{2.1}$$

where J_{ex} is Heisenberg's exchange integral, and $\boldsymbol{S_1}$, $\boldsymbol{S_2}$ are the electron spins. When $J_{ex} > 0$, parallel spins are favored to minimize E_{ex}, and lead to ferromagnetism.

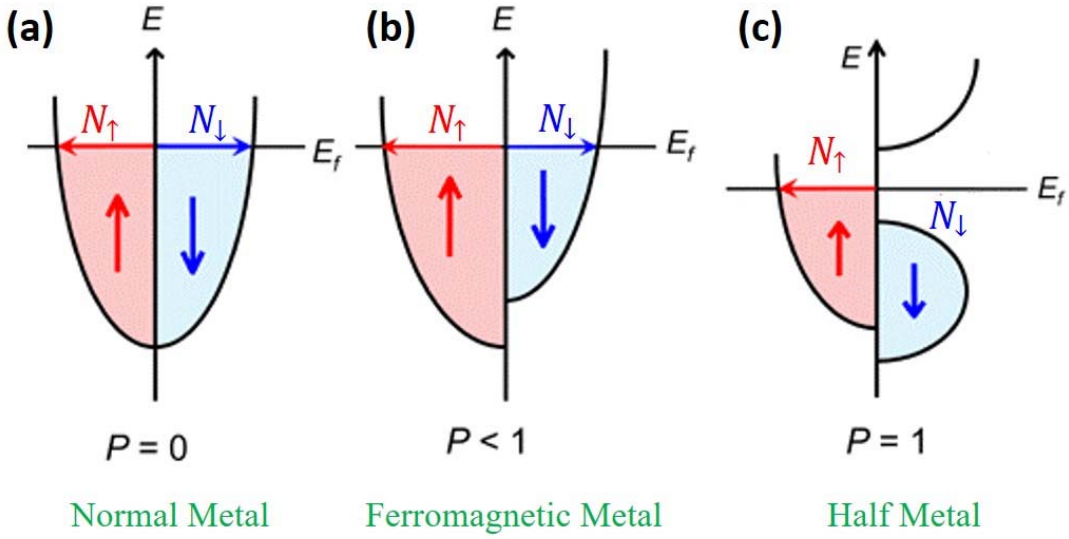

Figure 2.2: Density of states for spin-up and spin-down electrons in (a) normal metal; (b) ferromagnetic metal and (c) half metal.

For spin-dependent transport, the concept of electron spin polarization is essential. It's defined as:

$$P = \frac{N_\uparrow(E_F) - N_\downarrow(E_F)}{N_\uparrow(E_F) + N_\downarrow(E_F)} \tag{2.2}$$

where $N_\uparrow(E_F)$ and $N_\downarrow(E_F)$ are the density of states (DOS) at Fermi energy level for spin-up and spin-down electrons, respectively. From Fig. 2.2 (a), it's obvious that $P =$

0 for normal metals because of the equal occupancy of two spin states. On the other hand, in Fig. 2.2 (b), the band split results in $0 < P < 1$ in ferromagnetic materials. A special case shows in Fig. 2.2 (c): some materials have a band gap as a typical semiconductor for one of the spin states (the contribution of $N_{\downarrow}(E_F)$ is zero), which results in $P = 1$. This type of material is named as "half-metal", since it exhibits metallic behaviors for one subband and semiconducting behaviors for the other subband.

2.1.3 Giant Magnetoresistance (GMR)

The rapid development of thin film deposition techniques in 20th century, including magnetron sputtering, thermal evaporation and molecular beam epitaxy, provides the technical capabilities for precise control of thin film thickness in nanoscale. This leads to the discovery of new physics phenomena. One of the most significant milestones is the giant magnetoresistance (GMR) [6, 7]. In 1986, Grünberg *et al.* [11] firstly observed the antiferromagnetic exchange coupling of two Fe layers across the Cr interlayers in Fe/Cr/Fe trilayer structure. Then, Grünberg further found the magnetoresistance (MR) is up to 1.5% at room temperature, which is substantially higher than the anisotropic magnetoresistance (AMR) in a single Fe thin film. At the same time, Fert group discovered independently that the Fe/Cr multilayer magnetic superlattices had a large MR as much as 50% at 4.2 K. And the room temperature value of 17% was still significant. This large magnetoresistance phenomenon was named as giant magnetoresistance (GMR). The discovery of GMR not only contributes significantly to the modern information storage technology such as the hard disk drive, but also marks the inception of spintronics. The 2007 Nobel Prize in

Physics was awarded to Grünberg and Fert for their great contributions in the discovery of GMR.

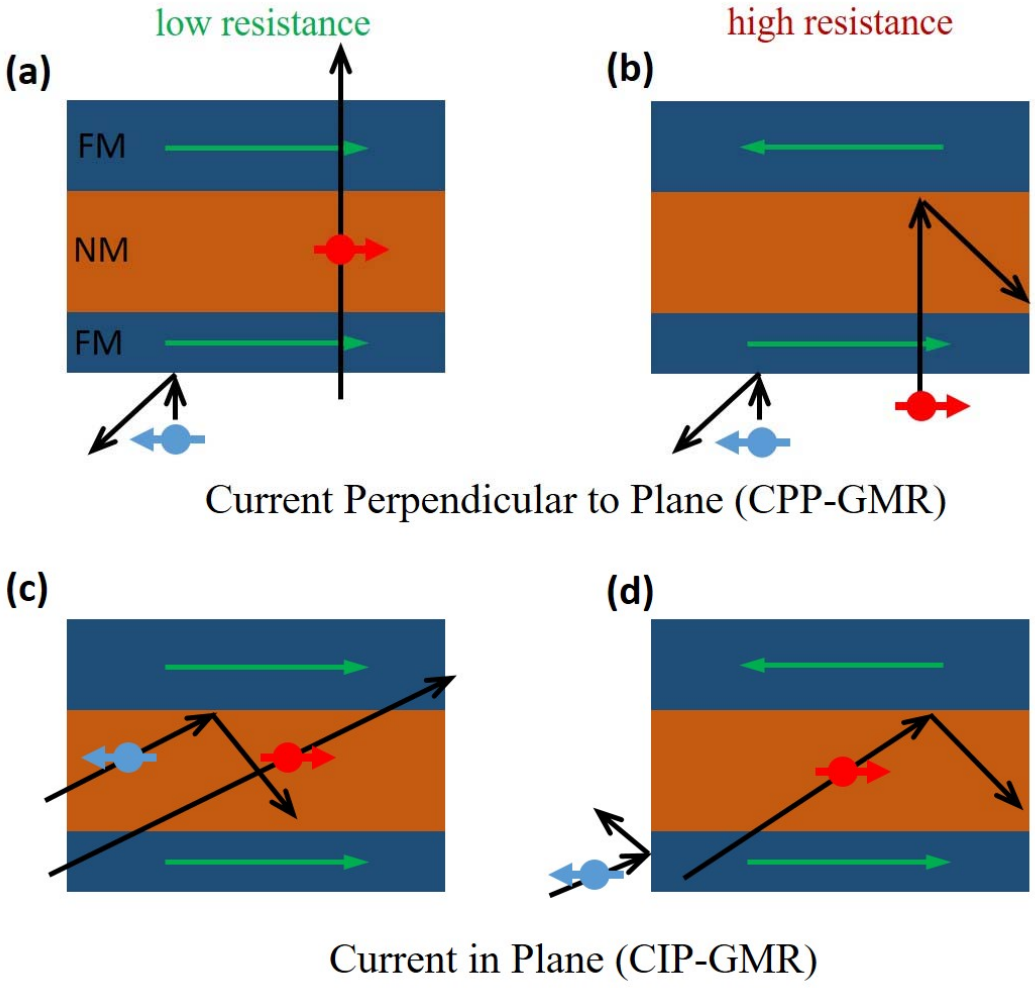

Figure 2.3: GMR in CPP geometry with (a) parallel and (b) antiparallel FM layers; GMR in CIP geometry with (c) parallel and (d) antiparallel FM layers.

A typical GMR structure consists of two ferromagnetic (FM) layers sandwiching by a nonmagnetic (NM) layer as shown in Fig. 2.3. The magnetization of

the FM layer can be controlled by an external magnetic field. There are two geometries of GMR structure: if the charge current flows perpendicular to the interface shown in Fig. 2.3 (a) or (b), the geometry is called the current-perpendicular-to-plane (CPP) structure; if the current is parallel to the interface illustrated as Fig. 2.3 (c) or (d), it's named as the current-in-plane (CIP) structure. The electrical resistance in both geometries depends on the magnetization orientations of two FM layers. When the magnetizations of two FM layers are aligned parallel, it exhibits a high resistance value; when they are antiparallel, a low resistance is observed.

The principle of GMR can be understood by using two current model proposed by Mott [12, 13] in 1936. There are two major points assumed in Mott's model: (1) one can consider the spin-up and spin-down electrons as two independent electrical conducting channels in metals, and these two spin channels are treated in parallel configuration; (2) for the ferromagnetic metals, the scattering probabilities of spin-up and spin-down electrons are different. In other words, the scattering rate is spin-dependent. Spins antiparallel to the magnetization orientation of the FM layer has a higher scattering rate, and therefore that spin channel has a high resistance state $R_{\uparrow\downarrow}$. The scattering is weak if spins are parallel to the magnetization of FM and the spin channel shows a low resistance state $R_{\uparrow\uparrow}$. Fig. 2.4 illustrates the Mott model in GMR structure. When the magnetizations of two FM layers are parallel with each other, spin-up electron channel passes through both FM layers without strong scattering. On the contrary, the spin-down electron is antiparallel to the magnetization of both FM layers, therefore experiencing strong scattering. Since spin-up and spin-down channels are considered as parallel resistor model, the total resistance is mainly determined by the spin-up channel with low scattering rate, and therefore the resistance is low. The

total resistance in this case can be written as $R_P = \frac{2R_{\uparrow\uparrow}R_{\uparrow\downarrow}}{R_{\uparrow\uparrow}+R_{\uparrow\downarrow}}$. On the other hand, for the two antiparallel FM layers, both spin-up and -down channels encounter strong scattering by one of the FM layers leading to a high total resistance, which is $R_{AP} = \frac{R_{\uparrow\uparrow}+R_{\uparrow\downarrow}}{2}$. The giant magnetoresistance in this trilayer structure can be expressed using Eq. 2.3:

$$GMR = \frac{\Delta R}{R_P} = \frac{R_P - R_{AP}}{R_P} = -\frac{(R_{\uparrow\uparrow}-R_{\uparrow\downarrow})^2}{4R_{\uparrow\uparrow}R_{\uparrow\downarrow}} \tag{2.3}$$

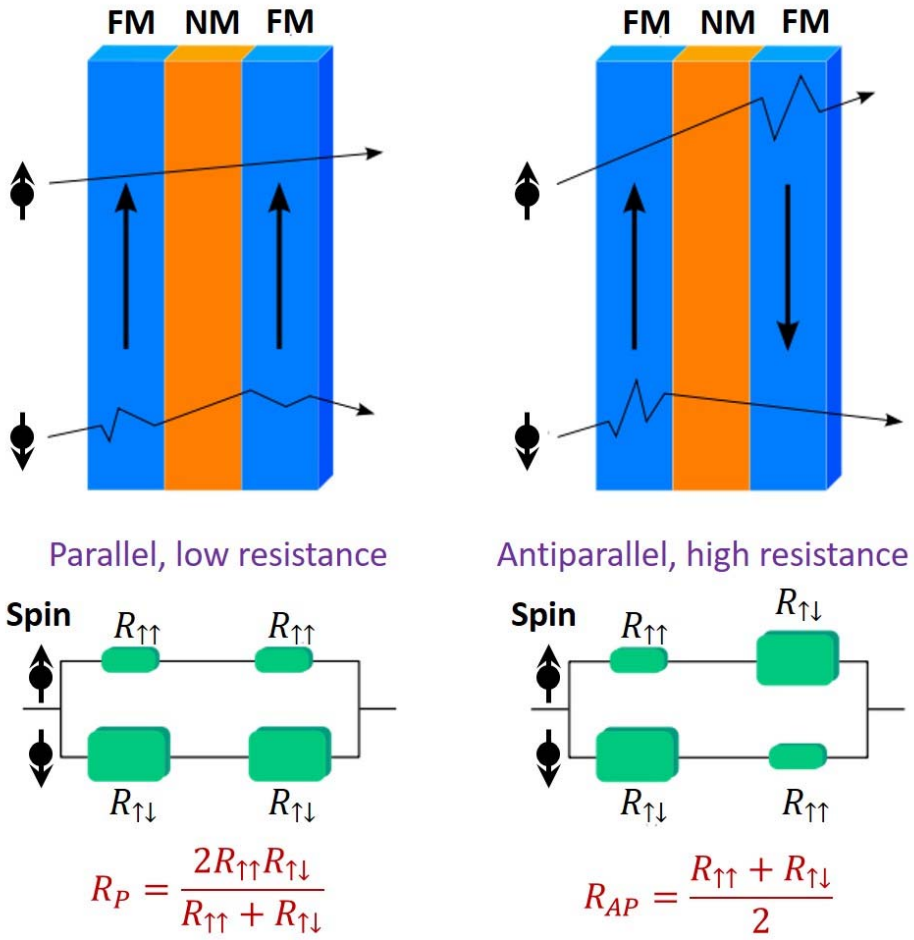

Figure 2.4: Two current model by Mott in GMR. Adapted from Wikipedia.

2.1.4 Magnetic Tunneling Junction (MTJ) and Tunneling Magnetoresistance (TMR)

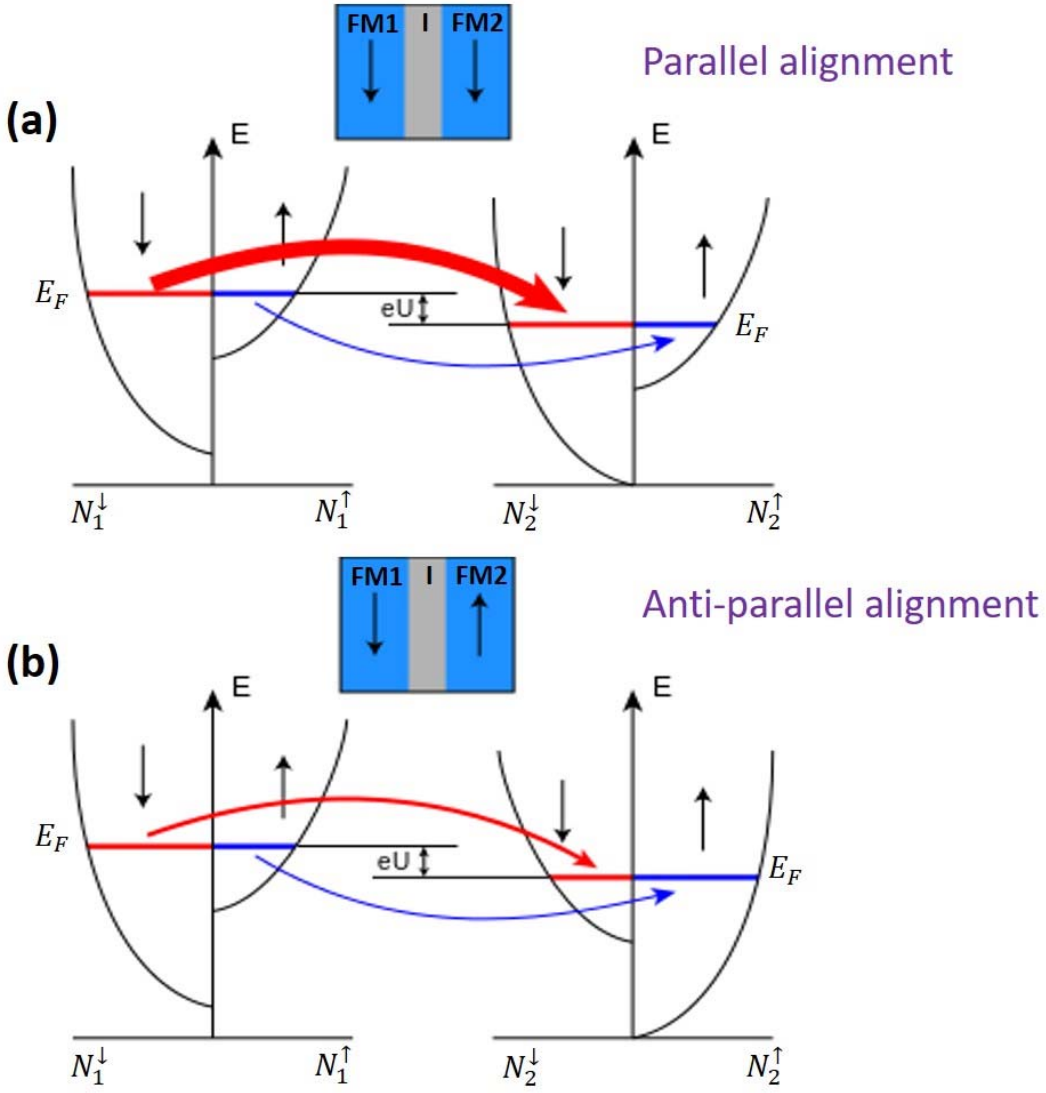

Figure 2.5: A schematic drawing of spin-dependent tunneling in MTJs: (a) parallel and (b) anti-parallel alignment of the magnetizations. $N_1^{\uparrow}$, $N_1^{\downarrow}$, $N_2^{\uparrow}$ and $N_2^{\downarrow}$ represent DOS for spin-up and spin-down electrons in FM1 and FM2 layers. Adopted from Wikipedia.

Another breakthrough in the history of spintronics is the magnetic tunneling junction (MTJ) structure. A MTJ has two ferromagnetic layers (FM) separated by a thin insulating layer (I) to form a FM/I/FM trilayer structure. The insulator is thin enough that electrons can tunnel through the insulating barrier between the two metallic electrodes. As shown in Fig. 2.5, an external magnetic field can alter the magnetization directions of two ferromagnetic layers (FM1 and FM2), and orientate them in parallel or anti-parallel alignments. In Fig. 2.5 (a), if FM1 and FM2 are parallel, the majority electrons in FM1 tunnel through the barrier into majority band of FM2; the minority electrons in FM1 tunnel into the minority band of FM1. As a result, the probability of electrons tunneling through the insulator between two ferromagnetic layers is large, and we have a low resistance state R_P. If FM1 and FM2 are anti-parallel as shown in Fig. 2.5 (b), majority electrons in FM1 tunnel into FM2 minority band and FM1 minority electrons tunnel into the majority band of FM2. Therefore, low possibility of electron tunneling is expected, leading to a high resistance state R_{AP}. The resistance change between parallel and antiparallel configurations in MTJs is defined as tunneling magnetoresistance (TMR) effect, which is expressed as:

$$TMR = \frac{R_{AP}-R_P}{R_P} \times 100\% = \frac{\sigma_P-\sigma_{AP}}{\sigma_{AP}} \times 100\% \tag{2.4}$$

where, σ_P and σ_{AP} are the tunneling conductivity for parallel and anti-parallel states.

In 1975, M. Jullière first observed a 14% TMR ratio in Fe/Ge/Co MTJs at low temperature and he proposed a simple Jullière model to describe TMR [14]. In Jullière's two spin channel model, he neglects the spin-flip in the tunneling process and assumes that the tunneling conductivity (σ) for each spin channel is proportional to the density of state (DOS) at Fermi energy level of two ferromagnetic layers.

$$\sigma_{\alpha,\beta} \propto N_1^{\alpha}(E_F) N_2^{\beta}(E_F) \tag{2.5}$$

in Eq. 2.5, $\alpha, \beta = \uparrow$ or $\downarrow$ represents direction of electron spins; $N_1(E_F)$ and $N_2(E_F)$ are the DOS at Fermi energy level in FM1 and FM2 electrodes. Then, the total tunneling conductivity in parallel state and anti-parallel state can be described as:

$$\sigma_P = \sigma_{\uparrow,\uparrow} + \sigma_{\downarrow,\downarrow} \propto N_1^{\uparrow}(E_F)N_2^{\uparrow}(E_F) + N_1^{\downarrow}(E_F)N_2^{\downarrow}(E_F), \tag{2.6.1}$$

$$\sigma_{AP} = \sigma_{\uparrow,\downarrow} + \sigma_{\downarrow,\uparrow} \propto N_1^{\uparrow}(E_F)N_2^{\downarrow}(E_F) + N_1^{\downarrow}(E_F)N_2^{\uparrow}(E_F). \tag{2.6.2}$$

According Eq. 2.4, TMR ratio is

$$TMR = \frac{\sigma_P - \sigma_{AP}}{\sigma_{AP}} = \frac{(N_1^{\uparrow}(E_F)N_2^{\uparrow}(E_F) + N_1^{\downarrow}(E_F)N_2^{\downarrow}(E_F)) - (N_1^{\uparrow}(E_F)N_2^{\downarrow}(E_F) + N_1^{\downarrow}(E_F)N_2^{\uparrow}(E_F))}{N_1^{\uparrow}(E_F)N_2^{\downarrow}(E_F) + N_1^{\downarrow}(E_F)N_2^{\uparrow}(E_F)} \tag{2.7}$$

Based on the definition of spin polarization for ferromagnetic material in Eq. 2.2, we can rewrite Eq. 2.7 and get the TMR in Jullière's model as:

$$TMR = \frac{2P_1P_2}{1 - P_1P_2} \tag{2.8}$$

where P_1(or P_2) is the spin polarization for FM1 (or FM2) layer. Later in 1989, a more complete theory of TMR effect is described by Slonczewski, where he discussed the effects of barrier height and barrier thickness on the tunneling conductance [15].

In 1995, two research groups observed relatively large TMR effect in MTJs with amorphous Al_2O_3 barrier. Miyazaki *et al.* [16] reported 18% TMR ratio at room temperature and 30% at 4.2 K with Fe/ Al_2O_3/Fe junction. At the same time, Moodera group [17] discovered 11.8%, 20% and 24% TMR ratios at 295 K, 77K and 4.2 K, respectively. These discoveries inspired the experimental and theoretical physicists to further explore the spin-dependent tunneling property in MTJ structures [18-20]. In MTJs with AlO_x barrier, a TMR ratio as high as 80% at room temperature has been reported experimentally [20]. However, this value is still not large enough to be used in spintronic devices. For example, in the high-density magnetoresistive random-access memory (MRAM), it requires each MTJ unit cell to have 150% or higher TMR

ratio at room temperature; also, the read head of a modern hard disk drive needs high TMR value. At this point, the AlO_x based MTJs limits the feasibility of spintronic memory devices.

Efforts are made by researchers in the past decades trying to optimize MTJs with higher TMR ratios. These efforts include using ferromagnetic materials with higher spin polarization and improving the quality of insulating barrier. Since 2000, crystalline magnesium oxide (MgO) tunnel barrier in MTJs has been explored for the enhancement of TMR values in those structures. In 2001, Butler *et al.* [21] and Mathon *et al.* [22] independently made the theoretical prediction that with MgO barrier, the TMR can reach several thousand percent. Then in 2004, S. Parkin's group in IBM lab obtained a giant TMR value in single-crystalline Fe/MgO/Fe MTJs with 220% at room temperature and 300% at low temperature. These MTJs are sputter-deposited [23]. The same year, Yuasa group in AIST reported that the MgO based MTJs fabricated with molecular beam epitaxy (MBE) exhibited a 180% TMR ratio at room temperature [24]. The largest TMR effect so far has been experimentally observed in 2008, Ikeda *et al.* [25] reported a TMR ratio of 604% at room temperature and 1144% at 5 K in CoFeB/MgO/CoFeB MTJs.

2.2 Nonlocal Spin Valve (NLSV)

The GMR spin valve or the MTJ discussed in the last section, is a vertical heterostructure with two terminals. It generates a spin-polarized charge current where the spin current is accompanied by the charge current. A non-local spin valve (NLSV) is different that it is a lateral heterostructure. Two ferromagnetic electrodes (F1 and F2) are separated and connected with a nonmagnetic channel (N). In the NLSV, a pure

spin current could be separated from the charge current in the nonmagnetic channel. The detailed principle of the NLSV will be discussed in the following paragraphs.

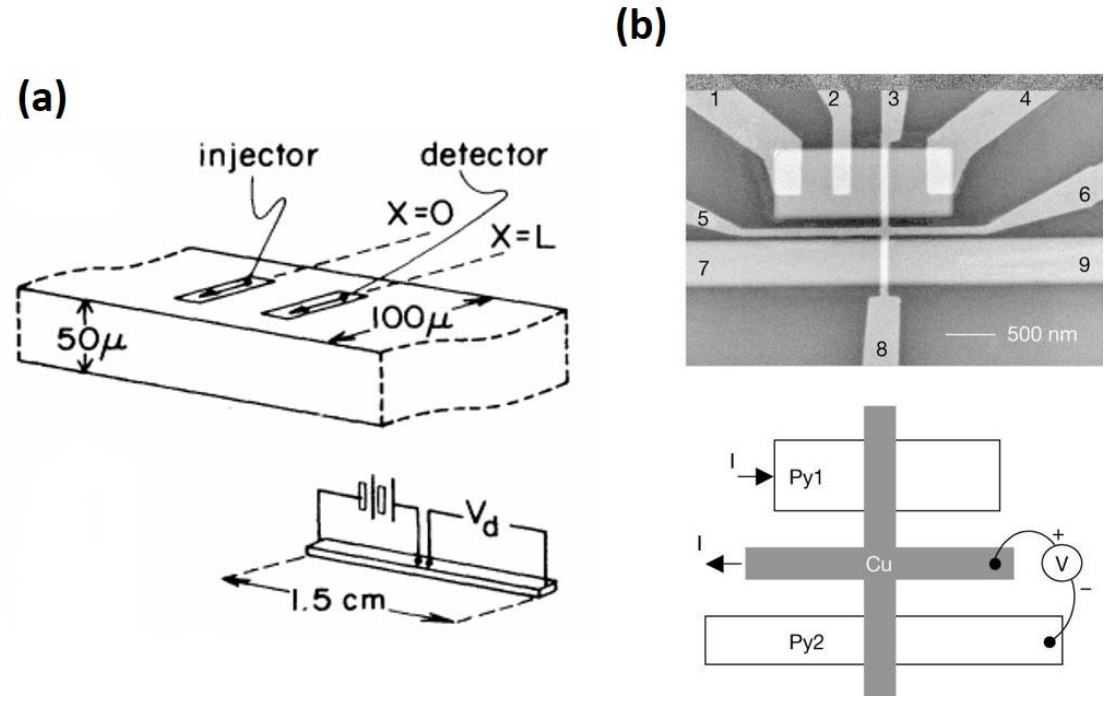

Figure 2.6: (a) Geometry of nonlocal spin injection and detection in bulk Al film; (b) mesoscopic Py/Cu/Py lateral spin valve. Reprinted with permission from Ref. [5] and Ref. [27].

In 1985, Johnson and Silsbee first demonstrated the nonlocal spin injection and detection in a bulk paramagnetic Al wire with two $Ni_{81}Fe_{19}$ (Permalloy or Py) leads patterned on the top, and the measurement geometry is shown in Fig. 2.6 (a). An electric current is passed from the Py injector to one end of Al, then the induced voltage (~ a few pV) between detector and the other end of Al wire is measured at low temperature. In this measurement configuration, there is no net charge current in the

region between two Py leads [5, 26]. With the development of nanofabrication techniques, Jedema *et al.* performed same idea in a mesoscopic Py/Cu/Py lateral spin valve (Fig. 2.6 (b)) at room temperature and obtained much larger signals [27]. One year later, they reported the enhancement of spin injection by inserting an oxide barrier between the ferromagnetic electrode and the nonmagnetic channel [28]. These pioneering works stimulates further research on the spin transport in nanoscale lateral devices.

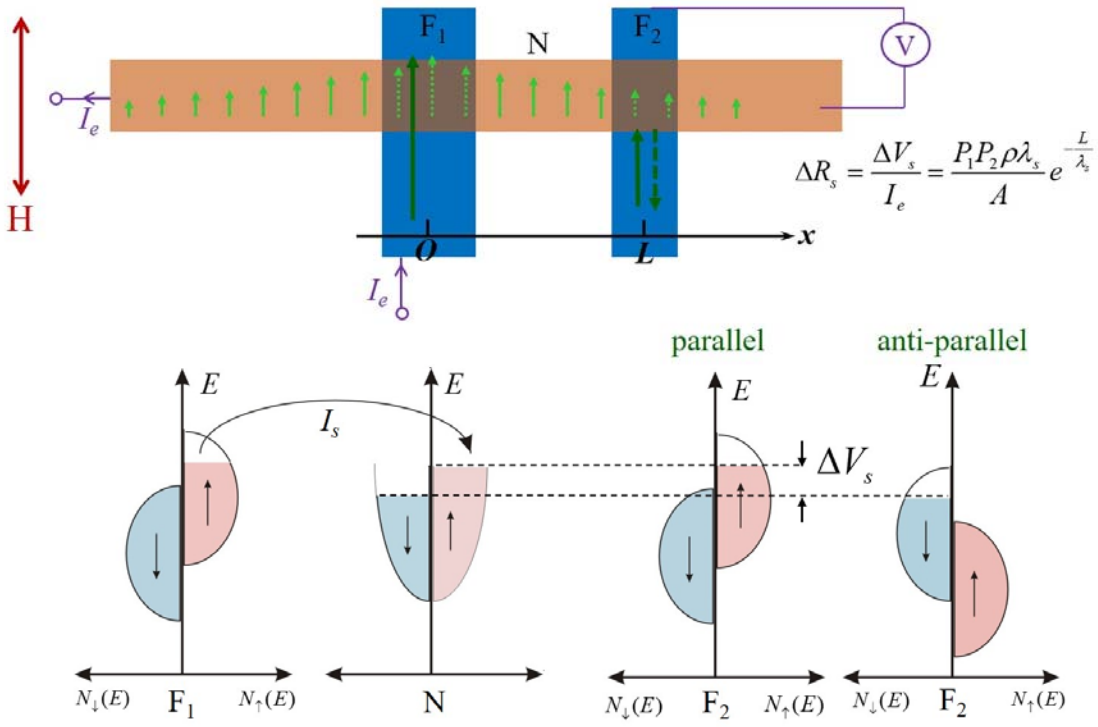

Figure 2.7: Measurement geometry of a NLSV. Dark green arrows in F1 and F2 electrodes indicate the magnetization direction. Light green arrows are the spin accumulation in N channel. Density of states for spin-up and spin-down electrons in F1, N and F2 (parallel or anti-parallel configuration) are shown in lower portion of the picture. Adapted from Ref. [29].

Fig 2.7 illustrates the measurement configuration of a NLSV with F1 and F2 separated by a length L along x direction. When a charge current I_e flows through F1 injector toward the left end of N channel, spin-polarized electrons are injected from F1 to N across the interface, causing an energy splitting of the Fermi levels between spin-up and spin-down electrons in N. Therefore, a spin accumulation is induced in N channel. The spin accumulation diffuses away from the injection point ($x = 0$), which drives a pure spin current. Though the charge current only flows in one direction from F1 to left end of N, but the spin accumulation diffuses in both directions in N channel. Thus, only a pure spin current flows in the portion of N channel that is to the right side of F1. In this process, the spin-dependent current density in F1 and N is given by

$$j_{\uparrow,\downarrow} = -(\frac{\sigma_{\uparrow,\downarrow}}{e})\nabla\mu_{\uparrow,\downarrow} \tag{2.9}$$

In this expression, $\sigma_{\uparrow,\downarrow}$ is the conductivity for spin-up and -down channel. The electrochemical potential $\mu_{\uparrow,\downarrow} = \mu_{ch\,\uparrow,\downarrow} + eV$, where $\mu_{ch\,\uparrow,\downarrow}$ is the chemical potential and V is the electrical voltage. The charge current density is described as $j_c = j_\uparrow + j_\downarrow = -(\nabla\sigma_\uparrow\mu_\uparrow + \nabla\sigma_\downarrow\mu_\downarrow)/e$, and the spin current density $j_s = j_\uparrow - j_\downarrow = -(\nabla\sigma_\uparrow\mu_\uparrow - \nabla\sigma_\downarrow\mu_\downarrow)/e$. The spin polarization P is defined as $P = j_s/j_c = (j_\uparrow - j_\downarrow)/(j_\uparrow + j_\downarrow)$, which describes the spin injection efficiency of the current across F/N interface. The pure spin current flow in the $x > 0$ region of N is well described using the diffusion equation of spin accumulation:

$$\nabla^2(\mu_\uparrow - \mu_\downarrow) = \frac{\mu_\uparrow - \mu_\downarrow}{\lambda_s^2} \tag{2.10}$$

which is characterized by the spin diffusion length λ_s in N.

The F2 electrode is used as a detector to measure the spin accumulation and the principle is shown in Fig 2.7. The spin orientation of F2 can be controlled by an external magnetic field H. When the spins in F2 is aligned parallel to the spin

accumulation (P state), its Fermi level is aligned with the upper Fermi energy level in N, and therefore exhibits a high voltage. If the spins in F2 is anti-parallel to the spin accumulation (AP state), a low voltage is measured. A voltage difference (ΔV_S) is obtained between P and AP states. The nonlocal spin signal is then defined as the voltage difference normalized by the injection current:

$$\Delta R_S = \frac{\Delta V_S}{I_e} = \frac{P_1 P_2 \rho \lambda_S}{A} e^{-\frac{L}{\lambda_S}} \tag{2.11}$$

where P_1 and P_2 are the spin polarization at F1/N and F2/N interface, ρ is the resistivity of N channel and A is the cross-sectional area of N [29]. Fig. 2.8 shows a typical nonlocal spin signal at 4.5 K in a Py/Cu/Py NLSV with AlOx barrier. The external magnetic field is applied parallel to the ferro-electrodes, which alters the magnetization directions of F1 and F2. High R_S value indicates a P state while low R_S value refers to an AP configuration [30].

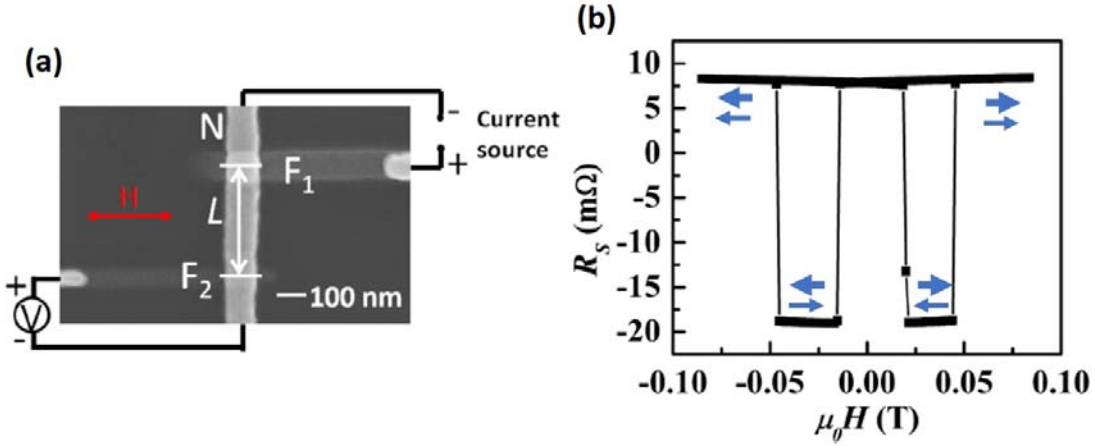

Figure 2.8: (a) A scanning electron microscope (SEM) picture of a Py/Cu/Py NLSV with AlO_x barrier; (b) nonlocal resistance R_S versus magnetic field $\mu_0 H$ measured at 4.5 K. Blue arrows indicate the magnetization directions of F1 and F2. Reprinted with permission from Ref. [30].

The planar geometry of the NLSV adds the degree of freedom in the lateral dimension, and allows the observation of other spin transport phenomena in NLSVs. Spin dynamics [28, 31, 32], spin transfer torque (STT) effects [33-35], spin Seebeck effects [36, 37], as well as spin Hall effects [38, 39] have been demonstrated in the lateral structure. In the next section, we will focus on the spin Hall effects and the related measurements using nonlocal spin valves.

2.3 Spin-dependent Hall Effects

2.3.1 Spin Hall Effect (SHE)

In Chapter 1, we have introduced the concept of SHE as shown in Fig. 1.2 (a). When a charge current is applied to the material, the spin-orbit interaction deflects equal number of spin-up and spin-down electrons to opposite boundaries, causing the spin accumulation on the edge in transverse direction. Therefore, a pure spin current that is perpendicular to the applied charge current is generated. Vice versa, its reciprocal process, which is known as inverse spin Hall effect (ISHE), is the phenomenon in which a pure spin current can generate a transvers charge current (Fig. 1.2 (c)). The idea of SHE was first predicted by Dyakonov and Perel in 1971 [40, 41]. In 1999, Hirsch revived the concept and named these phenomena as spin Hall effects [42]. The mechanisms of SHE can be classified into two categories: one is the intrinsic SHE, which is related to the band structure of the material [43]; the other is extrinsic SHE, which is based on the impurity scattering, i.e. skew scattering [44] and side jump [45].

Because SHE only generates the spin accumulation without any charge voltage, it makes the experimental detection more difficult compared to other spin-

dependent transport phenomena. Until 30 years after the first prediction, the direct observation of SHE was demonstrated experimentally by Y. Kato in semiconductors with the use of Kerr rotation microscopy [46]. Although the magneto-optic Kerr effect (MOKE) for the detection of SHE in semiconductors is well-established and useful, this method is not applicable to the metallic system. In 2006, Valenzuela and Tinkham reported the direct electrical detection of inverse spin Hall signal in Al strip with a lateral nonlocal structure [38]. It triggered intense research efforts on SHE with various heavy nonmagnetic metals, such as Pt, Pd and Ta, which exhibit large spin Hall signals due to their strong spin-orbit coupling. There are two major systems to quantify SHE/ISHE in metals. The most widely explored one is ferromagnet/heavy-metal bilayer structure and the other is mesoscopic nonlocal structure.

With $Ni_{81}Fe_{19}$/Pt bilayer structure, Saitoh *et al.* [47] observed ISHE in Pt thin film at room temperature induced by a pure spin current. A pure spin current is injected from $Ni_{81}Fe_{19}$ layer into Pt layer using spin pumping method, which is shown in Fig. 2.9 (a). Owing to ISHE in Pt, the pure spin current is converted into transverse charge current, which causes charge accumulation at the edges of Pt layer. As a result, an electric potential difference between the edges can be measured. In 2008, Ando *et al.* [48] reported direct spin Hall effect with the same bilayer structure as illustrated in Fig. 2.9 (b). When an electric charge current is applied through Pt, a pure spin current is generated and injected into adjacent $Ni_{81}Fe_{19}$ layer due to SHE. It exerts a spin torque to the ferromagnetic layer, causing the magnetization precession, which can be monitored by the ferromagnetic resonance (FMR) spectrum. The spin Hall angle of Pt layer at room temperature is also estimated to be ~ 0.08 by Ando *et al*.

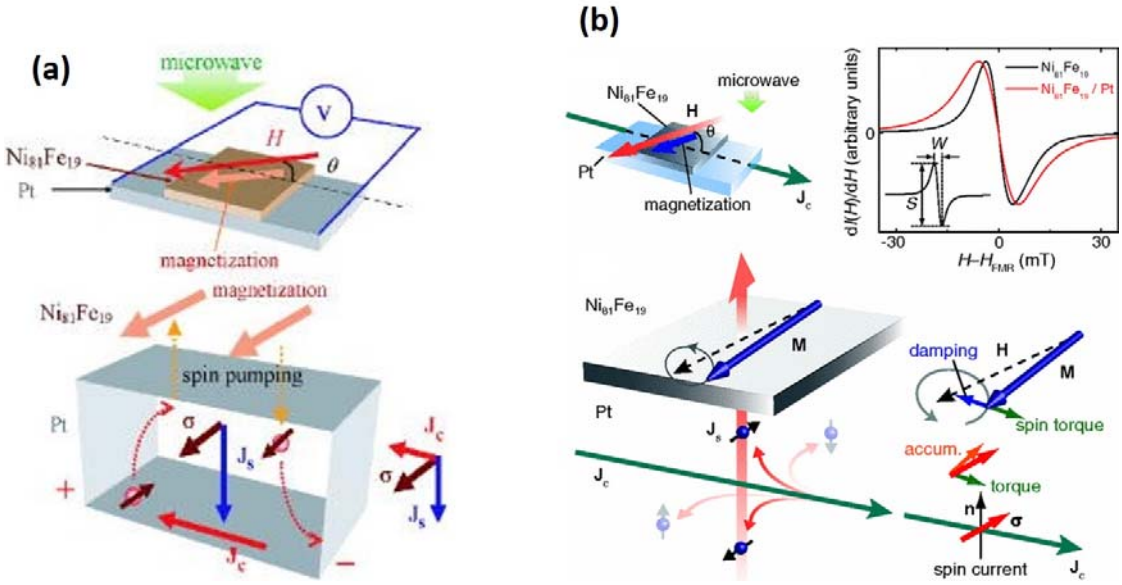

Figure 2.9: Schematic illustrations of (a) the spin pumping effect and the ISHE in Saitoh's bilayer structure; (b) the SHE and the spin-torque effect, as well as FMR signal in Ando's bilayer structure. Parameters $\boldsymbol{\sigma}$, $\boldsymbol{J_c}$ and $\boldsymbol{J_s}$ denote the spin-polarization vector of the spin current, the flow direction of charge current and spin current, respectively. Parameters $\boldsymbol{H}$ and $\boldsymbol{M}$ represent the external magnetic field and magnetization in the $Ni_{81}Fe_{19}$ layer. Reprinted with permission from Ref. [47] and Ref. [48].

Another breakthrough in studying SHE with bilayer structure is that the spin current due to SHE in some heavy nonmagnetic materials is large enough to switch the magnetic moment of the adjacent ferromagnetic layer. It draws lots of attention for the potential application in spintronics. A pioneering work is presented by Miron *et al.* about magnetic reversal of a perpendicular anisotropic cobalt dot induced by Rashba effect [49]. Also, Liu *et al.* demonstrated spin Hall induced spin transfer torque switching in perpendicularly magnetized Co/Pt [50] (as shown in Fig. 2.10) or CoFeB/Ta [51] bilayer system at room temperature. Liu *et al*. also presented the spin torque switching of an in-plane polarized magnet using a three-terminal spin Hall

device, where a MTJ nanopillar is patterned on top of the Ta layer [51]. The spin accumulation generated from SHE in Ta layer can be injected into the bottom CoFeB ferromagnetic layer of MTJ. And the MTJ structure can be switched between parallel and anti-parallel magnetization configurations for top and bottom ferromagnetic layers, by altering the direction of the injected charge current in Ta.

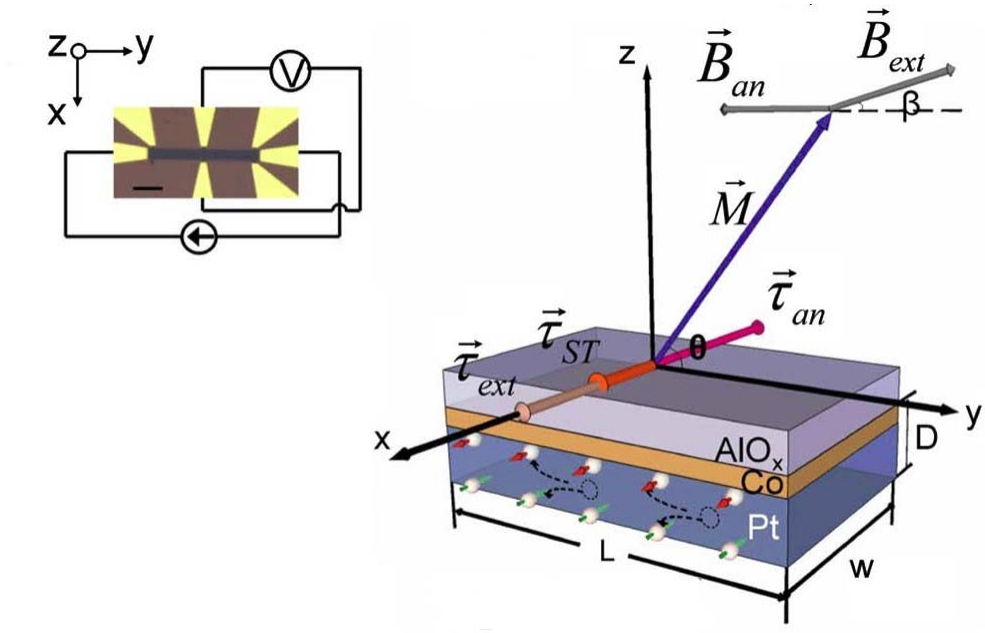

Figure 2.10: Illustration of spin Hall induced spin transfer torque switching in the Co/Pt bilayer structure. Reprinted with permission from Ref. [50].

At the same time, there are also extensive researches utilizing the mesoscopic nonlocal structures to explore SHE/ISHE. The most significant work comes from Valenzuela and Tinkham in 2006, who were the first to perform the direct electrical detection of ISHE in metallic structure as we mentioned earlier. The inset of Fig. 2.11 shows the measurement configuration. The Al cross is oxidized in pure oxygen to

form Al_2O_3 barrier, and ferromagnetic (FM) electrodes overlap with the Al strip. In the inverse spin Hall measurement, when a charge current flows from FM1 electrode to Al and away from the Hall cross, a pure spin current is injected into the Al strip across the FM1/Al interface. From the concept of a traditional NLSV, the spin current propagates from the injection point toward both directions along the Al channel. A voltage, which is the result of the conversion from pure spin current to a transverse charge current owing to ISHE, can be measured across Al Hall bar as shown in Fig. 2.11. An out-of-plane large magnetic field is used to align the spin direction in FM electrode. The spin Hall angle of Al is estimated to be around $1\sim3\times10^{-4}$ at 4.2 K [38].

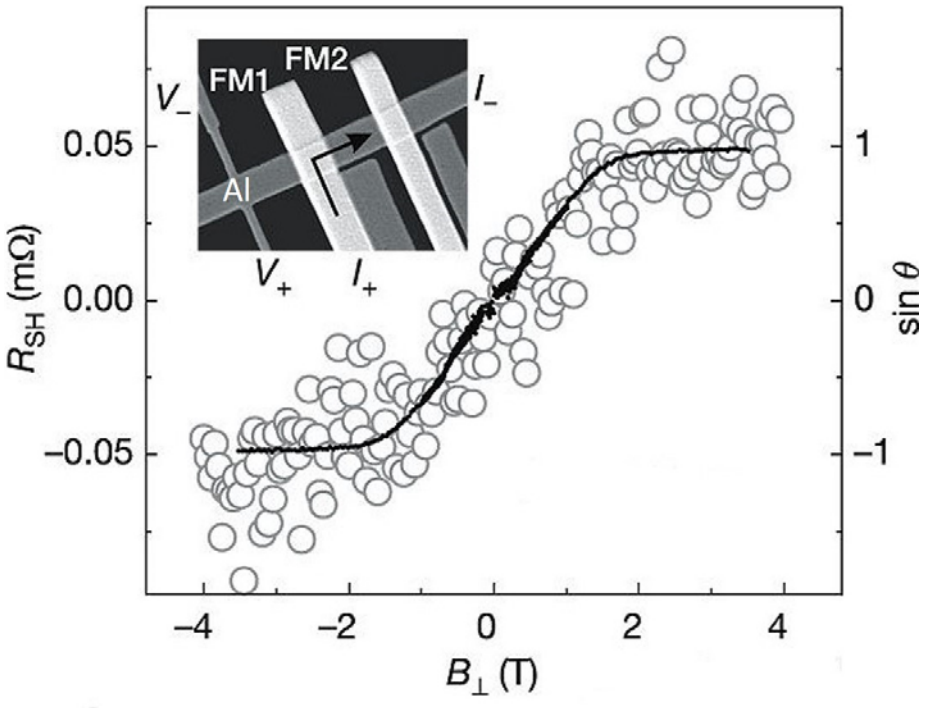

Figure 2.11: Spin Hall signal as a function of the external perpendicular magnetic field $B_\perp$. The inset is the scanning electron micrograph of the device with measurement configuration. Reprinted with permission from Ref. [38].

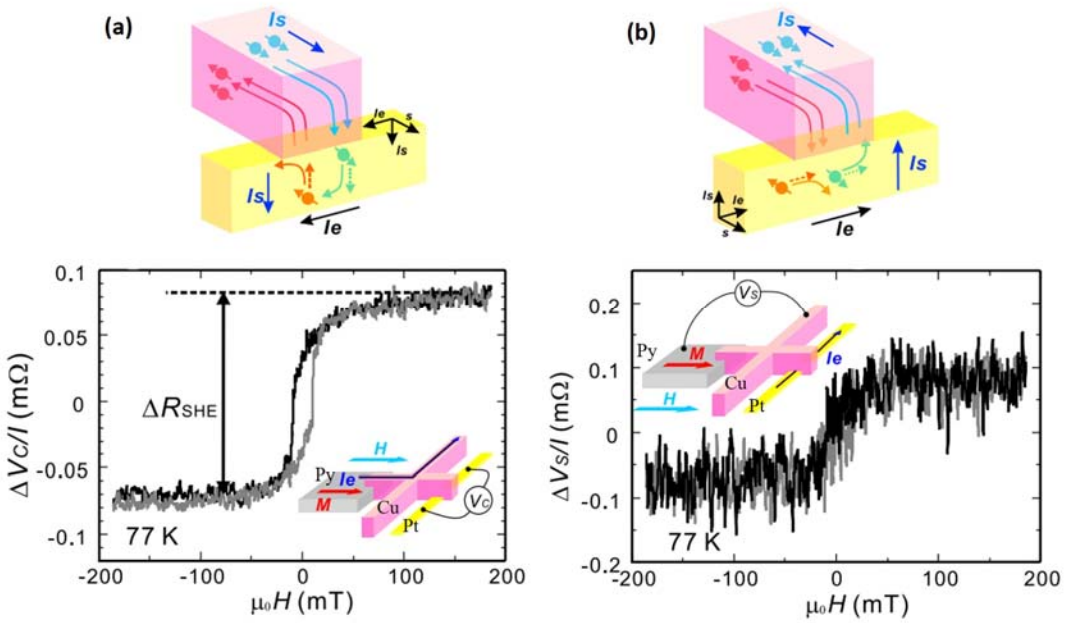

Figure 2.12: (a) Upper portion: schematic illustration of the ISHE process at Cu/Pt junction; lower portion: ISHE signal as a function of external magnetic field. The inset is the ISHE measurement configuration. (b) Upper portion: schematic illustration of the SHE process at the Cu/Pt junction; lower portion: SHE as a function of external magnetic field. The inset is the SHE measurement configuration. Parameters $\boldsymbol{I_e}$ and $\boldsymbol{I_s}$ denote charge current and pure spin current. Parameters $\boldsymbol{M}$ and $\boldsymbol{H}$ denote the magnetization direction of Py layer and applied external magnetic field. Reprinted with permission from Ref. [39].

In 2007, Kimura *et al.* reported the electrical detection of ISHE and SHE in nanoscale Pt wire using lateral nonlocal spin valve structure at both room temperature and 77 K. The lateral device consists of a Py pad, a Pt wire and a Cu cross, shown in the insets of Fig. 2.12. For the ISHE measurement, the charge current is injected from the Py pad into Cu cross, inducing a pure spin current in Cu, which is directed into Pt wire. The absorbed spin current in Pt is perpendicular to the device plane, therefore the direction of the induced charge current due to ISHE in Pt is along the Pt wire and

the charge voltage is detected over two ends of Pt wire. The external magnetic field alters the magnetization direction of Py and changes the polarity of the charge voltage in Py as shown in Fig. 2.12 (a). The SHE can also be measured in the same device. When the charge current is injected through Pt wire, it induces the spin accumulation on the surface of Pt. The spin accumulation on the top surface drives the spin across the Cu/Pt interface into Cu channel. The Py in this case works as a spin detector, controlled by the external magnetic field. As shown in Fig 2.12 (b), when the spins in Py is aligned parallel to the spin accumulation in Cu channel, it shows a high signal; when in anti-parallel configuration, a low magnitude of signal is obtained. The same magnitude of ISHE and SHE signal demonstrates that SHE and ISHE are reciprocal processes, and verifies the Onsager relation [39].

2.3.2 Anomalous Hall Effect (AHE)

AHE in ferromagnetic metals (e.g. Py) shares the same mechanism as SHE in nonmagnetic metals. Unlike SHE that generates a transverse pure spin current, AHE deflects uneven number of electrons with opposite spins to opposite directions, which produces both spin current and charge current as shown in Fig. 1.2 (b). The polarity of the charge accumulation along the edges depends on the magnetization direction of the ferromagnet. The reciprocal process of AHE has the same scenario as ISHE in nonmagnet, which is shown in Fig. 1.2 (d), and it converts a pure spin current into a charge current.

Previous relevant work has been conducted in the context of ISHE in ferromagnetic thin film, using a bilayer structure with Py and ferromagnetic insulator yttrium iron garnet (YIG). A pure spin current from YIG is produced by a temperature gradient via spin Seebeck effect (SSE) [52, 53], or by the microwave excitation via

spin pumping [54]. Then a charge voltage is generated as the pure spin current propagates through Py because of the ISHE. Fig. 2.13 shows the bilayer system, with which the first observation of ISHE in Py is demonstrated by Miao *et al*. By applying an out-of-plane temperature gradient to the Py/YIG bilayer sample, a pure spin current is generated in YIG and injected towards Py. Owing to the ISHE, a charge voltage in transverse direction developes in Py. However, as illustrated in Fig. 2.13 (a), in addition to ISHE, the anomalous Nernst effect (ANE) also exists in Py under the applied thermal gradient. The total observed signal is the superposition of ISHE and ANE. Thus, supplementary structures are made by inserting an insulating layer (I) between Py and YIG as shown in Fig. 2.13 (b). It blocks the transmission of the spin current across the interface between YIG and Py layer. Therefore, with a temperature gradient, only the ANE can be detected. The difference between Py/YIG and Py/I/YIG samples provides an accurate measurement that is contributed by ISHE in Py [52].

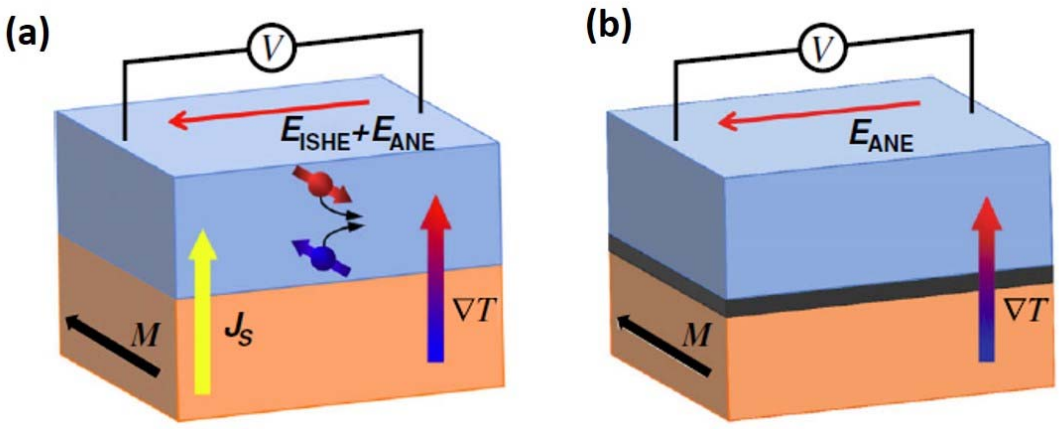

Figure 2.13: Illustrations of (a) Py/YIG bilayer structure and (b) Py/insulator/YIG structure under a perpendicular temperature gradient. Reprinted with permission from Ref. [52].

REFERENCES

[1] J. J. Thomson, Philosophical Magazine **44** (1897).

[2] G. E. Uhlenbeck and S. Goudsmit, Naturwissenschaften **13** (47), 953 (1925).

[3] G. E. Uhlenbeck and S. Goudsmit, Nature **117**, 264 (1926).

[4] P. A. M. Dirac, Proceedings of the Royal Society of London Series A **117** (778), 610 (1928).

[5] M. Johnson and R. H. Silsbee, Physical Review Letters **55** (17), 1790 (1985).

[6] M. N. Baibich, J. M. Broto, A. Fert, F. N. Vandau, F. Petroff, P. Eitenne, G. Creuzet, A. Friederich and J. Chazelas, Physical Review Letters **61** (21), 2472 (1988).

[7] G. Binasch, P. Grunberg, F. Saurenbach and W. Zinn, Physical Review B **39** (7), 4828 (1989).

[8] A. Fert and I. A. Campbell, Physical Review Letters **21** (16) (1968).

[9] A. Fert, Journal of Physics Part C Solid State Physics **2** (10) (1969).

[10] C. Kittel, *Introduction to Solid State Physics*, 8th Ed. (John Wiley & Sons, Inc., New York, 2004).

[11] P. Grunberg, R. Schreiber, Y. Pang, M. B. Brodsky and H. Sowers, Physical Review Letters **57** (19), 2442 (1986).

[12] N. H. Mott, Proceedings of the Royal Society A **156** (888), 368 (1936).

[13] N. H. Mott, Proceedings of the Royal Society A **153** (880), 699 (1936).

[14] M. Julliere, Physics Letters A **54** (3), 225 (1975).

[15] J. C. Slonczewski, Physical Review B **39** (10), 6995 (1989).

[16] T. Miyazaki and N. Tezuka, Journal of Magnetism and Magnetic Materials **139** (3), L231 (1995).

[17] J. S. Moodera, L. R. Kinder, T. M. Wong and R. Meservey, Physical Review Letters **74** (16), 3273 (1995).

[18] X. F. Han and T. Miyazaki, Journal of Materials Science & Technology **16** (6), 549 (2000).

[19] X. F. Han, M. Oogane, H. Kubota, Y. Ando and T. Miyazaki, Applied Physics Letters **77** (2), 283 (2000).

[20] H. X. Wei, Q. H. Qin, M. Ma, R. Sharif and X. F. Han, Journal of Applied Physics **101** (9), 3 (2007).

[21] W. H. Butler, X. G. Zhang, T. C. Schulthess and J. M. MacLaren, Physical Review B **63** (5), 12 (2001).

[22] J. Mathon and A. Umerski, Physical Review B **63** (22), 4 (2001).

[23] S. S. P. Parkin, C. Kaiser, A. Panchula, P. M. Rice, B. Hughes, M. Samant and S. H. Yang, Nature Materials **3** (12), 862 (2004).

[24] S. Yuasa, T. Nagahama, A. Fukushima, Y. Suzuki and K. Ando, Nature Materials **3** (12), 868 (2004).

[25] S. Ikeda, J. Hayakawa, Y. Ashizawa, Y. M. Lee, K. Miura, H. Hasegawa, M. Tsunoda, F. Matsukura and H. Ohno, Applied Physics Letters **93** (8), 3 (2008).

[26] M. Johnson and R. H. Silsbee, Physical Review B **37** (10), 5312 (1988).

[27] F. J. Jedema, A. T. Filip and B. J. van Wees, Nature **410** (6826), 345 (2001).

[28] F. J. Jedema, H. B. Heersche, A. T. Filip, J. J. A. Baselmans and B. J. van Wees, Nature **416** (6882), 713 (2002).

[29] Y. Ji, A. Hoffmann, J. S. Jiang, J. E. Pearson and S. D. Bader, Journal of Physics D: Applied Physics **40** (5), 1280 (2007).

[30] H. Zou and Y. Ji, Applied Physics Letters **101** (8), 4 (2012).

[31] S. Garzon, I. Zutic and R. A. Webb, Physical Review Letters **94** (17), 4 (2005).

[32] Y. Fukuma, L. Wang, H. Idzuchi, S. Takahashi, S. Maekawa and Y. Otani, Nature Materials **10** (7), 527 (2011).

[33] T. Kimura, Y. Otani and J. Hamrle, Physical Review Letters **96** (3), 4 (2006).

[34] T. Yang, T. Kimura and Y. Otani, Nature Physics **4** (11), 851 (2008).

[35] H. Zou, X. J. Wang and Y. Ji, Journal of Applied Physics **108** (3), 4 (2010).

[36] A. Slachter, F. L. Bakker, J. P. Adam and B. J. van Wees, Nature Physics **6** (11), 879 (2010).

[37] M. Erekhinsky, F. Casanova, I. K. Schuller and A. Sharoni, Applied Physics Letters **100** (21), 4 (2012).

[38] S. O. Valenzuela and M. Tinkham, Nature **442** (7099), 176 (2006).

[39] T. Kimura, Y. Otani, T. Sato, S. Takahashi and S. Maekawa, Physical Review Letters **98** (15), 156601 (2007).

[40] M. I. Dyakonov and V. I. Perel, JETP Letters **13** (11), 467 (1971).

[41] M. I. Dyakonov and V. I. Perel, Physics Letters A **35** (6), 459 (1971).

[42] J. E. Hirsch, Physical Review Letters **83** (9), 1834 (1999).

[43] J. Sinova, D. Culcer, Q. Niu, N. A. Sinitsyn, T. Jungwirth and A. H. MacDonald, Physical Review Letters **92** (12), 4 (2004).

[44] J. Smit, Physica **24** (1), 39 (1958).

[45] L. Berger, Physical Review B **2** (11), 4559 (1970).

[46] Y. K. Kato, R. C. Myers, A. C. Gossard and D. D. Awschalom, Science **306** (5703), 1910 (2004).

[47] E. Saitoh, M. Ueda, H. Miyajima and G. Tatara, Applied Physics Letters **88** (18), 182509 (2006).

[48] K. Ando, S. Takahashi, K. Harii, K. Sasage, J. Ieda, S. Maekawa and E. Saitoh, Physical Review Letters **101** (3), 036601 (2008).

[49] I. M. Miron, G. Gaudin, S. Auffret, B. Rodmacq, A. Schuhl, S. Pizzini, J. Vogel and P. Gambardella, Nature Materials **9** (3), 230 (2010).

[50] L. Q. Liu, O. J. Lee, T. J. Gudmundsen, D. C. Ralph and R. A. Buhrman, Physical Review Letters **109** (9), 096602 (2012).

[51] L. Q. Liu, C. F. Pai, Y. Li, H. W. Tseng, D. C. Ralph and R. A. Buhrman, Science **336** (6081), 555 (2012).

[52] B. F. Miao, S. Y. Huang, D. Qu and C. L. Chien, Physical Review Letters **111** (6), 5 (2013).

[53] H. Wu, C. H. Wan, Z. H. Yuan, X. Zhang, J. Jiang, Q. T. Zhang, Z. C. Wen and X. F. Han, Physical Review B **92** (5), 6 (2015).

[54] H. L. Wang, C. H. Du, P. C. Hammel and F. Y. Yang, Applied Physics Letters **104** (20), 4 (2014).

Chapter 3

EXPERIMENTAL TECHNIQUES

In this chapter, we will review the sample fabrication and measurement techniques in our work.

3.1 Microlithography

The fabrication of electronic devices in a mesoscopic scale requires a variety of chemical and physical processes performed on a semiconductor (e.g., silicon) substrate. The basic to all processes is lithography, which is printing micro/nano-scale images on the substrate for subsequent transfer of the pattern to the substrate.

To fabricate the nanoscale non-local structures, two kinds of lithography methods are used in this work: (1) photolithography, creating the external contact pads for wire bonding and electron beam (e-beam) lithography alignment marks; (2) e-beam lithography, fabricating nanoscale devices connected to the contact pads.

3.1.1 Photolithography

Photolithography is a process that transfers the pattern to the photosensitive polymer (a photoresist) by exposure to a UV light through a photomask. A photomask typically consists of opaque patterns (chrome or iron oxide) on a transparent quartz support. Fig. 3.1 shows contact pads with alignment marks in the scale range from 5 μm to 400 μm after photolithography process.

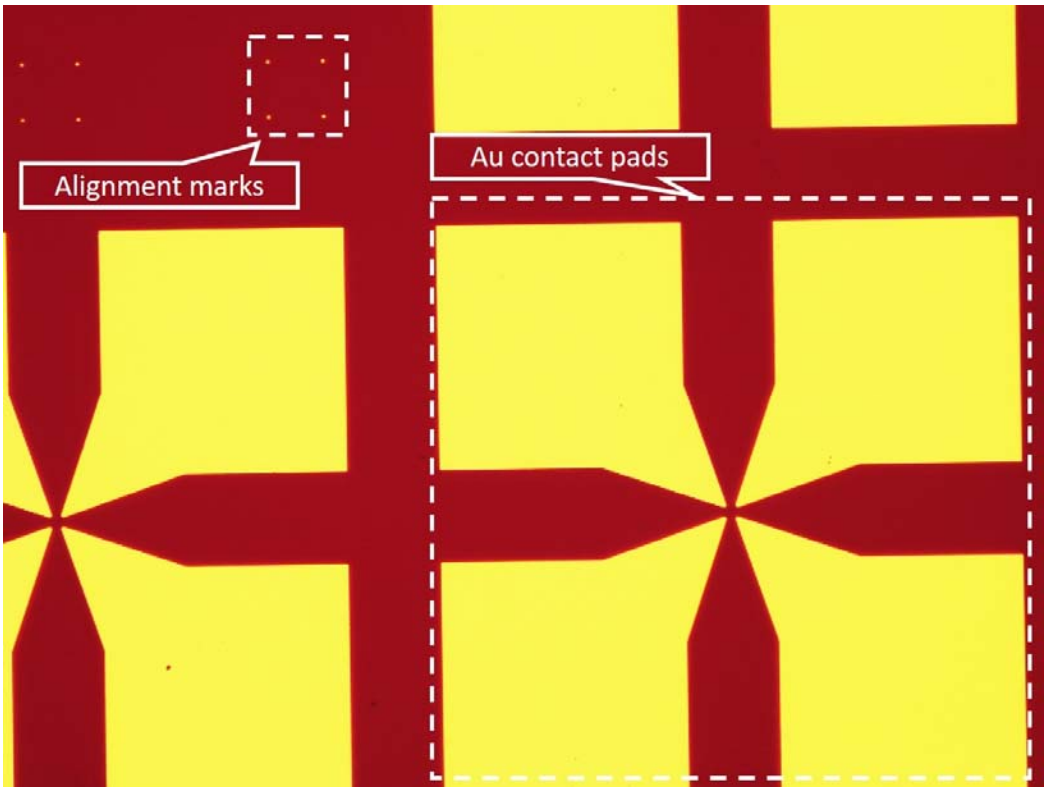

Figure 3.1: Au contact pads and alignment marks under optical microscope.

A set of photolithography process steps is illustrated in Fig. 3.2. In our work, the 2-inch silicon wafer covered with 200 nm Si_3N_4 is used as the substrate. First, substrate cleaning and preparation [Fig. 3.2 (a)] is intended to improve the adhesion of the photoresist to the substrate. The silicon wafer is cleaned in an ultrasonic cleaner with acetone, ethanol and deionized (DI) water in sequence for 15 minutes each, and followed by rinsing with acetone, ethanol and DI water sequentially and blowing dry with N_2 gas. It removes organic or inorganic contaminations on the surface. Then, a viscous, liquid solution of the positive photoresist (AZ 1512) [1] is dispensed to the surface of the substrate via spin coating at 3000 rpm for one minute. After pre-baking on a hot plate at 115 ˚C for 65 s, it forms a uniform thin resist layer [Fig. 3.2 (b)] ~ 1.4

μm thick. Subsequently, the wafer is placed on the mask aligner (OAI Model 200) to write patterns on the photomask to the photoresist [Fig. 3.2 (c)]. After careful alignment, the wafer is exposed to UV light through the photomask for 6 s. AZ 1512 is a positive photoresist, which means the area exposed by UV light under a transparent part of the photomask will have a chemical change and become soluble in the photographic developer. Right after the light exposure, the wafer is dipped into the developer (MF 319) for 20-30 s to dissolve exposed photoresist [Fig. 3.2 (d)].

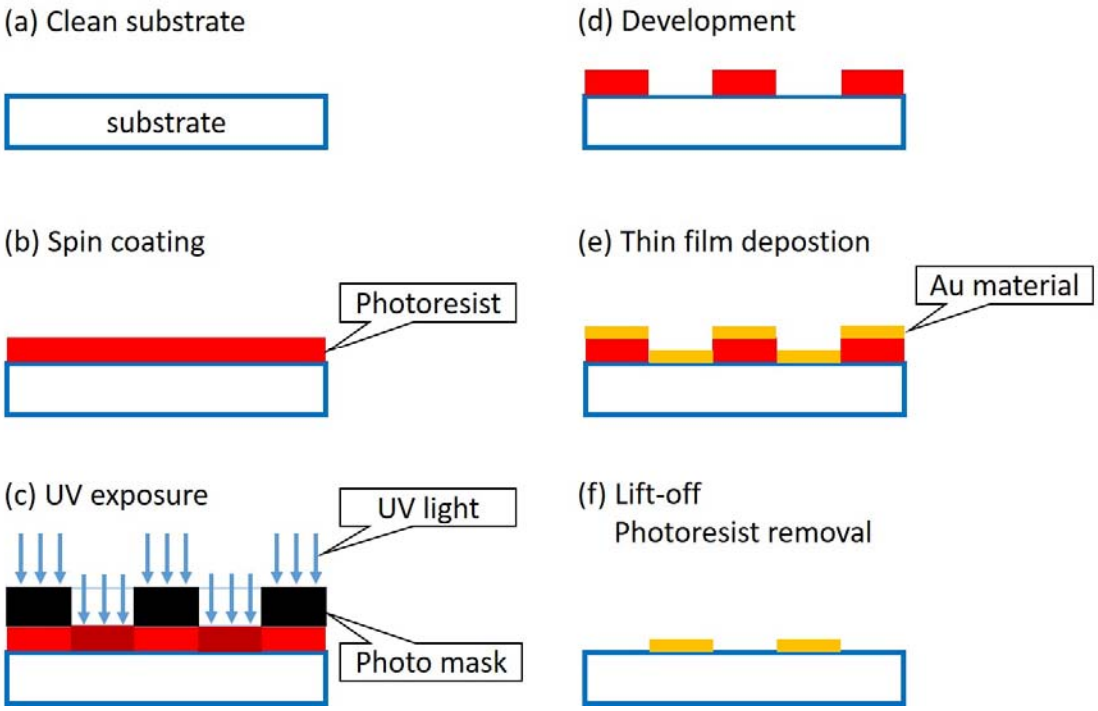

Figure 3.2: Flow chart of photolithography. (a) substrate cleaning; (b) spin coating of photoresist; (c) exposure with photo mask by UV light; (d) development with developer; (e) deposition of Au thin film; (f) Lift-off for photoresist removal.

After the development, the wafer is coated with 80 nm of Au material through magnetron sputtering [Fig. 3.2 (e)]. The substrate is then soaked in acetone for several hours and ultrasonic for 5-10 s, flush the substrate with acetone, ethanol, DI water and blow dry with N_2 gas. In this "lift-off" process [Fig. 3.2 (f)], the remaining photoresist and unneeded material are completely removed, only leaving the Au patterns printed on the substrate.

3.1.2 Electron-beam Lithography (EBL)

Unlike photolithography that requires physical photo masks, electron-beam lithography (EBL) is a direct writing technique that uses an accelerated beam of electrons to pattern features on the substrates that have been coated with the electron beam sensitive resist (e-beam resist) [2]. The solubility of the e-beam resist changes when exposed to the electron beam, and enables selective removal of either exposed (positive resist) or non-exposed regions (negative resist) by immersing it in a developer. ELB is a great tool for the nanostructure fabrication because of its high resolution below 10 nm, and flexibility and efficiency in pattern modification and line-width control, etc.

3.1.2.1 EBL System – Raith e-LiNE

In this work, the electron beam lithography was performed on the Raith e-LiNE system at the University of Maryland NanoCenter shown in Fig. 3.3. The e-LiNE consists of the following subsystems [3]:

(1). The electron optical column with thermionic field emission filament. It controls the focusing position and the intensity of the electron beam.

(2). Deflection system with scan generators for lithography and SEM imaging.

(3). High precision X-Y-Z stage equipped with Laser interferometer for X-Y positioning and automated height sensing. It controls the high-precision movement of the sample/substrate to be processed.

(4). Vacuum system and plinth. It controls the vacuum degree at the electron optical system, the lithography chamber housing stage, and the specimen changing chamber (load lock) according to the required steps of the lithography operation.

(5). PC-based lithography user interface. It processes the control of lithography applications, SEM imaging and functions for Metrology.

Figure 3.3: Raith e-LiNE machine at University of Maryland NanoCenter.

The heart of the EBL system is the electron optical control and deflection system as shown in Fig. 3.4. The electron emitter in the electron gun generates electrons with a large current density. When passing through a set of electromagnetic lenses and deflector, the electron beam is correspondingly modified so that the beam spot diameter is reduced to less than 2 nm and correctly focused onto the substrate.

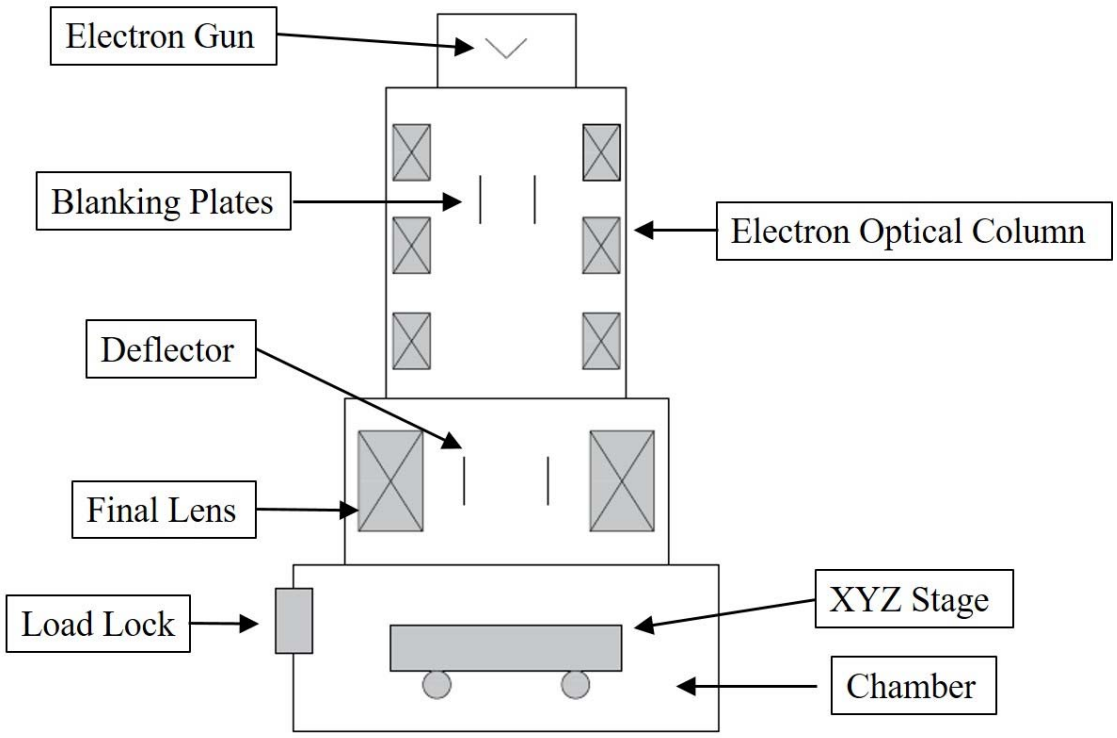

Figure 3.4: Schematic of electron optical control and deflection system in electron beam lithography system.

Before operating under EBL system, ELPHY Quantum software is used to design the device pattern, as shown in Fig. 3.5. The rectangles, polygons and lines

with red outlines are the designed structures to write using EBL. This software is the GDSII databased and comparable to the EBL system. Therefore, the structures can be designed and exposed within the same software platform making it unnecessary to switch between different software packages for multiple tasks.

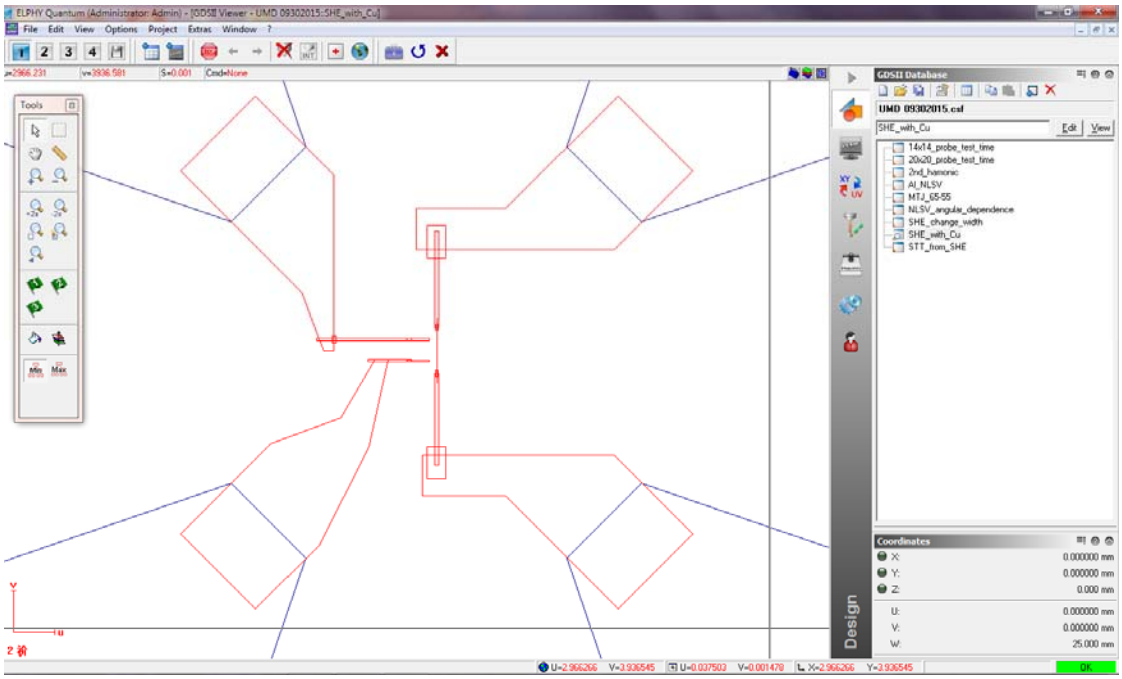

Figure 3.5: EBL pattern design in ELPHY Quantum software.

3.1.2.2 Operation of Raith e-LiNE

The operation of electron beam writing includes following steps: sample loading via load lock, electron beam optimization, stage adjustment, write field alignment, exposure (e-beam writing) and sample unloading [4].

To load the sample, place the sample holder with the sample on the robot arm of the load lock and close the chamber door. The sample loading via load lock is

automated. At the end of the loading procedure, the user can choose the accelerating voltage and aperture to start.

With a proper working distance, a clear SEM image is obtained by focusing. Use joystick to drive the X-Y-Z stage to the desired position and choose a small feature on the sample less than 1 μm. By adjusting the magnification, focusing, aperture and stigmation correction, the electron beam can be further optimized to form a sharp image.

The stage adjustment allows navigation with a blanked beam on the sample to find the exposure area without pre-exposing. There are two coordinate systems: XYZ for the stage and UVW for the sample. The aim of stage adjustment is to find the relationship between XYZ and UVW with respect to shift, scaling and rotation in order to perform a permanent coordinate transformation between both systems. A few steps are involved in the stage adjustment. (1) Angle correction: make the axes of the sample surface parallel to the axes of the stage; (2) origin correction: compensate the different origins between XYZ and UVW coordinates; (3) 3-point adjustment: further adjust the coordinate transformation.

The write field alignment is to adjust the electrostatic deflections system inside the column so that the beam can be precisely controlled by the lithography software respect to UVW coordinate. It's a very important task as it aligns the write field to the sample coordinate UVW. In the stage adjustment, we performed a point navigation in sample coordinate UVW, but the image via the column software was still parallel to XYZ at a certain point and non-parallel to UVW. For pattern stitching it is essential that the write field is exactly parallel to UVW and this can be achieved with the write field alignment.

In the exposure step, the beam current is measured on the Faraday cup. The area exposure dose for the pattern can be calculated by the dwell time, beam current and exposed area as the formula shown below:

$$Dose = \frac{Dwell\ Time \times Beam\ Current}{Area\ Exposed} = \frac{Dwell\ Time \times Beam\ Current}{(Step\ Size)^2} \quad (3.1)$$

To create fine lines with small dimensions less than 100 nm, the line exposure will be also used. Table 3.1 shows a typical set of Raith e-LiNE system parameters we used in our work.

Table 3.1: Raith e-LiNE system parameters.

Accelerating Voltage	**Aperture**	**Working Distance**	**Beam Current**
20 kV	30 μm	10 mm	0.27 nA

	Area	**Line**
Step Size	0.02 μm	0.01 μm
Dwell Time	0.0035 ms	0.015 ms
Beam Speed	5.5 mm/s	0.7 mm/s
Dose	245 μC/cm^2	4000 pC/cm

After the exposure, the samples can be unloaded via load lock through the automated system.

3.1.2.3 Shadow Mask: Double-layer Electron Beam Resist

Two kinds of electron beam resist are used in this work to form the double-layer shadow mask: PMGI (polydimethyl glutarimide) as the bottom layer and PMMA (polymethyl methacrylate) as the top layer. The pre-patterned Au contact pad wafer is used as substrate. The spin coating process of these two electron beam resists is

illustrated in Fig. 3.6 (a). Firstly, PMGI resist is spin coated at 3000 rpm for 60 s, then baked at 210 ˚C for 3 mins on the hot plate, which forms a 360 nm thick resist layer. Secondly, on the top of PMGI layer, PMMA is spin coated at 5000 rpm for 60 s and baked at 190 ˚C for 4 mins and it gives rise to a 160 nm thick top layer.

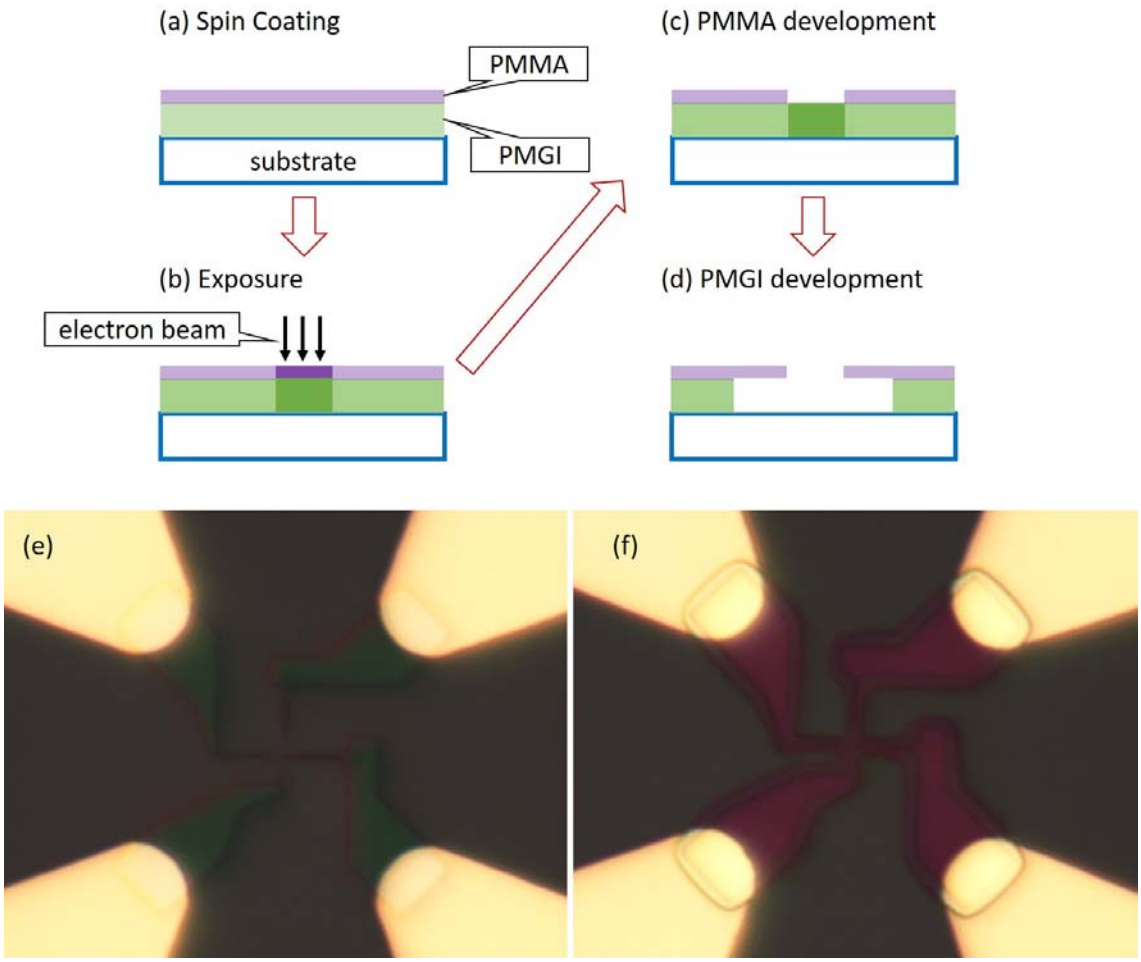

Figure 3.6: (a) Spin coating with double layer electron beam resists PMGI and PMMA; (b) Exposure under EBL system; (c) development of PMMA layer; (d) development of PMGI layer; optical microscope pictures after (e) PMMA development and (f) PMGI development.

After exposed in EBL system with designed pattern as shown in Fig. 3.6 (b), we develop the two resist layers with different developers. For the development of top PMMA layer, the wafer is dipped in the MIBK: IPA 1:3 solvent for 90 s and followed by IPA for 30 s [Fig. 3.6 (c)]. After rinsed with DI water, the wafer is then soaked in XP101A (PMGI developer) for 5-6 mins, which helps the development of the bottom PMGI layer [Fig. 3.6 (d)]. Because the PMGI has a higher e-beam sensitivity and longer development time than PMMA, resulting in a top layer mask suspended from the overdeveloped bottom layer. The undercut area can be controlled by the development time of PMGI resist. Fig. 3.6 (e) shows the trenches after PMMA development under optical microscope, and the dark green area is where the PMMA layer is removed. In Fig. 3.6 (f) as the image after the development of both layers, two parallel lines along the edge can be clearly seen indicating the suspended shadow mask. The advantage using double-layer shadow masks to fabricate nanoscale devices will be discussed in the Section 3.2.3.

3.2 Thin Film Deposition

We fabricate the nanoscale non-local spintronic devices by angle deposition through shadow masks. The magnetic and non-magnetic materials are deposited on the patterned substrate by electron beam (e-beam) evaporator in the ultra-high vacuum system. In this section, we will discuss the details of the e-beam evaporation system and associated techniques.

3.2.1 High Vacuum Chamber

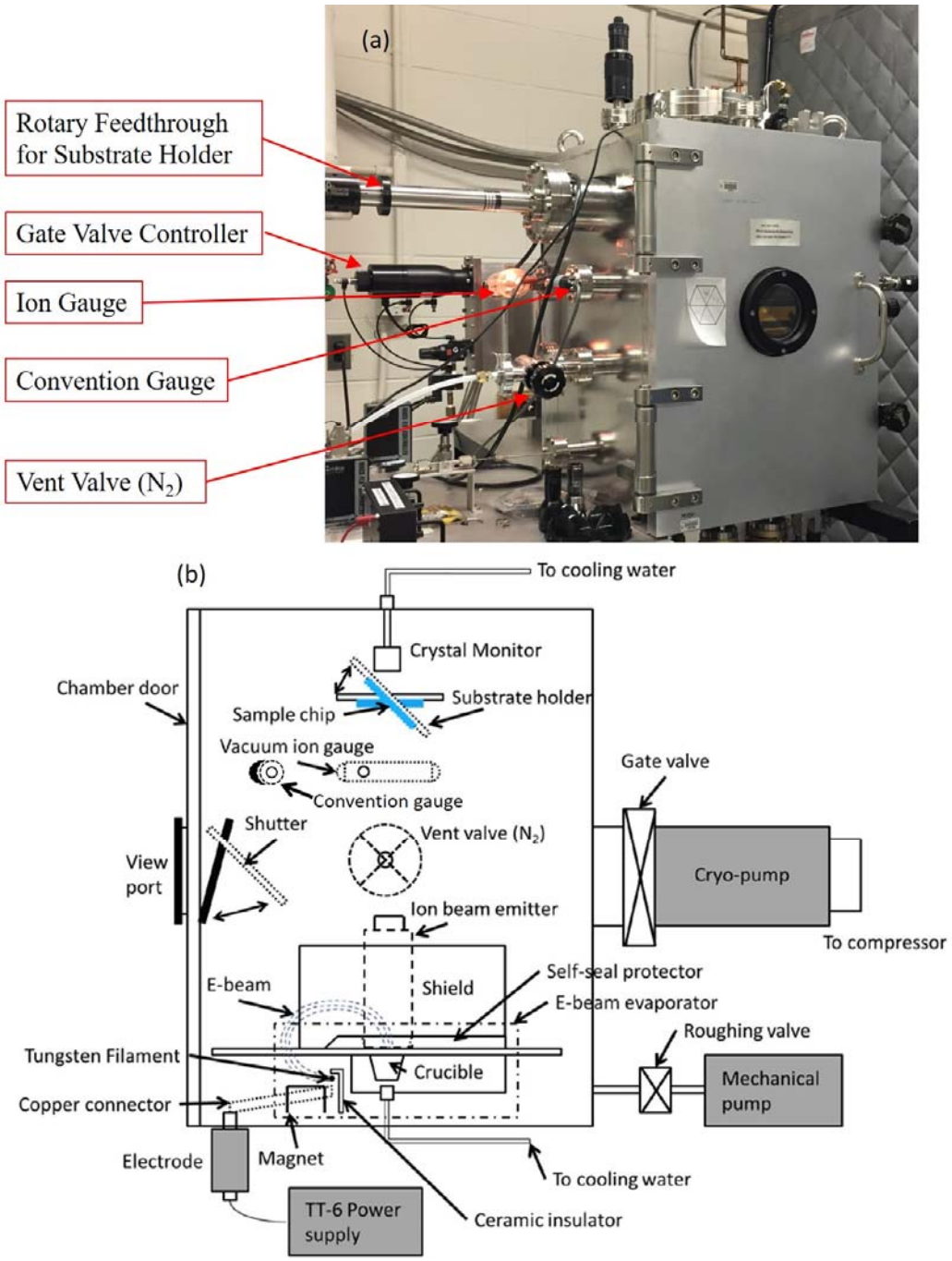

Figure 3.7: (a) vacuum chamber in Ji's group; (b) schematic drawing of the vacuum chamber from right side view.

Fig. 3.7 (a) shows the self-design and home-built high vacuum chamber in our laboratory. The vacuum system consists of three major components: the main chamber, the roughing mechanical pump and the cryogenic pump. Details are shown schematically in Fig. 3.7 (b). In order to evacuate the chamber to a high vacuum level, it's necessary to establish an insulating vacuum around the cryogenic pump first. So, the mechanical pump is firstly used to pump down the chamber to the pressure of 10^{-2} Torr range through the three-way valve. Then, the high vacuum is achieved and maintained by the cryopump, usually around 2×10^{-8} Torr. At this time, the gate valve attached to the cryopump is open, making it connected to the main chamber. However, the gate valve should stay closed to isolate the cryo-pump and leave it running before the main chamber is exposed to ambient pressure. The pressure in the chamber can be monitored by the convention gauge (1×10^{-4} to 1,000 Torr) and the ion gauge (1×10^{-4} to 1×10^{-9} Torr).

The electron beam evaporator is located at the bottom of the chamber with cooling water system, and we will discuss the details in the next section. The wafer/substrate can be placed on the substrate holder right above the e-beam source, and the holder is mounted to a 360-degree rotary feedthrough to control the deposition directions. The thickness crystal monitor on the top of the chamber gives real-time monitor for the material deposition rate and thickness. Also, there's an ion beam emitter of the left side of e-beam evaporator, which is used as a dry etching method. We can watch all the vacuum and deposition process from the view port on the front door, and the port is protected by a piece of rotatable flat copper shutter. When the deposition is in process, the shutter is titled down to avoid material deposition onto the view port.

3.2.2 Electron Beam Evaporation

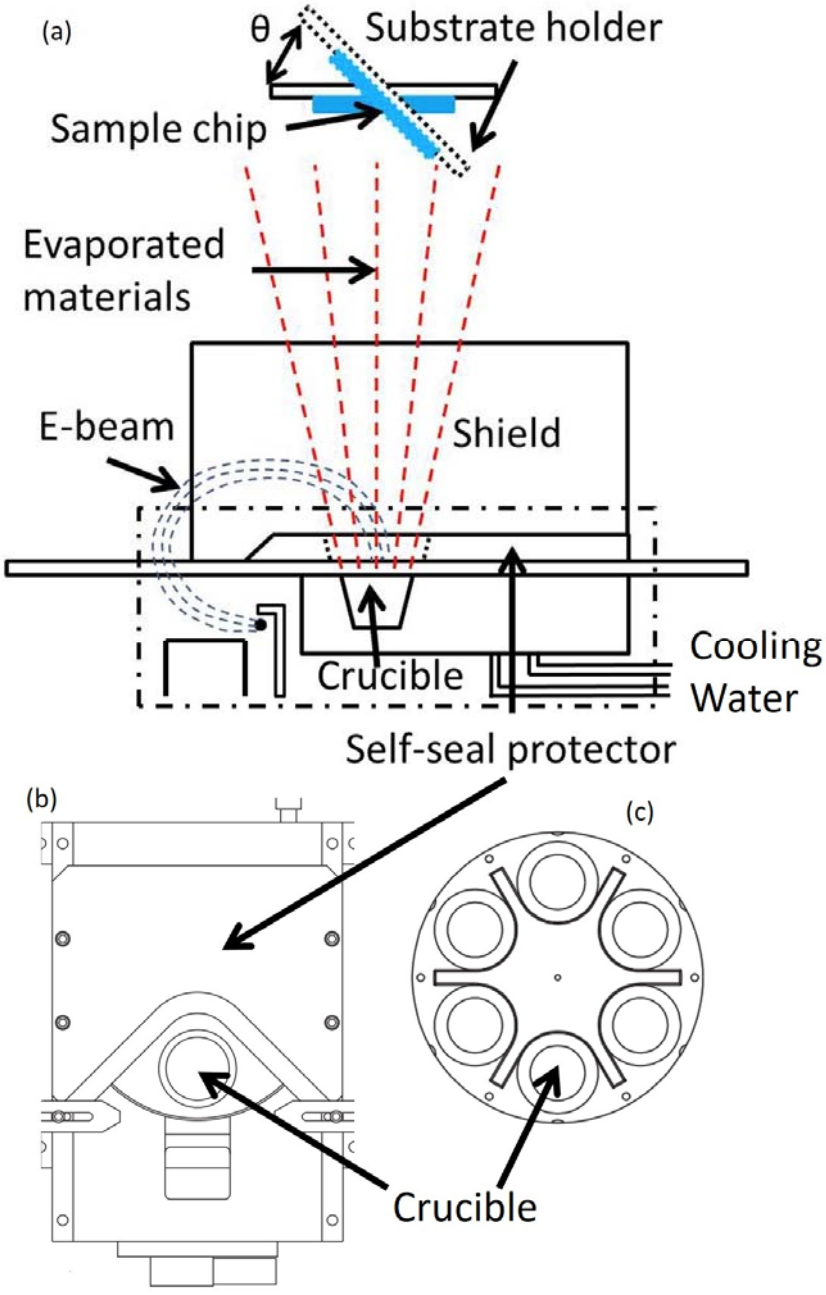

Figure 3.8: (a) The schematic drawing of the electron beam evaporation system; (b) top view of the e-beam source; (c) 6-pocket crucibles under self-seal protector.

The Telemark electron beam evaporation system is installed in the chamber, and it includes the following components as shown at the bottom part of Fig. 3.7 (b): a power supply, a system controller, a tungsten filament to emit electrons, the confocal electromagnetic system, crucibles for evaporation materials, the cooling water system, and the substrate holder.

The evaporation must be operated under a pressure below 10^{-5} Torr. As seen in Fig. 3.8 (a), a large current is sent through the filament and heats it until the emission of electrons takes place. The filament is located outside the evaporation zone that avoids contamination. The emitted electrons are then directed and focused by the confocal electromagnetic system to form a beam that hits the surface of the evaporant. When the beam strikes the surface, the kinetic energy of the electrons is transformed into thermal energy, and it heats up and vaporizes the target materials, then subsequently evaporated materials condense on all surfaces. Since there are lots of electrons in the beam, the overall thermal energy released is quite high. Therefore, it requires that the crucibles which holds the target materials must be water cooled to keep it from melting [5]. The sample (wafer) is attached on the rotatable substrate holder with Kapton tapes and kept facing upward to prevent any deposition onto the sample. When a certain deposition rate is reached and stable, one can quickly rotate the holder to a downward position so that the evaporated materials hits the sample surface directly or from an oblique angle. When a desired thickness is reach, the holder is flipped upward again. The deposition rate and film thickness can be monitored simultaneously by the crystal monitor assembled on the top of the chamber. The relationship between the actual deposition thickness on the substrate and the one on crystal monitor is given by:

$$Film\ thickness =$$

$$Film\ thickness\ on\ monitor \times \left(\frac{Distance\ from\ target\ to\ monitor}{Distance\ from\ target\ to\ substrate}\right)^2 \times cos\theta \qquad (3.2)$$

where θ is the angle at which the evaporated material hits the sample surface.

The e-beam source in our lab is equipped with 6-pocket crucibles that is shown in Fig. 3.8 (c) and it is able to hold 6 different materials. The crucibles are covered with a self-seal protector which only allows one target materials to be exposed at a time as illustrated in Fig. 3.8 (b) and it helps to avoid cross-contamination. The crucibles can be easily switched by the chain-driven handle through a feedthrough at the bottom of the chamber.

3.2.3 Angle Deposition through Shadow Mask

We have introduced the double-layer shadow mask with e-beam resists in section 3.1.2.3. In this part, we will discuss the fabrication process of a nanoscale Py/Cu non-local spin valve with multiple angle deposition through shadow mask.

Fig. 3.9 (a) shows the top view of the shadow mask (PMMA layer), there are two lateral open slits and one vertical slit. The width of the vertical opening is about 100 nm. Because of the overdeveloped bottom PMGI layer, the PMMA layer acts as a freestanding mask suspended from the PMGI layer. The angle deposition procedures are illustrated in Fig. 3.9 (b)-(e). First, Py are deposited through the lateral slits from two different oblique angles, forming two ferromagnetic electrodes on the substrate. Due to the narrow width of the vertical slit, the atomic flux of Py is blocked by the side wall of the PMMA resist, thus there is no Py deposition through it. Then, AlO_x and Cu are deposited from the normal direction in sequence [6]. It forms two Py/AlO_x/Cu interfaces and a Cu channel connecting two Py electrodes. All depositions

are finished in one vacuum cycle, which ensure the purity of the materials and the cleanness of the interfaces.

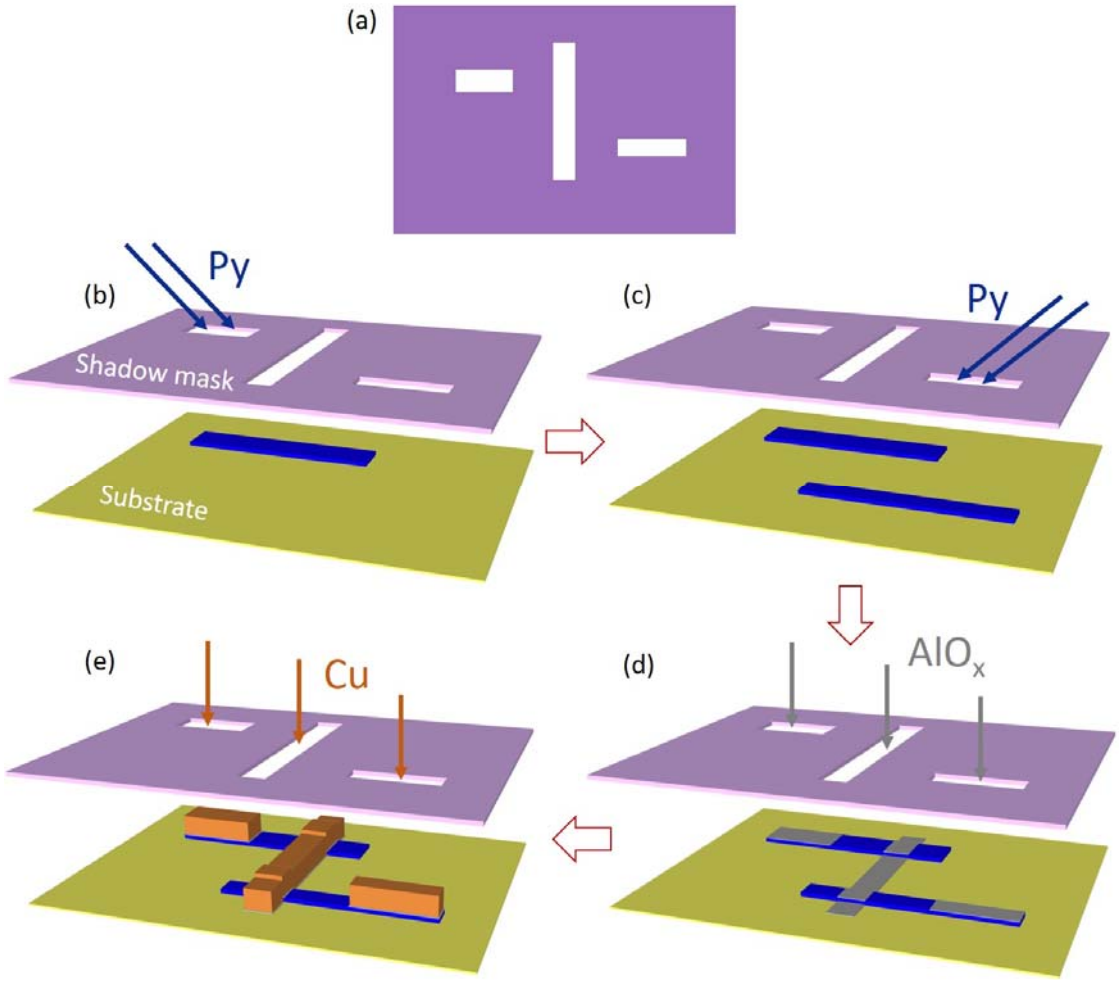

Figure 3.9: (a) Top view of shadow mask; (b)-(e) the flow chart of angle deposition.

3.3 Measurement Techniques

3.3.1 Cryogenic System with Variable Temperature Controller

In this work, samples are placed in the Janis Research PTSHI-950 Refrigerator System (Fig. 3.10 (a)) to perform the electrical measurements. This closed cycle cryogenic system is designed to operate from 4.5 K to room temperature. The system consists of the following parts:

(1). Compressor (not shown in Fig. 3.10) manufactured by Sumitomo Heavy Industries with a remote valve unit and a cold head.

(2). An exchange gas sample tube with an insulating vacuum jacket. The vacuum jacket is equipped with a bellows sealed evacuation valve, which allows evacuating and sealing the jacket to a pressure of 10^{-5} Torr or less. Better vacuum levels provide greater insulation, therefore shorter cooldown times and lower final temperature.

(3). A sample positioner assembly as shown in Fig. 3.10 (b). It can be inserted into or removed from the sample tube vertically from the top. The sample holder is mounted at the bottom of the positioner, and Helium exchange gas can transfer heat from the sample to the refrigerator, cooling the sample in the process. There are two electrical feedthroughs on the top of the positioner: one is the connector to the electronic measurement setups for the sample (it will be introduced in Section 3.3.3); the other connects between the heater (Heater B) on the sample mount and the temperature controller.

(4). An automatic temperature controller with dual heater outputs. It provides the temperature setpoint within the range of 5 K – 300 K.

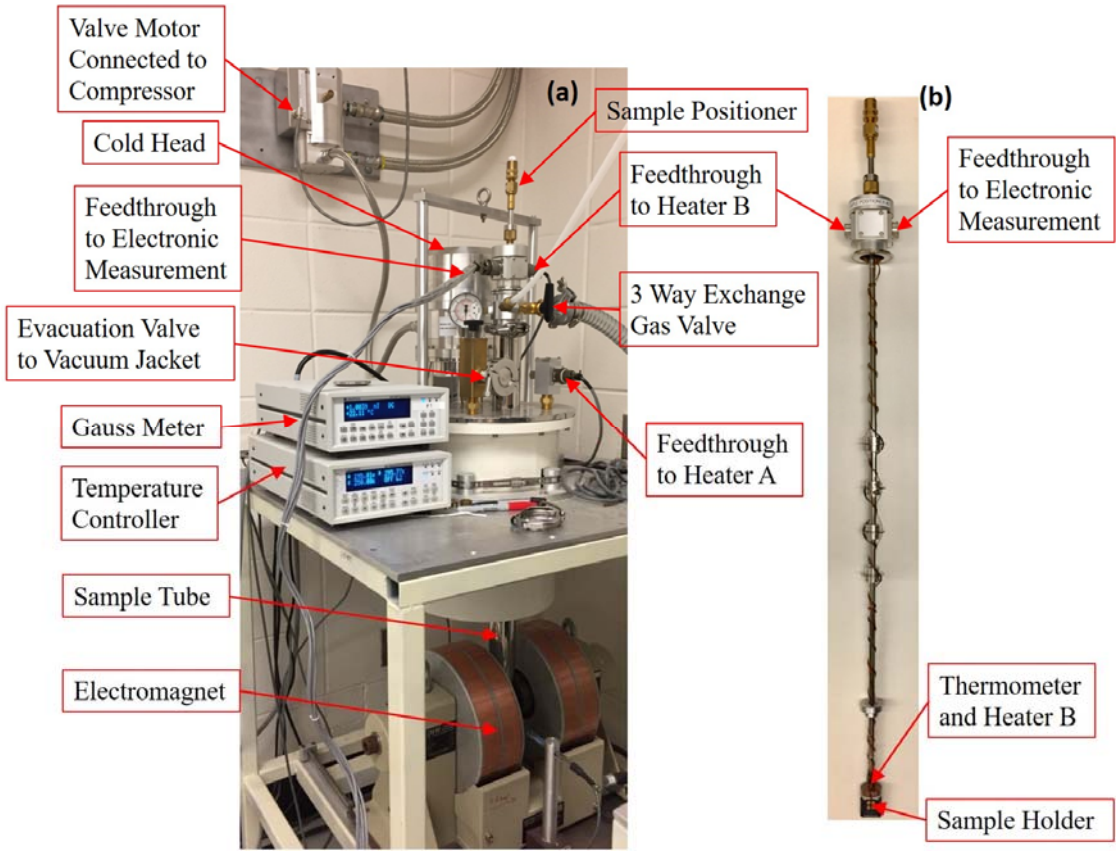

Figure 3.10: (a) Janis PTSHI-950 Refrigerator system;(b) Sample positioner assembly.

A 3-way exchange gas valve is located near the top of the sample tube. One end connects to the pure Helium gas source and the other end is equipped with a mechanical pump. It is used to introduce or remove Helium exchange gas. When loading the sample positioner into the sample tube, the valve is firstly switched to the Helium gas side to vent the tube. It allows the Helium gas to flow into the sample tube while loading and prevents air and moisture from entering the tube. After the positioner is loaded, switch the valve to the mechanical pump side. It evacuates the tube to a pressure of 10^{-3} Torr. Then, measurements can be taken through the electrical feedthroughs on top of the positioner. Low temperature measurements can also be

achieved by turning on the compressor. After a couple of hours' operation, the cryogenic system will reach the temperature around 4.5 K.

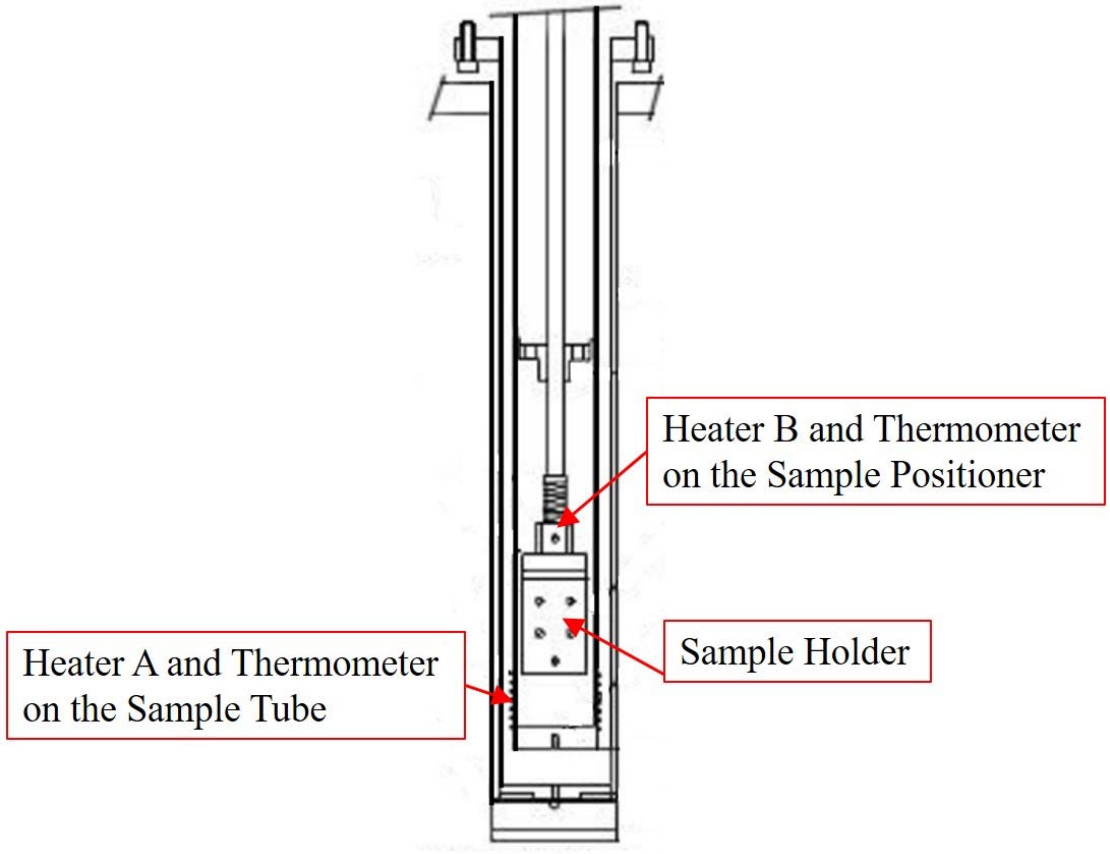

Figure 3.11: Schematic drawing of the sample tube with sample positioner inside (lower part).

For the operation of various temperatures, two sets of heater and thermometer are installed on the cryostat, as illustrated in Fig. 3.11. One set is installed at the bottom of sample tube as Heater A with maximum 100 W output power. It controls the Helium exchange gas temperatures and heats the sample indirectly through the

contact with the exchange gas. The sample is surrounded by an isothermal gas, therefore the temperature is more uniform. However, it takes a long time to stabilize, particularly at high temperature. The other set is installed on the sample mount of the positioner as Heater B (25 W output). The sample can be directly heated up by the conduction of the heat through the Cu sample holder. The advantage of this method is that it can achieve a temperature change more fast. But the disadvantage is the uncertainty involved in the temperature measurement, since the sample is surrounded by the exchange gas that is at a different temperature from the sample mount. Using both heaters will combine the advantages and reduce disadvantages. Both heaters and thermometers are wired to the feedthroughs either on the top of the sample tube or the positioner. And they are connected to the Lakeshore 322 temperature controller to monitor and control the temperature on the sample [7].

3.3.2 Electromagnets

The external magnetic field used in this work is supplied by GMW variable gap electromagnet (Model 5403), as shown in Fig. 3.12. Two coils with a fixed 86 mm separation are connected to the KEPCO bipolar power supply. It produces the magnetic field by tuning the current through the coils. Since the coils are equipped with the cooling water system, the maximum current that can be applied to each coil is as high as 20 A. A cylindrical pole is inserted into each coil to assure the uniformity of the magnetic field between the pole gap. And the direction of the magnetic field is pointing from one pole to the other as the red arrow labeled as “field” in Fig. 3.12. The pole gap is adjustable in a range from 0 mm to 86 mm, and has been adjusted to a certain distance to accommodate the situation that the sample holder in the lower part of the sample tube can be just placed at the center of the gap. In this case, the

maximum magnetic field is about 0.5 T. A Hall probe with Lakeshore 455 DSP Gauss meter is placed next to the sample tube, which measures the magnitude and direction of the magnetic field applied to the sample.

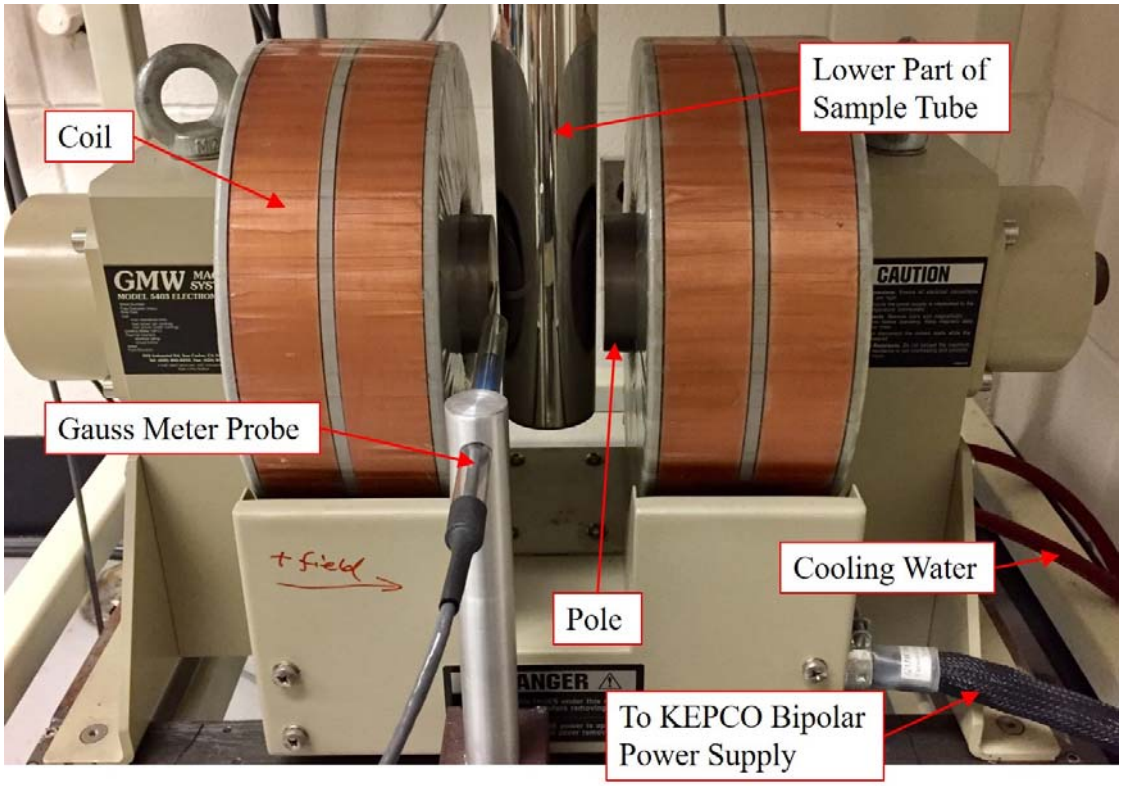

Figure 3.12: GMW variable gap electromagnet with cooling water system.

3.3.3 Electronic Measurement Setups

Devices are wire bonded to the contact pins of the sample holder, which is placed at the end of the positioner in the cryogenic system, and then can be measured via the electrical feedthrough on the positioner.

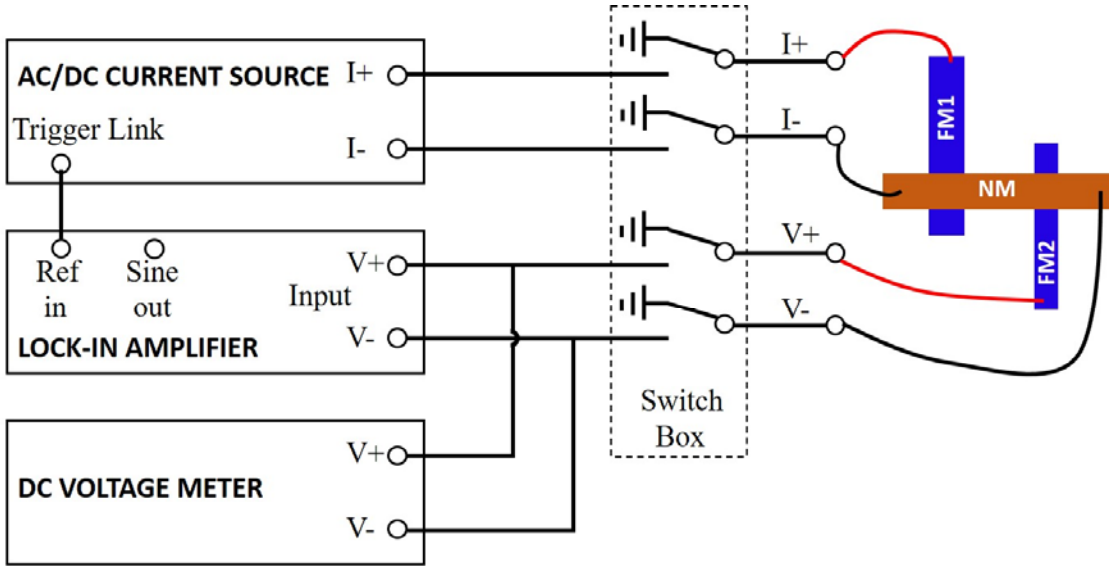

Figure 3.13: Schematic circuit diagram of the 4-terminal measurement setups.

Fig. 3.13 shows the electronic measurement setup for a NLSV device. In our lab, we use Stanford Research System SR830 DSP Lock-in Amplifier, Keithley 6221 Low Noise Precision AC/DC Current Source and Keithley 2182A Nanovoltmeter as electronic instruments. To obtain a low noise nonlocal spin signal, an *a.c.* current is injected from the FM1(ferro-magnetic) electrode to one end of the NM(non-magnetic) channel, and the nonlocal *a.c.* voltage (with the same frequency of the injected *a.c.* current) is detected between FM2 electrode and the other end of the NM channel by the lock-in amplifier. It requires a 4-terminal measurement system: two as the current output and the other two as the voltage-detecting input. The SR830 Lock-in Amplifier itself has an internal *a.c.* output from "Sine out" channel, that can be converted into an *a.c.* current source. But for the convenience of switching between *a.c.* and *d.c.* current, we use Keithley 6221 as an external current source instead. When using 6221 to

provide a tunable sine output current, a cable is connected between the “Trigger Link” of 6221 and “Ref in” of SR830 to reference the frequency to the lock-in amplifier. If the resistance of the interface or electrode needs to be measured, 6221 can be used as a *d.c.* current source, and 2182A Nanovoltmeter is then connected into the setup to read the *d.c.* voltage.

Before connecting electronic instruments to the device, each measurement terminal (*I*+, *I*-, *V*+, *V*-) is controlled by a 2-way toggle switch through a switch box. It has two states: “grounding” and “connected”. During the measurement, the switches are put into “connected” state. While the devices are not being measured, the switches are in “grounding” state. It protects the device from static discharge so that it won’t damage the device.

REFERENCES

[1] *AZ 1500 Series Product Data Sheet*.

[2] http://lnf-wiki.eecs.umich.edu/wiki/Electron_beam_lithography.

[3] *Raith e-LiNE Technical Description*.

[4] *Raith e-Line Operation Manual*.

[5] https://en.wikipedia.org/wiki/Electron_beam_physical_vapor_deposition.

[6] Y. Ji, A. Hoffmann, J. E. Pearson and S. D. Bader, Applied Physics Letters **88** (5), 052509 (2006).

[7] *Operating Instruction for the Janis Research PTSHI-950 Refrigerator System*.

Chapter 4

SPIN HALL EFFECTS IN MESOSCOPIC PT FILMS WITH HIGH RESISTIVITY

4.1 Introduction

Spin Hall effects (SHE) and inverse spin Hall effects (ISHE) have stimulated broad interest and debates in the field of spintronics [1-7]. The ability to create a robust pure spin current without magnetic materials is intriguing, and the simplicity and efficiency of this approach is desirable for potential technological applications. Owing to the spin-orbit coupling in heavy nonmagnetic metals such as Pt, a charge current j induces a spin current j_s in the transverse direction. The conversion rate is described by a spin Hall angle $\alpha_H = j_s/j = \sigma_H\rho$, where ρ is the electrical resistivity and σ_H is the spin Hall conductivity. For a fixed amount of j_s, The Joule heating power density in the material is $j^2\rho = j_s^2/(\sigma_H^2\rho)$. Apparently increasing the ρ while maintaining the σ_H leads to an enhanced energy efficiency. The spin diffusion length λ is also a crucial quantity. For a film that is thicker than λ, only a depth of λ near the surface contribute to the SHE meaningfully.

There are mainly two types of experimental systems to quantify α_H and λ: the bilayer structure of a ferromagnetic metal and a heavy nonmagnetic metal and the mesoscopic nonlocal structure. The bilayer structures are more actively pursued and allow for a variety of experiments. These include spin pumping [8, 9], spin Hall ferromagnetic resonance [10, 11], spin Hall torque [12-14], and spin Seebeck effect [15]. The less explored mesoscopic nonlocal structure [1-3, 16] takes advantage the

nonlocal spin injection and detection methods [17, 18] that involve ferromagnetic electrodes and a nonmagnetic channel (e.g. Cu). Either the SHE or the ISHE can be explored for a heavy nonmagnetic metal (e.g. Pt) that is in contact with the Cu channel.

The bilayer and nonlocal structures involve different physical processes and provide complementary aspects of the SHE/ISHE. In the nonlocal method, the ferromagnetic metal and the Pt are physically separated and therefore other phenomena such as proximity effects or Rashba effect are avoided. The challenge to the nonlocal method, however, is the proper evaluation of various charge and spin transport parameters in the structure. These parameters include spin diffusion length and resistivity values of the Pt film and the Cu channel, the resistance of the Pt/Cu interface, and the spin injection or detection polarization of the ferromagnet. Ex-situ measurements conducted on other samples may not reflect the in-situ values for the SHE/ISHE structures under investigation. In addition, proper quantification of the charge current shunting near the Pt/Cu interface is also crucial and controversy arises from a previous method [19-21].

In this chapter, we explore SHE/ISHE in mesoscopic Pt films using the nonlocal method. The lateral confinement of the films to ~ 230 nm widths gives rise to high electrical resistivity (150 – 300 μΩ•cm). The nonlocal SHE/ISHE structures consist of mesoscopic Pt films, Cu channels, Py (permalloy or $Ni_{81}Fe_{19}$ alloy) spin injector/detectors, and low-resistance AlO_x barriers. All relevant physical quantities are either measured directly in the SHE/ISHE structures or determined from in-situ supplementary structures fabricated on the same substrate. Extensive measurements (58 SHE/ISHE structures from 6 substrates with 4 different Pt thickness values) are

conducted to take into account of microstructure variations. The charge current shunting and the spin absorption near the Cu/AlO_x/Pt interfaces are consistently characterized by the interfacial resistance. A full quantitative model, based on diffusion equations and proper boundary conditions, is developed to take into account spin transport processes in various materials and interfaces throughout the structure. The effectiveness of the model is demonstrated by extracting the same values of $\alpha_H\lambda$ from two groups of SHE/ISHE structures that differ drastically in the physical sizes and the resistance of the Cu/AlO_x/Pt interfaces.

We use the product $\alpha_H\lambda$ as a figure of merit because it is less prone to errors than the individual values of α_H and λ. Either a larger α_H or a larger λ will enhance the transverse spin accumulation on the surface of Pt film that is thicker than λ. An underestimated λ results in overestimated α_H, and conversely an overestimated λ results in underestimated α_H. Furthermore, the $\alpha_H\lambda$ is equivalent to $\sigma_H\rho\lambda$, which is of certain universal quality. Because the σ_H is a constant value if the SHE is intrinsic, and the $\rho\lambda$ is also a constant value if the spin relaxation can be described by Elliot-Yafet model with a constant spin-flip probability [22]. Our data and analysis provide an upper limit (0.8 nm) of the λ_{pt} and a confident determination of $\alpha_H\lambda_{pt}$ for the resistive mesoscopic Pt films. The substantial value of $\alpha_H\lambda_{pt}$ suggests an efficient spin Hall process.

4.2 Sample Preparation and Measurement

For each sample, up to 196 mesoscopic metallic structures are fabricated on a 10 mm × 10 mm silicon substrate covered with 200 nm Si_3N_4. Four different types of structures are included and shown in the scanning electron microscope (SEM) pictures in Fig. 4.1. Fig. 4.1 (a) and (b) are both nonlocal SHE/ISHE structures. The ~ 280 nm

wide ferromagnetic electrode is made of Py and the ~ 85 nm wide nonmagnetic channel is made of Cu. The Pt stripe near the lower end of the Cu channel is ~ 230 nm in width. A directly evaporated AlO_x layer (3nm) is placed at both interfaces forming $Py/AlO_x/Cu$ and $Cu/AlO_x/Pt$ junctions.

The sizes of the $Cu/AlO_x/Pt$ junctions are different for Fig. 4.1 (a) and (b). Fig. 4.1 (a) illustrates a "small-overlap" SHE/ISHE structure, where the Cu channel and Pt stripe overlaps only near the edge the Pt stripe. The size of the interface is $< 50 \times 30$ nm^2, forming a "point-contact". Fig. 4.1 (b) illustrates a "full-overlap" SHE/ISHE structure, where the overlap size along x direction is comparable to the Pt width forming an interface of area $\sim 80 \times 200$ nm^2. The interfacial resistance (R_i) values of the small-overlap and full-overlap $Cu/AlO_x/Pt$ junctions are quite different, and will be useful in confirming the validity of our quantitative models. The center-to-center distance between the $Py/AlO_x/Cu$ and the $Pt/AlO_x/Cu$ junctions is defined as channel length L.

The thickness of Cu and Py is 110 nm and 12 nm, respectively. The relatively large Cu thickness is chosen to ensure long Cu spin diffusion lengths. In this work, Pt thickness of 4 nm, 6 nm, 10 nm and 12 nm has been used for 6 samples (substrates) including a total number of 58 SHE/ISHE structures. We will focus on the results from one sample with 6 nm Pt to illustrate the measurement and quantification method before addressing the dependence on the Pt thickness.

Fig. 4.1 (c) and (d) illustrate two types of supplementary structures fabricated in-situ on the same substrate with SHE/ISHE structures: the nonlocal spin valve (NLSV) [17, 18, 23-26] and the Pt resistivity structure, respectively. The NLSV structure consists of two Py electrodes (spin injector F_1 and spin detector F_2) and a Cu

channel. AlO_x barriers are placed at the interfaces forming Py/AlO_x/Cu junctions. The Pt resistivity structure is a mesoscopic Pt stripe with four electrical probes, with which the resistivity of Pt can be determined. The thickness values of Cu, Py, AlO_x, and Pt are the same as those of the SHE/ISHE structures on the same substrate, owing to the identical processes

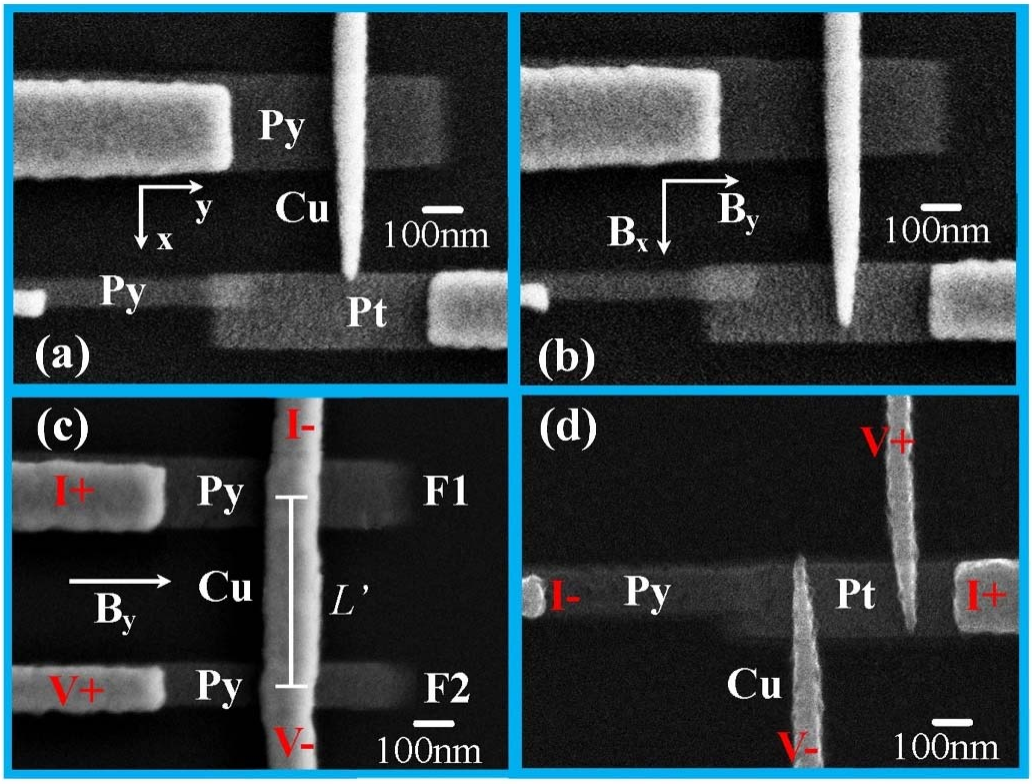

Figure 4.1: SEM pictures of SHE/ISHE structures with (a) small-overlap and (b) full-overlap. (c) SEM image of a nonlocal spin valve and measurement configuration is indicated. *L'* is the injector-to-detector distance. (d) A Pt resistivity measurement structure. All structures are fabricated on the same substrate through identical processes.

For each sample, all structures on the substrate are formed simultaneously by depositing Pt, Py, AlO_x, and Cu from different angles through a set of mesoscopic suspended shadow masks, which are created by electron beam (e-beam) lithography from two layers of e-beam resists: the PMGI (polydimethylglutarimide) resist on the bottom and the PMMA (polymethyl methacrylate) resist on the top. Details of the shadow mask and angle deposition method can be found in Chapter 3.2.3 and other literatures [3, 27-29].

The measurements of the 6 samples have been carried out either in a variable temperature probe station or in a pulse-tube variable temperature cryostat. All measurements are conducted at 10 K. The SHE and ISHE measurements from a structure with 6 nm Pt are shown in Fig. 4.2 (a) and (b), respectively, and the corresponding measurement configurations are shown in the insets. For SHE, the current is injected through the Pt stripe (+I on the right and –I on the left), and the nonlocal voltage is detected between Py (+V) and the upper end of Cu channel (-V). For the ISHE, the current flows from Py (+I) to the upper end of Cu (-I), and the nonlocal voltage is measured between the two ends of Pt stripe (+V on the left and –V on the right).

An alternating current (*a.c.*) of I_e = 0.1 mA with a frequency of 346.5 Hz is used as the injection current and the nonlocal *a.c.* voltage V_{nl} is detected by a lock-in detector. The nonlocal resistance, $R_s = V_{nl}/I_e$, is recorded as a function of the magnetic field B_x applied along the x direction, which is perpendicular to the Py electrodes. In both SHE and ISHE measurements, the R_s value reaches a high state for positive field but reaches a low state for negative field, and the difference between two states is ΔR_s = 0.7 mΩ. The polarity of the signals is consistent with previous

SHE/ISHE measurements in Pt [2, 3]. The equal magnitudes of ΔR_s for SHE and ISHE are expected because of Onsager reciprocal relations. Owing to its better signal-to-noise ratio, the ISHE measurements are used to extract the ΔR_s values. According to previously used conventions, the SHE/ISHE signal is defined as $\Delta R_{SHE} = \Delta R_s/2$ [2].

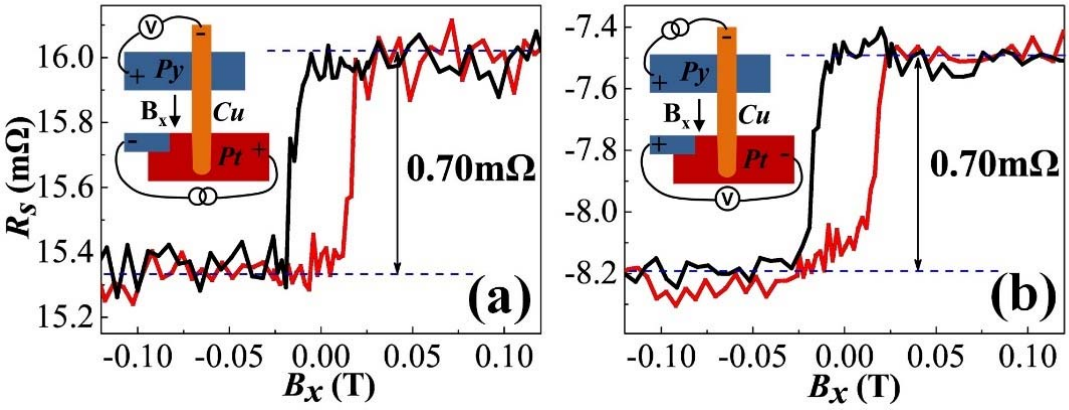

Figure 4.2: The R_s versus B_x curve of (a) a SHE measurement and (b) an ISHE measurement for the same structure with 6 nm Pt. The magnetic field is aligned parallel to Cu channel ($\pm x$ direction) and the temperature is 10 K.

The resistance R_i of the Cu/AlO_x/Pt interface is individually measured from each SHE/ISHE structure by sending a current from the top end of Cu to the right end of the Pt stripe and detecting a voltage between the Py and the left end of the Pt stripe. Various physical dimensions, as illustrated in Fig. 4.3 (a) for "small-overlap" and in (b) for "full-overlap", are individually characterized by SEM after the SHE/ISHE measurements. These quantities include width (w_{pt}) of Pt stripe, transport distance L between the center of the Py/AlO_x/Cu junction and the center of the Cu/AlO_x/Pt

junction, the width w_{cu} of the Cu channel, the length d of the Cu/AlO$_x$/Pt junction in the x direction, and the average width w_I of the Cu/AlO$_x$/Pt junction in the y direction. The tapering lower end of the Cu channel typically results in $w_I < w_{cu}$.

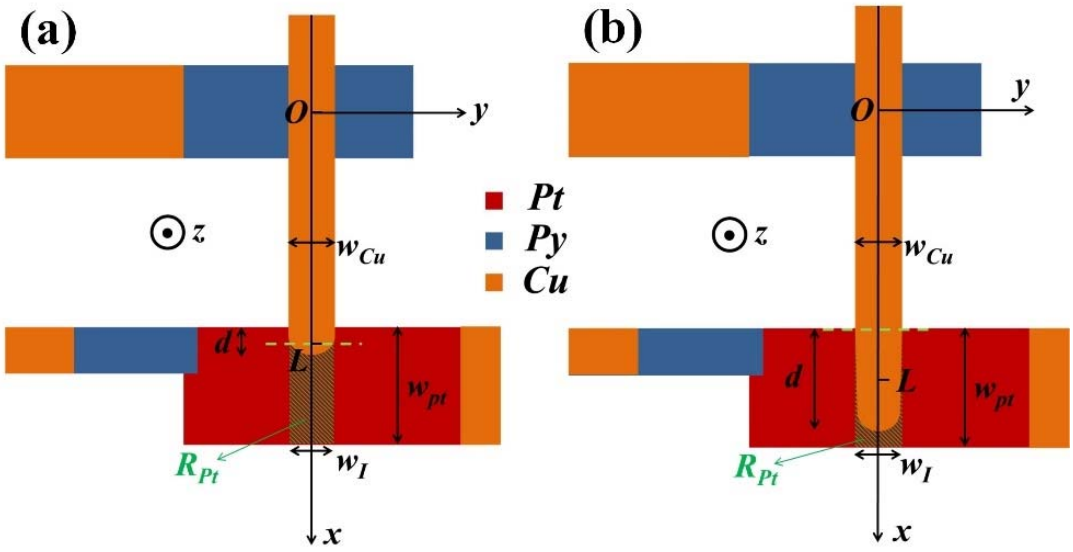

Figure 4.3: Top view of (a) the small-overlap and (b) full-overlap SHE/ISHE structure. The relevant physical dimensions are illustrated.

The effective spin polarization P of the Py/AlO$_x$/Cu interface, the spin diffusion length λ_{cu} of the Cu channel, and the resistivity ρ_{cu} of Cu are useful values for quantifying SHE/ISHE structures, and can be derived from the supplementary NLSVs on the same substrate. The R_s versus B_y curve of a NLSV is shown in Fig. 4.4, and the standard NLSV measurement configuration is illustrated in Fig. 4.1 (c). The magnetic field B_y is applied along the y direction, which is parallel to the F_1 and F_2 Py stripes. The field sweep alters the magnetizations of the F_1 and F_2 between parallel

states (high R_s) and antiparallel states (low R_s), and the difference ΔR_s is the NLSV spin signal.

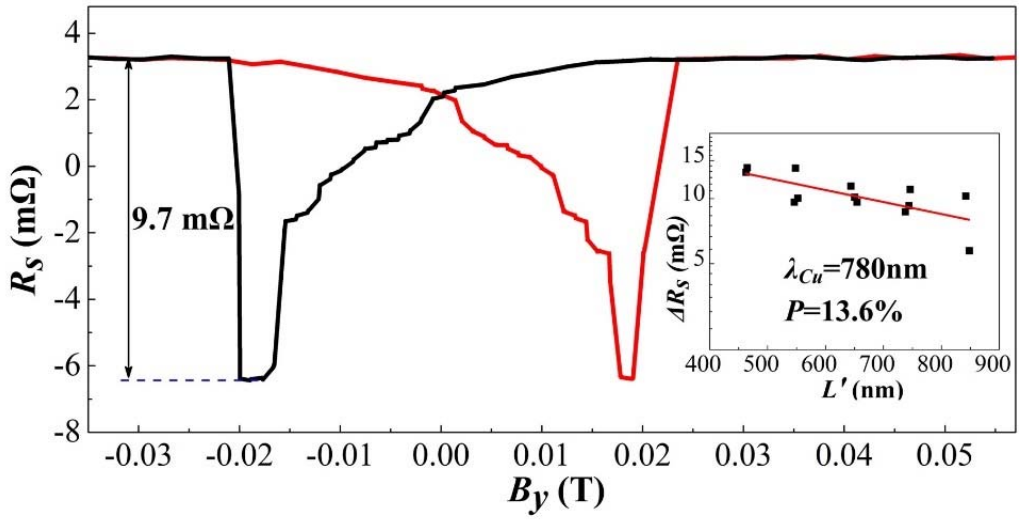

Figure 4.4: The R_s versus B_y curve at 10 K for a NLSV with magnetic field applied parallel to Py electrode ($\pm$ y direction). The ΔR_s versus L' and a fit (red solid line) is shown in the inset for a series of NLSVs on the same substrate.

In the inset of Fig. 4.4, the spin signals ΔR_s are plotted as a function of the center-to-center distance L' between the F_1 and the F_2. We fit the ΔR_s versus L' using $\Delta R_s = (P^2 \rho_{cu} \lambda_{cu} / A_{cu}') exp(-L'/\lambda_{cu})$ to extract the values of λ_{cu} and P, assuming that the two Py/AlO_x/Cu interfaces for F_1 and F_2 provide the same polarization P [17, 23, 30]. The cross-sectional area of the NLSV Cu channel is $A_{cu}' = t_{cu} w_{cu}'$, where $t_{cu} = 110$ nm and w_{cu}' are the Cu thickness and width, respectively, and w_{cu}' is measured by SEM. Here for the NLSVs, L' and w_{cu}' are used to be distinguished from

the channel length L and Cu width w_{cu} of the SHE/ISHE structures. In this set of data, the fitting yields P = (13.6 ± 2.6) % and λ_{cu} = (780 ± 220) nm at 10 K.

As described in other works, the precise determination of either P or λ_{cu} is nontrivial [31, 32]. The overestimate of one value leads to the underestimate of the other, and vice versa. However, the truly relevant quantity for later analysis (in Eq. 4.3 and 4.4) is the spin current that flows down the channel and it scales with $Pexp(-L/\lambda_{cu})$. This quantity is less uncertain than the individual values of P or λ_{cu} [31]. From the data in the inset of Fig. 4.4, this quantity for L = 500 nm is determined to be $Pexp(-L/\lambda_{cu})$= (0.072 ± 0.005), which has less uncertainty than individual values of P or λ_{cu}.

To obtain the resistivity value of Cu, the Cu resistance R_{cu} can be determined by sending in a current through the Cu channel and detecting voltages between F_1 and F_2. Then the resistivity ρ_{cu} can be calculated from R_{cu}, L' and A_{cu}'. For each sample, 10 - 15 NLSVs are used to obtain the P, λ_{cu}, and ρ_{cu}.

The resistivity of mesoscopic Pt stripes is measured using the supplementary structures shown in Fig. 4.1 (d). Note that the widths of these Pt stripes are the same as those in the SHE/ISHE structures. For each sample, 5 – 10 Pt stripes are measured for resistivity and the average value is used as the ρ_{pt} of that sample. The values of ρ_{pt} are generally in the range of 150 μΩ•cm < ρ_{pt} < 300 μΩ•cm, and this is a factor of 5 to 10 larger than that of extended films. The large resistivity is due to the reduced lateral dimension and thickness. The ΔR_{SHE}, R_i, L, w_{pt}, w_{cu}, and w_I values from each SHE/ISHE structure and the values of P, λ_{cu}, ρ_{cu}, and ρ_{pt} from supplementary structures will be used for quantitative analysis of ISHE signals.

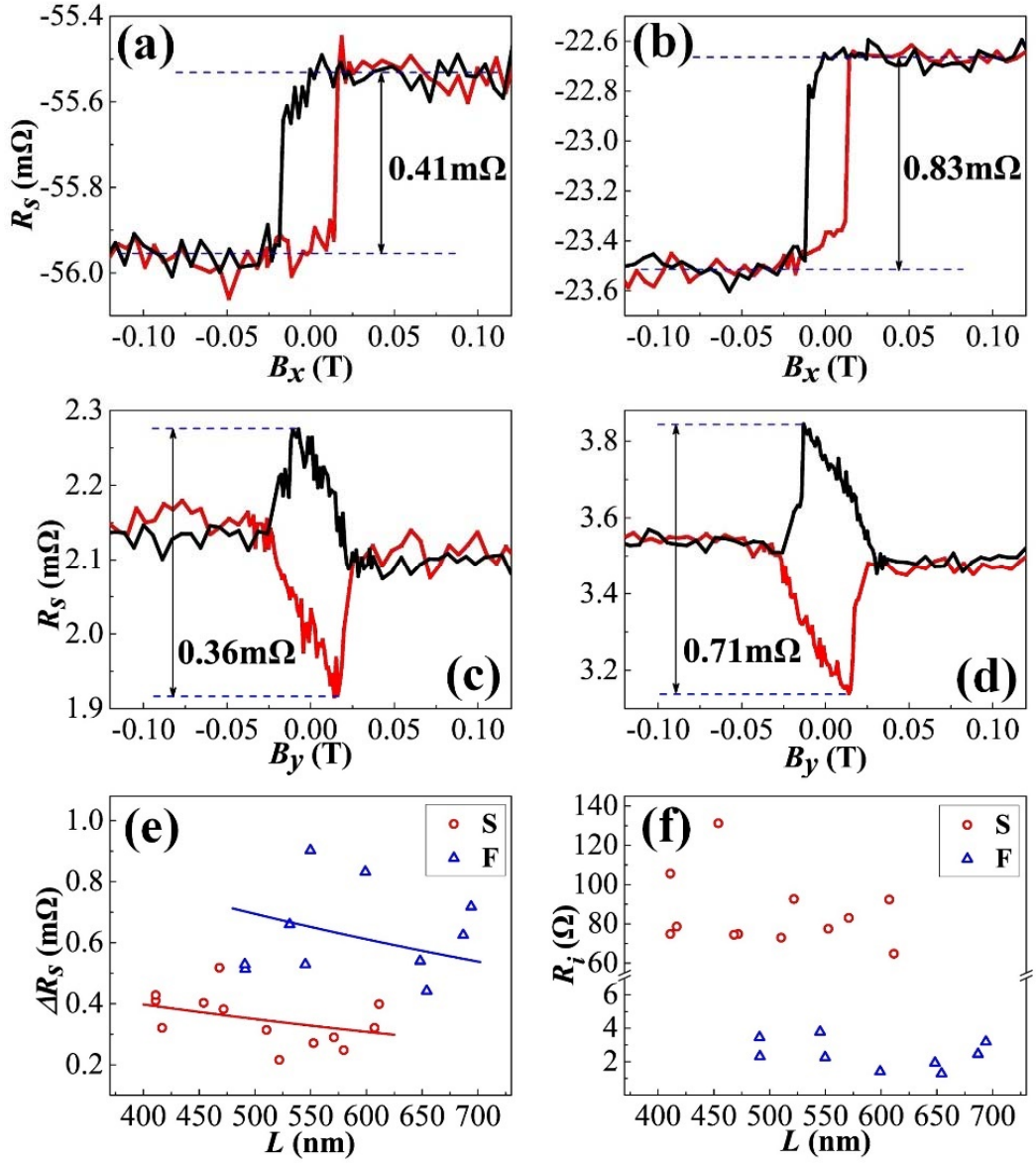

Figure 4.5: Various measurements at 10 K from a sample with 6 nm Pt. ISHE measurements on (a) a small-overlap structure and (b) a full-overlap structure with field along x direction. ISHE measurements on (c) a small-overlap structure and (d) a full-overlap structure with field along y direction. (e) The ΔR_s values from ISHE measurement with field along $\pm x$ direction versus channel length L of the SHE/ISHE structures. (f) The resistance of the Cu/AlO_x/Pt interface for SHE/ISHE devices identified by L. In (e) and (f), S denotes small-overlap and F denotes full-overlap.

Fig. 4.5 (a) and (b) show representative ISHE measurements for a small-overlap structure (ΔR_S = 0.41 mΩ) and a full-overlap structure (ΔR_S = 0.83 mΩ), respectively, with magnetic field along the *x* direction. The ISHE measurements with a magnetic field along *y* direction (parallel to Py injectors) are shown in Fig. 4.5 (c) and (d) for the same two structures as in Fig. 4.5 (a) and (b), respectively. At large ± *B*, spin moments along ± *y* are injected and the ISHE voltage generated in the Pt film is in the *x* direction. Therefore, the R_s value measured across the Pt stripe, which lies in the *y* direction, reaches the same value for large + *B* and - *B*. At intermediate fields, the magnetization of Py rotates in the substrate plane and has a non-zero projection on the *x* axis. Therefore, a variation of R_s is observed across the Pt stripe. However, the ΔR_S values are smaller than those in Fig. 4.5 (a) and (b), because the Py magnetization is never fully aligned along ± *x* direction. This is consistent with our previously published results [3].

The ΔR_S values of all SHE/ISHE structures on this substrate are plotted as a function of the channel length *L* in Fig. 4.5 (e). The average ΔR_S of the full-overlap structures is 0.63 mΩ, which is 1.8 times of the average ΔR_S of 0.35 mΩ for the small-overlap structures. The solid line is a fit assuming an exponential decay of the ΔR_S as a function of *L* with λ_{cu} as the decay length. The resistance values R_i of the Cu/AlO_x/Pt interfaces are shown for SHE/ISHE structures with various channel length *L* in Fig. 4.5 (f). The *L* values are used as a labeling mechanism for various SHE/ISHE structures without implying any necessary correlation between R_i and *L*. The small-overlap structures have a larger average R_i of 85 Ω than that (3 Ω) of the full-overlap structures.

4.3 Quantitative Analysis of SHE/ISHE Signals

In this section, we use simple models to derive a relationship between the magnitude of $\Delta R_s = 2\Delta R_{SHE}$, the spin Hall angle α_H, the spin diffusion length λ_{pt} of Pt, and other measurable quantities in SHE/ISHE structures. This will allow us to obtain the α_H and λ_{pt} from the experimental results. The calculation has been carried out with both SHE and ISHE and the results are consistent. The models yield the same average spin Hall angles for the small-overlap and full-overlap structures, attesting to the effectiveness of the models.

Refer to Fig. 4.3 (a) and (b) for relevant dimensions. In the context of ISHE, a spin current is injected from Py and flows down the Cu channel along the + x direction. Upon reaching the Cu/AlO_x/Pt interface near the end of the Cu channel, a reflected spin current flows toward – x direction and an absorbed spin current flows across the AlO_x into the Pt. The absorbed spin current flows perpendicularly into the Pt film along z direction and gives rise to the ISHE voltage.

From one-dimensional diffusion equation, the spin accumulation in Cu is described as $\delta\mu_{cu}(x) = a_1 exp(-x/\lambda_{cu}) + a_2 exp(x/\lambda_{cu})$ for $0 < x < L$ and $\delta\mu_{cu}(x) = a_1' exp(x/\lambda_{cu})$ for $x < 0$, where $\delta\mu_{cu} = \mu_{cu\uparrow} - \mu_{cu\downarrow}$. The combined electrochemical potential $\mu_{cu\uparrow,\downarrow}$ is defined as $\mu_{cu\uparrow,\downarrow} = -\mu_{ch\uparrow,\downarrow}/e + V$, where $\mu_{ch\uparrow,\downarrow}$ is the chemical potential for spin-up (-down) and V is the electrical voltage. The spin current in the Cu channel is $I_s(x) = -\frac{\sigma_{cu}}{2}\left(\frac{d\delta\mu_{cu}(x)}{dx}\right)A_{cu}$, where σ_{cu} is the Cu conductivity and A_{cu} is the cross-sectional area of the Cu channel. At $x = 0$, boundary conditions are $\delta\mu_{cu}(0^-) = \delta\mu_{cu}(0^+)$ and $I_s(0^+) - I_s(0^-) = PI_e$, where I_e is the charge injection current through the Py/AlO_x/Cu interface and P is the effective injection polarization of the interface. Note that at $x < 0$, the spin current is toward – x direction and therefore carries a negative value. At $x = L$, boundary conditions are

$I_s(L) = I_{sa}$ and $\frac{\delta\mu_{cu}(L)}{2R_i} = I_{sa}$, where I_{sa} is the absorbed spin current into the Pt. The latter equation indicates that the I_{sa} is driven by the spin accumulation difference across the Cu/AlO_x/Pt interface, which has a resistance of R_i. We obtain the absorbed spin current: $I_{sa} = 1/2\,\gamma P I_e exp(-L/\lambda_{cu})$, where

$$\gamma = 2R_{scu}/(R_{scu} + R_i) \tag{4.1}$$

is the spin absorption coefficient and $R_{scu} = \lambda_{cu}/\sigma_{cu}A_{cu} = \rho_{cu}\lambda_{cu}/A_{cu}$ is the spin resistance of the Cu channel. If $R_i = 0$, $\gamma = 2$; if $R_i \gg R_{scu}$, $\gamma = 2R_{scu}/R_i \ll 1$.

The absorbed spin current flows perpendicularly (along z direction) into Pt and the ISHE develops a voltage in the y direction. Consider $z = 0$ at the top surface of the Pt film and $z = t_{pt}$ for the bottom surface of the Pt film. The spin current density absorbed into the Pt top surface is $j_{sa} = I_{sa}/A_j$, where A_j is the area of the Cu/AlO_x/Pt junction. If assuming uniform junction width w_I, $A_j = w_I d$, where d is the overlap between Cu and Pt along the x direction. The spin injection into Pt induces a spin accumulation, which can be described by $\delta\mu_{pt}(z) = u_1 exp\left(-z/\lambda_{pt}\right) + u_2 exp\left(z/\lambda_{pt}\right)$. The spin current density in the z direction is $j_s(z) = -\frac{\sigma_{pt}}{2}\left(\frac{d\delta\mu_{pt}(z)}{dz}\right)$, where $\sigma_{pt} = 1/\rho_{pt}$ is the Pt conductivity. Boundary conditions are $j_s(0) = j_{sa}$ and $j_s\left(t_{pt}\right) = 0$, which states that the spin current near the top surface equal to the absorbed spin current and the spin current near the bottom surface vanishes. Then the coefficients u_1 and u_2 can be solved from the boundary conditions and the $j_s(z)$ is determined. The ISHE induces a charge current $\alpha_H j_s(z)$ in the y direction and therefore an electric field $E_y(z) = \alpha_H \rho_{pt} j_s(z)$. The resulting voltage between two ends of the Pt stripe is $V_{nl} = w_I \overline{E_y(z)} = w_I \frac{1}{t_{pt}} \int_0^{t_{pt}} E_y(z) dz$.

The voltage on the Pt stripe changes sign and becomes $-V_{nl}$ when the injected spins at $x = 0$ from the Py changes sign. Therefore $\Delta R_s = \Delta V_{nl}/I_e = 2V_{nl}/I_e$. In

addition, the shunting effect from two sources will reduce the V_{nl}. The Pt at $x > L + d/2$ is not in contact with the Cu channel, does not receive a spin current on the top surface, and therefore generates no ISHE voltage. As a result, the V_{nl} should be multiplied by a reduction factor d/w_{pt}. Also, the highly conductive Cu channel shunts the ISHE voltage through the low-resistance oxide barrier and the reduction factor is

$$\chi = 4R_i/\left(4R_i + R_{pt}\right) \tag{4.2}$$

where $R_{pt} = \rho_{pt} w_I/\left(w_{pt} t_{pt}\right)$ is the resistance along the y direction of the Pt segment that is shown as green shaded area in Fig. 4.3 (a), (b) and Fig. 4.6 (a). Parallel to R_{pt} is another conduction channel that passes through half of the Cu/AlO_x/Pt junction, the highly conductive Cu, and the other half of the Cu/AlO_x/Pt junction, as shown in Fig. 4.6 (a) and (b). The resistance of this parallel channel is $4R_i$, since each half-junction has the resistance value of $2R_i$ and the Cu resistance (along the y direction) is negligible compared to R_i. The Pt segment can be seen as an electromotive force (ISHE voltage) with an internal resistance R_{pt}. The resistance of $4R_i$ can be considered as the external resistance, and the actually measured voltage should be the terminal voltage on the $4R_i$. The ratio χ between the terminal voltage and the emf voltage is therefore expressed by Eq. 4.2. Summarizing all above, the ISHE signal can be calculated:

$$\Delta R_s = 2\Delta R_{SHE} = \frac{\alpha_H \gamma \chi \lambda_{pt} \rho_{pt} P}{t_{pt} w_{pt}} \left(\frac{exp(t_{pt}/\lambda_{pt}) - 1}{exp(t_{pt}/\lambda_{pt}) + 1}\right) exp(-L/\lambda_{cu}) \tag{4.3}$$

Note that the shape of the lower tip of the Cu channel does not affect the above result. To prove this, we assume a variable width along x direction $w_i(x)$ instead of a constant w_I, and thereby V_{nl} depends on the x as well: $V_{nl}(x) = w_i(x)\overline{E_y(z)} \propto w_i(x)\overline{J_s(z)} \propto w_i(x)\frac{I_{sa}}{A_j}$, where $A_j = \int_{L-d/2}^{L-d/2} w_i(x)dx$ is the area of the Cu/AlO_x/Pt

junction. The measured voltage should be an average over x: $\overline{V_{nl}} \propto \frac{I_{sa}}{A_j} \cdot \frac{1}{d}\int_{L-d/2}^{L+d/2} w_i(x)dx = \frac{I_{sa}}{d}$, which is independent of A_j or a particular form of $w_i(x)$ [3].

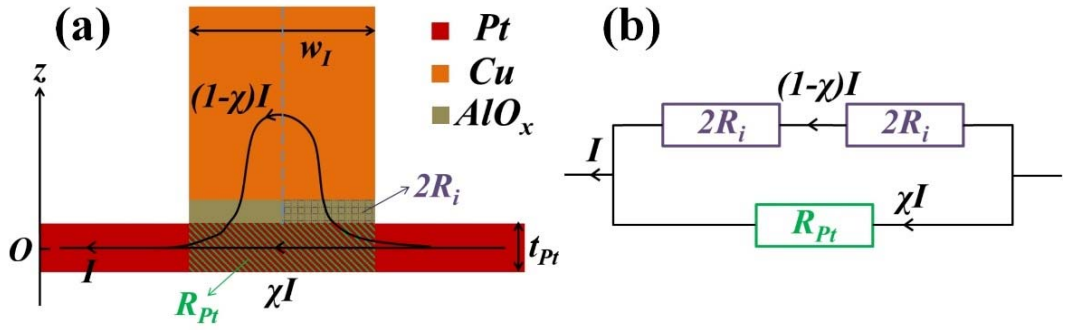

Figure 4.6: (a) The cross-sectional view of Fig. 4.3 (a) or (b) along the green dashed line perpendicular to the Cu channel and the distribution of charge current for SHE measurement. (b) Resistor model for calculating shunting factor χ.

The calculation has also been done in the context of SHE. A charge current is injected through Pt along the y direction, forming a spin current in the z direction owing to SHE and causing spin accumulations on the surface of Pt stripe. The spin accumulation on the top Pt surface drives the spins across the Cu/AlO_x/Pt interface into Cu channel. The spins in Cu is then detected by the Py electrode as the nonlocal spin signal.

In the SHE, the factor χ can be understood in a more straightforward manner, as shown in Fig. 4.6 (a), which is a cross-sectional view of the structures in Fig. 4.3(a) or (b) along the dashed line. When a charge current is sent through the two ends of the Pt stripe, only a fraction (χ) of the current stays in the Pt film, and the rest $(1-\chi)$ of the current is shunted by the Cu. As in Fig. 4.6 (a), the shunted current flows across

right-half of the AlO_x interface (with resistance $2R_i$) into the Cu and then flows across the left-half of the AlO_x interface (with resistance $2R_i$) out of Cu. Therefore, the resistance to the shunted current is $4R_i$, neglecting the resistance of the highly conductive Cu. The resistance to the current in the parallel branch through Pt is R_{pt}. The equivalent circuit model is shown in Fig. 4.6 (b). From current divider rule for parallel resistors, we have obtained the expression of χ in Eq. 4.2.

Due to the SHE, the charge current $j_c' = \chi I_e/(w_{pt}t_{pt})$ which remains in Pt gives rise to a transverse spin current density of $j_s' = \alpha_H j_c' = \frac{\alpha_H \chi I_e}{w_{pt}t_{pt}}$. Refer to the coordinate in Fig. 4.6 (a), where $z = \frac{t_{pt}}{2}$ is the top surface of the Pt film and $z = -\frac{t_{pt}}{2}$ is the bottom surface, the spin accumulation in Pt is described as $\delta\mu_{pt}'(z) = v_1 exp(-z/\lambda_{pt}) + v_2 exp(z/\lambda_{pt})$. Because the spin accumulation along z direction is symmetrical, $\delta\mu_{pt}'(0) = 0$ gives the relation $v_1 = -v_2$. The spin current density in the z direction is $j_s'(z) = -\frac{\sigma_{pt}}{2}\left(\frac{d\delta\mu_{pt}'(z)}{dz}\right)$. At the top and bottom Pt surfaces, the spin current driven by the spin accumulation cancels the spin current driven by the SHE in the z direction, we obtain the boundary condition $j_s'\left(\frac{t_{pt}}{2}\right) = 0$, where the coefficients v_1 and v_2 can be solved to determine $j_s'(z)$. The spin accumulations on the top Pt surface drives spins across Cu/AlO_x/Pt into Cu, and the spin accumulation in Cu at the injection point can be expressed as $\gamma'\delta\mu_{pt}'\left(\frac{t_{pt}}{2}\right)$. Parameter γ' is the spin injection rate from Pt into Cu. The spin accumulation in the Cu channel decays over distance as $\delta\mu_{cu}'(x) = \delta\mu_{cu}'(0)exp(-x/\lambda_{cu})$, where $\delta\mu_{cu}'(0)$ is the spins in Cu at Cu/AlO_x/Pt interface ($x = 0$). The spin current in the Cu channel is then described as $I_s'(x) = -\frac{\sigma_{cu}}{2}\left(\frac{d\delta\mu_{cu}'(x)}{dx}\right)A_{cu}$. The boundary conditions at $x = 0$ are $I_s'(0) = I_{si}$ and $\frac{\delta\mu_{pt}'\left(\frac{t_{pt}}{2}\right) - \delta\mu_{cu}'(0)}{2R_i} = I_{si}$, where I_{si} is the injected spin current into the Cu channel. The second equation in the boundary conditions indicates the interfacial spin current across

the Cu/AlO_x/Pt is driven by the difference of the spin accumulation between two sides of the interface. By solving the boundary condition equations, we obtain $\delta\mu_{cu}(0)$ and find that the spin injection rate γ' equals to spin absorption coefficient γ as shown in Eq. 4.1 in the context of ISHE.

The spin accumulation in Cu channel is then detected by the Py electrode located at $x = L$, and the spin signal is described as $\Delta R_s = \frac{V_{nl}}{I_e} = \frac{P\delta\mu'_{cu}(L)}{I_e}$. It gives the exact same expression as in Eq. 4.3. This is expected from the reciprocal relationship between SHE and ISHE and reassures the validity of Eq. 4.3.

4.4 Determination of $\alpha_H\lambda_{pt}$

The expression of ΔR_s in Eq. 4.3 can be rewritten as:

$$\Delta R_s = 2\Delta R_{SHE} = \frac{\alpha'_H\gamma\chi\rho_{pt}P}{2w_{pt}} exp\left(-\frac{L}{\lambda_{cu}}\right) \tag{4.4}$$

with the definition of an apparent spin Hall angle α'_H:

$$\alpha'_H(t_{pt}) = 2\alpha_H\left(\frac{\lambda_{pt}}{t_{pt}}\right)\left(\frac{exp(t_{pt}/\lambda_{pt})-1}{exp(t_{pt}/\lambda_{pt})+1}\right) \tag{4.5}$$

Note that α'_H is a mere definition for convenience and its value monotonically decays as a function of the Pt thickness t_{pt}. But α_H is the real Pt spin Hall angle and does not depend on the t_{pt}. In the limit of thin Pt films (*i.e.* $t_{pt} \ll \lambda_{pt}$), the apparent spin Hall angle is a constant and shares the same value with the spin Hall angle: $\alpha'_H = \alpha_H$. Therefore, in this limit, the Pt spin Hall angle α_H can be directly calculated from the measured signal ΔR_s by using Eq. 4.4. As t_{pt} increases above the thin limit, the α'_H monotonically but gradually decreases, reaching $\alpha'_H = 0.76\alpha_H$ when $t_{pt} = 2\lambda_{pt}$. In the limit of thick Pt films (*i.e.* $t_{pt} \gg \lambda_{pt}$), $\alpha'_H(t_{pt}) = 2\alpha_H\left(\frac{\lambda_{pt}}{t_{pt}}\right)$ and the apparent spin Hall angle α'_H is inversely proportional to the Pt film thickness. Because only a thickness of λ_{pt} near the top Pt surface contributes to the SHE signal. As a result, in

this thick limit, the α_H' decays more rapidly as a function of t_{pt}. The magnitude of ΔR_s essentially follows a similar dependence on t_{pt}, assuming that other physical parameters are fixed. For an unknown relationship between λ_{pt} and t_{pt}, one can first use Eq. 4.4 to calculate the apparent spin Hall angle α_H' from experimental values of ΔR_s for samples with various t_{pt} values. Then a fit of the α_H' versus t_{pt} dependence by Eq. 4.5 will generate the Pt spin Hall angle α_H and the Pt spin diffusion length λ_{pt}.

Table 4.1: The ΔR_s of ISHE, channel distance L, interface resistance R_i and calculated shunting factor χ, spin absorption rate γ, and apparent spin Hall angle α_H' for selected small-overlap (S-4, 6, 12) and full-overlap SHE/ISHE structures (F-1, 4, 12) for a sample with t_{pt} = 6 nm.

Device	ΔR_s **mΩ**	L **nm**	R_i **Ω**	χ	γ	α_H'
S-4	0.38	471.9	74.8	0.80	0.033	0.040
S-6	0.52	468.2	74.5	0.79	0.033	0.052
S-12	0.27	552.6	77.5	0.82	0.032	0.032
F-1	0.51	491.3	2.3	0.077	0.64	0.030
F-4	0.90	549.7	2.2	0.074	0.66	0.058
F-12	0.54	648.3	1.9	0.066	0.71	0.040

We apply this method to our experimental data. Table 4.1 lists values of ΔR_s, R_i, γ, χ, and α_H' for several SHE/ISHE structures with 6nm Pt film. The three small overlap structures (S-4, S-6, and S-12) has larger χ but smaller γ compared to the full overlap structures (F-1, F-4, and F-12). The larger junction resistance R_i of the small-overlap reduces the shunting effect and therefore allows a higher fraction (χ) of current to remain in Pt (in the context of SHE). The spin current across the interface is

also reduced owing to the larger R_i and therefore γ is reduced. The two important processes, the shunting of charge current and the transport of interfacial spin current, are both effectively quantified by the junction resistance R_i through Eq. 4.1 and 4.2.

The values of the apparent spin Hall angle α_H' calculated from Eq. 4.4 from small-overlap structures with various L values are plotted in Fig. 4.7 (a) and those from the full-overlap are plotted in Fig. 4.7 (b). All values come from SHE/ISHE structures with 6 nm Pt on the same substrate. Interestingly, the average α_H' values are exactly the same: α_H' = (0.043 ± 0.011) for small-overlap and α_H' = (0.043 ± 0.013) for full-overlap, despite the difference of average R_i by a factor of 28 and the difference of average ΔR_s by a factor of 1.8. This attests to the validity and consistency of this method.

Using this method, the α_H' values from samples with different Pt thickness are determined and plotted as a function of the Pt thickness, as shown in Fig. 4.7 (c). A total number of 58 SHE/ISHE structures with 4 different t_{pt} values from 6 substrates are included. As t_{pt} increases from 4 nm to 12 nm, a drastic decay of α_H' is observed and indicates that $t_{pt} > \lambda_{pt}$. Because when $t_{pt} < \lambda_{pt}$, α_H' should remain nearly a constant and be approximately equal to α_H according to Eq. 4.5. When a fit of the α_H' versus t_{pt} by Eq. 4.5 is conducted with α_H and λ_{pt} as free parameters, the best fit generates short spin diffusion length λ_{pt} = 0.25 nm and large spin Hall angle α_H = 0.53. The fitted curve is shown as the green line in Fig 4.7 (c). The product of the two values is $\alpha_H\lambda_{pt}$ = 0.132 nm. Note that the fitting is weighted by the number of SHE/ISHE structures investigated at each thickness. This number is indicated next to each data point in Fig. 4.7 (c).

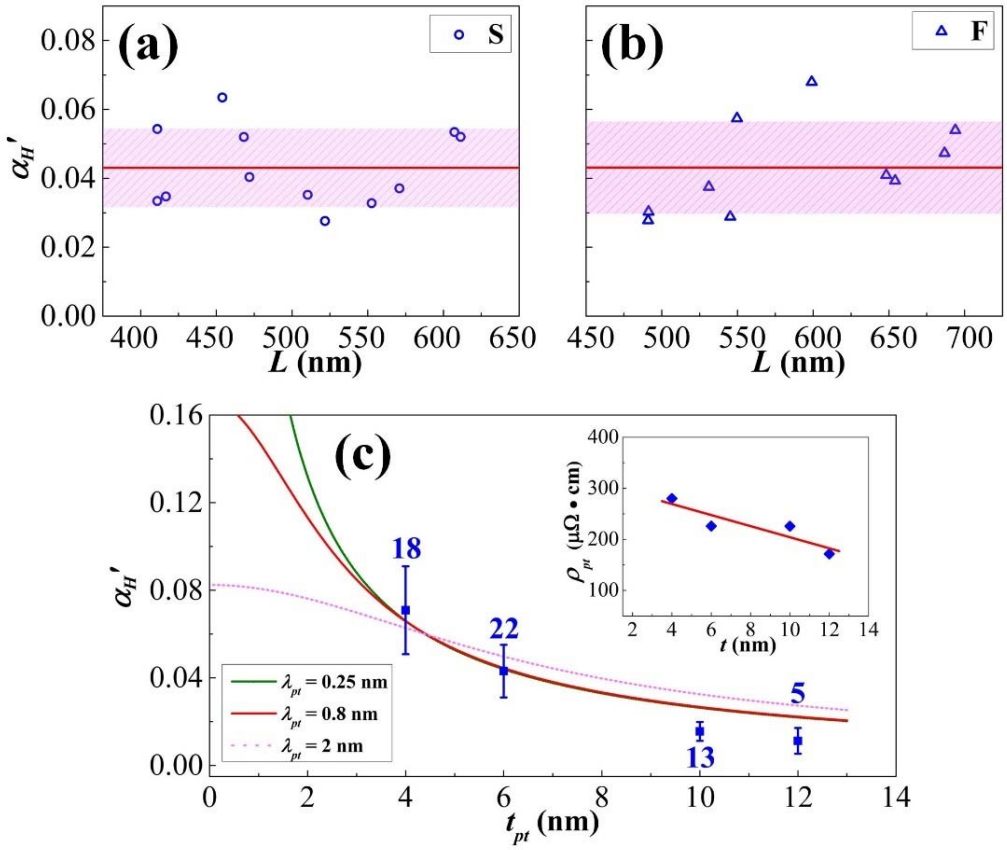

Figure 4.7: Calculated apparent spin Hall angle α_H' for (a) the small-overlap structures and (b) the full-overlap structures from the sample with 6 nm Pt at 10K. The red lines indicate average values in each case and the shaded areas indicate the standard deviation. (c) The value of α_H' as a function of Pt thickness from 58 SHE/ISHE devices. The number next to each data point indicates the number of SHE/ISHE structures measured for that thickness. The solid and dashed lines are fits with various λ_{pt}. The fitting is weighted by the number of structures at each thickness. The inset of (c) shows the Pt resistivity as a function of Pt thickness.

We also used other fixed values of λ_{pt} within the range of 0.25 nm ≤ λ_{pt} ≤ 0.8 nm and left α_H as the single fitting parameter. Interestingly we could obtain equally satisfactory fits for any λ_{pt} in that range. Though the fitted α_H decreases as the

assumed λ_{pt} increases, the product of the two always remains the same. The red line in Fig. 4.7 (c) corresponds to λ_{pt} = 0.8 nm and α_H = 0.167, yielding $\alpha_H\lambda_{pt}$ = 0.133 nm. Within the range of the experimental data (4 nm ≤ t_{pt} ≤ 12 nm), this curve is almost identical as the green curve (λ_{pt} = 0.25 nm), and both scale with $1/t_{pt}$. The difference between two curves lies in the region t_{pt} < 4.0 nm, where no experimental data is present.

The experimental α_H' values for 10 nm and 12 nm are below the fitted curves, because the decay of α_H' as a function of t_{pt} is faster than the $1/t_{pt}$ trend given by the model. For λ_{pt} > 0.8 nm, the calculated curves show even slower decaying trend, and obviously cannot describe the experimental data well. Fig. 4.7 (c) shows a fitting curve for λ_{pt}= 2.0 nm and its correlation with experimental data is clearly worse than the curve with λ_{pt} < 0.8 nm. Therefore, we can safely conclude that the upper limit of the λ_{pt} is 0.8 nm. The present set of experimental data cannot conclude the precise value of λ_{pt}, but the fitting with various λ_{pt} values between 0.25 nm and 0.8 nm gives a consistent product of $\alpha_H\lambda_{pt}$ = (0.133 ± 0.067) nm.

The short λ_{pt} is consistent with the high resistivity of the mesoscopic Pt film and with the works by Liu *et al.* [13], Zhang *et al.* [33], and Nguyen *et al.* [22]. The ρ_{pt} as a function of film thickness is shown in the inset of Fig. 4.7 (c), and shows gradual decrease as the t_{pt} is increased. From Eq. 4.4 and 4.5, it is obvious that the SHE/ISHE signal ΔR_{SHE} is proportional to $\alpha_H\rho_{pt}$ or equivalently $\sigma_H\rho_{pt}^2$. An underestimated ρ_{pt} would lead to an overestimated spin Hall angle α_H or spin Hall conductivity σ_H. Therefore, the accurate determination of the in-situ resistivity is an essential component of quantifying the SHE/ISHE. Using the average ρ_{pt} = 225 μΩ•cm from the inset of Fig. 4.7 (c) and 0.25 nm < λ_{pt} < 0.8 nm, we have 0.56 × 10^{-15}

$\Omega\cdot m^2 < \rho_{pt}\lambda_{pt} < 1.8 \times 10^{-15}\ \Omega\cdot m^2$. Using $\alpha_H\lambda_{pt} = \sigma_H\rho_{pt}\lambda_{pt} = 0.133$ nm, we estimate the spin Hall conductivity to be $0.74 \times 10^5\ \Omega^{-1}m^{-1} < \sigma_H < 2.4 \times 10^5\ \Omega^{-1}m^{-1}$. As a comparison, Nguyen *et al*. [22] obtained $\rho_{pt}\lambda_{pt} = (0.77 \pm 0.08) \times 10^{-15}\ \Omega\cdot m^2$ and $\sigma_H = (5.9 \pm 0.2) \times 10^5\ \Omega^{-1}m^{-1}$ from spin Hall torque measurements.

The electron mean free path in the Pt films can be estimated to be 0.21 nm from the average ρ_{pt} using the Drude model. This value is lower than the range of spin diffusion length (0.25 nm < λ_{pt} < 0.8 nm), as expected from the Elliott-Yafet spin relaxation mechanism. However, the short λ_{pt} (< 0.8 nm) suggests that the effect is more sensitive to the surface region of the film. As a point of reference, the lattice constant of Pt is 0.39 nm.

Since we are confident that the experimental results are in the limit of $t_{pt} >> \lambda_{pt}$, we obtain $\alpha_H\lambda_{pt} = \alpha'_H(t_{pt}/2)$ from the limiting form of Eq. 4.5. Therefore, the $\alpha_H\lambda_{pt}$ can be calculated for each SHE/ISHE structure from the α'_H. The results obtained from all 58 devices are summarized in Fig. 4.8 (a), where the value is plotted against the *L* value of each structure. Again, *L* is used as a labeling mechanism without suggesting any necessary dependence of $\alpha_H\lambda_{pt}$ on *L*. Different Pt thicknesses t_{pt} are represented by different symbols. Though the average of all 58 structures is $\alpha_H\lambda_{pt}$ = (0.12 ± 0.05) nm, the data are scattered over a broad range. A substantial number (15 out of 58) of structures show 0.15 nm < $\alpha_H\lambda_{pt}$ < 0.21 nm. The highest value is $\alpha_H\lambda_{pt}$ = 0.21 nm for a structure with 4 nm Pt.

It is noticeable in Fig. 4.8 (a) that the 4 nm and 6 nm Pt films tend to show higher $\alpha_H\lambda_{pt}$ than the 10 nm and 12 nm Pt films. Therefore, we plot the average $\alpha_H\lambda_{pt}$ of each Pt thickness as a function of t_{pt} in Fig. 4.8 (b). We have obtained $\alpha_H\lambda_{pt}$ = (0.142 ± 0.040) nm for 4 nm Pt, $\alpha_H\lambda_{pt}$ = (0.129 ± 0.036) for 6 nm Pt, $\alpha_H\lambda_{pt}$

= (0.078 ± 0.022) for 10 nm Pt, and $\alpha_H\lambda_{pt}$ = (0.067 ± 0.035) for 12 nm Pt. There is a gradually decreasing trend of $\alpha_H\lambda_{pt}$ as Pt thickness t_{pt} increases. The dash-dot line is a guidance of eyes. As stated earlier, the quantity $\alpha_H\lambda_{pt}$ is equivalent to $\sigma_H\rho_{pt}\lambda_{pt}$, which is supposed to be a constant if the spin Hall effect is intrinsic (constant σ_H) and if the spin relaxation in Pt can be described by Elliott-Yafet model (constant $\rho_{pt}\lambda_{pt}$). Therefore, the decreasing trend in Fig. 4.8 (b) suggests that either the SHE is not entirely intrinsic or the assumption of constant $\rho_{pt}\lambda_{pt}$ is oversimplified. It is unclear at this point which is the primary cause.

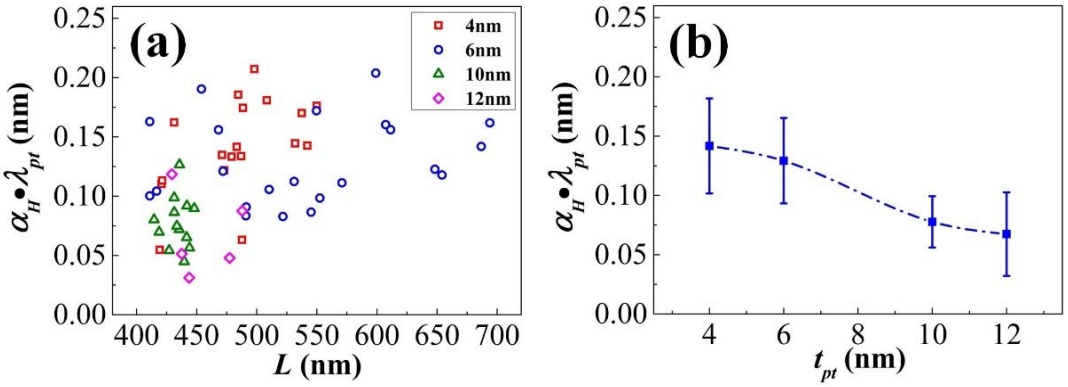

Figure 4.8: (a) Calculated $\alpha_H\lambda_{pt}$ for each SHE/ISHE structure is plotted against the channel distance L of the structure. Different symbols represent various thicknesses. (b) The average experimental value of $\alpha_H\lambda_{pt}$ is plotted as a function of t_{pt}. The dash-dot line is a guidance of eyes.

4.5 Further Discussion

The results (values of σ_H and $\rho_{pt}\lambda_{pt}$) by Nguyen *et al*. [22] lead to a large value of $\sigma_H\rho_{pt}\lambda_{pt}$ = 0.45 nm. Our result of average $\sigma_H\rho_{pt}\lambda_{pt}$ = (0.142 ± 0.040) nm for 4 nm Pt is lower by more than a factor of 3. However, our highest $\sigma_H\rho_{pt}\lambda_{pt}$ value

from an individual SHE/ISHE structure is 0.21 nm, roughly half of the value by Nguyen *et al*. By using spin pumping method, Feng *et al*. [34] reported α_H = 0.012 and λ_{pt} = 8.3 nm, yielding $\alpha_H\lambda_{pt}$ = 0.10 nm. The same $\alpha_H\lambda_{pt}$ = 0.10 nm can be inferred from the spin pumping measurements by Zhang *et al.* [33], but the values of α_H = 0.086 and λ_{pt} = 1.2 nm are different. Qu *et al*. [35] used spin Seebeck effects and ISHE, and reported α_H = 0.013 and λ_{pt} = 2.5 nm and thereby $\alpha_H\lambda_{pt}$ = 0.03 nm.

A comparison can also be made with nonlocal measurements on mesoscopic Pt films by other groups. Morota *et al*. [20] reported λ_{pt} = 11 nm and α_H = 0.021, yielding $\alpha_H\lambda_{pt}$ = 0.23 nm. Though this value is in reasonable agreement with ours, the λ_{pt} is much higher and the $\alpha_H$is much lower than our estimation. In addition, it is noteworthy to point out that the reported resistivity for their mesoscopic Pt films is ρ_{pt} = 12.3 μΩ•cm, which is much lower than the values measured in-situ from our mesoscopic Pt films. Isasa *et al*. [36] reported λ_{pt} = 3.4 nm and α_H = 0.009, yielding $\alpha_H\lambda_{pt}$ = 0.03 nm, which is much smaller than our value. Their reported resistivity value is ρ_{pt} = 25 μΩ•cm.

The broad distribution of the results in the literature is not completely surprising. Our own results in Fig. 4.8 (a) scatter broadly between 0.03 nm and 0.21 nm. The microstructure of the Pt films likely imposes strong influences on the SHE. The salient difference between our experiments and others is that our Pt films are truly mesoscopic with high resistivity and therefore a short λ_{pt} can be confidently concluded. The microstructures of the mesoscopic films may vary and induce variations of σ_H, ρ_{pt}, and λ_{pt} between individual structures. In contrast, effects measured from larger films may represent average behavior over a large area. Overall, the $\sigma_H\rho_{pt}\lambda_{pt}$ values we obtained are still quite substantial in magnitudes.

4.6 Conclusions

In conclusion, we use nonlocal structures to demonstrate enhanced spin Hall effects and inverse spin Hall effects in mesoscopic Pt films. Essential physical quantities are all determined in-situ on the same substrate and provide an accurate representation of the structures. The resistivity of the mesoscopic Pt films is substantially higher than extended Pt films and can be beneficial for the energy efficiency of the spin Hall effects. The spin absorption into Pt and the current shunting by Cu are treated effectively using simple models with resistors and spin resistors. By consistent analysis of the samples with various Pt thicknesses, we confidently set an upper limit of 0.8 nm for the Pt spin diffusion length.

The product of the spin Hall angle and the spin diffusion length of Pt, $\alpha_H \lambda_{pt}$, or equivalently the product of the spin Hall conductivity, electrical resistivity, and the spin diffusion length, $\sigma_H \rho_{pt} \lambda_{pt}$, is used as a figure of merit for the spin Hall efficiency in Pt. We have determined an average value of $\alpha_H \lambda_{pt} = (0.142 \pm 0.040)$ nm for 4 nm Pt at 10K. A gradual decrease of the average $\alpha_H \lambda_{pt}$ at higher Pt thickness is observed. Broad distribution of individual $\alpha_H \lambda_{pt}$ values from 0.03 nm to 0.21 nm is present and indicates possible variations of microstructures. The substantial values of $\alpha_H \lambda_{pt}$ suggest efficient generation of spin current via the spin Hall effects.

REFERENCES

[1] S. O. Valenzuela and M. Tinkham, Nature **442** (7099), 176 (2006).

[2] T. Kimura, Y. Otani, T. Sato, S. Takahashi and S. Maekawa, Physical Review Letters **98** (15), 156601 (2007).

[3] S. H. Chen, C. Qin and Y. Ji, Applied Physics Letters **105** (8), 082402 (2014).

[4] J. E. Hirsch, Physical Review Letters **83** (9), 1834 (1999).

[5] S. F. Zhang, Physical Review Letters **85** (2), 393 (2000).

[6] Y. K. Kato, R. C. Myers, A. C. Gossard and D. D. Awschalom, Science **306** (5703), 1910 (2004).

[7] A. Hoffmann, IEEE Transactions on Magnetics **49** (10), 5172 (2013).

[8] E. Saitoh, M. Ueda, H. Miyajima and G. Tatara, Applied Physics Letters **88** (18), 182509 (2006).

[9] O. Mosendz, J. E. Pearson, F. Y. Fradin, G. E. W. Bauer, S. D. Bader and A. Hoffmann, Physical Review Letters **104** (4), 046601 (2010).

[10] K. Ando, S. Takahashi, K. Harii, K. Sasage, J. Ieda, S. Maekawa and E. Saitoh, Physical Review Letters **101** (3), 036601 (2008).

[11] L. Q. Liu, T. Moriyama, D. C. Ralph and R. A. Buhrman, Physical Review Letters **106** (3), 036601 (2011).

[12] L. Q. Liu, C. F. Pai, Y. Li, H. W. Tseng, D. C. Ralph and R. A. Buhrman, Science **336** (6081), 555 (2012).

[13] L. Q. Liu, O. J. Lee, T. J. Gudmundsen, D. C. Ralph and R. A. Buhrman, Physical Review Letters **109** (9), 096602 (2012).

[14] M. Miron, G. Gaudin, S. Auffret, B. Rodmacq, A. Schuhl, S. Pizzini, J. Vogel and P. Gambardella, Nature Materials **9** (3), 230 (2010).

[15] D. Qu, S. Y. Huang, J. Hu, R. Q. Wu and C. L. Chien, Physical Review Letters **110** (6), 067206 (2013).

[16] G. Mihajlovic, J. E. Pearson, M. A. Garcia, S. D. Bader and A. Hoffmann, Physical Review Letters **103** (16) (2009).

[17] M. Johnson and R. H. Silsbee, Physical Review Letters **55** (17), 1790 (1985).

[18] F. J. Jedema, A. T. Filip and B. J. van Wees, Nature **410** (6826), 345 (2001).

[19] Y. Niimi, M. Morota, D. H. Wei, C. Deranlot, M. Basletic, A. Hamzic, A. Fert and Y. Otani, Physical Review Letters **106** (12), 126601 (2011).

[20] M. Morota, Y. Niimi, K. Ohnishi, D. H. Wei, T. Tanaka, H. Kontani, T. Kimura and Y. Otani, Physical Review B **83** (17), 174405 (2011).

[21] L. Q. Liu, R. A. Buhrman and D. C. Ralph, arXiv:1111.3702 (2011).

[22] M. H. Nguyen, D. C. Ralph and R. A. Buhrman, Physical Review Letters **116** (12), 126601 (2016).

[23] F. J. Jedema, H. B. Heersche, A. T. Filip, J. J. A. Baselmans and B. J. van Wees, Nature **416** (6882), 713 (2002).

[24] T. Kimura, J. Hamrle, Y. Otani, K. Tsukagoshi and Y. Aoyagi, Applied Physics Letters **85** (16), 3501 (2004).

[25] S. O. Valenzuela and M. Tinkham, Appl Phys Lett **85**, 5914 (2004).

[26] Y. Ji, A. Hoffmann, J. S. Jiang and S. D. Bader, Applied Physics Letters **85** (25), 6218 (2004).

[27] Y. Ji, A. Hoffmann, J. E. Pearson and S. D. Bader, Applied Physics Letters **88** (5), 052509 (2006).

[28] X. J. Wang, H. Zou, L. E. Ocola and Y. Ji, Applied Physics Letters **95**, 022519 (2009).

[29] H. Zou, X. J. Wang and Y. Ji, Journal of Vacuum Science and Technology B **28**, 1314 (2010).

[30] M. Johnson, Physical Review Letters **70** (14), 2142 (1993).

[31] Y. J. Cai, Y. M. Luo, C. Qin, S. H. Chen, Y. Z. Wu and Y. Ji, Journal of Magnetism and Magnetic Materials **405**, 145 (2016).

[32] Y. J. Cai, Y. M. Luo, C. Zhou, C. Qin, S. H. Chen, Y. Z. Wu and Y. Ji, Journal of Physics D: Applied Physics **49**, 185003 (2016).

[33] W. Zhang, V. Vlaminck, J. E. Pearson, R. Divan, S. D. Bader and A. Hoffmann, Applied Physics Letters **103** (24), 242414 (2013).

[34] Z. Feng, J. Hu, L. Sun, B. You, D. Wu, J. Du, W. Zhang, A. Hu, Y. Yang, D. M. Tang, B. S. Zhang and H. F. Ding, Physical Review B **85** (21), 214423 (2012).

[35] D. Qu, S. Y. Huang, B. F. Miao, S. X. Huang and C. L. Chien, Physical Review B **89** (14), 140407 (2014).

[36] M. Isasa, E. Villamor, L. E. Hueso, M. Gradhand and F. Casanova, Physical Review B **92** (1), 019905 (2015).

Chapter 5

NONLOCAL ELECTRICAL DETECTION OF SPIN ACCUMULATION GENERATED BY ANOMALOUS HALL EFFECTS IN MESOSCOPIC $NI_{81}FE_{19}$ FILMS

5.1 Introduction

A pure spin current, which is a flow of spin angular momenta without a net charge current, provides important functionalities for spintronics. Recently, spin Hall effect (SHE) and inverse spin Hall effects (ISHE) have been explored extensively for the conversion between charge current and pure spin current [1-13]. SHE converts longitudinal charge current into transverse spin current. The reciprocal process, inverse spin Hall effect (ISHE), converts spin current into charge current. The SHE/ISHE originates from the strong spin-orbit coupling and was initially studied in heavy nonmagnetic metals such as Pt [6-13]. Later work shows that ISHE also exists in ferromagnetic metal such as $Ni_{81}Fe_{19}$ alloy (permalloy or Py) [14-16], which contains lighter elements than Pt. It is an intriguing prospect, because Py is less expensive than Pt and is a commonly used material in spintronics. This also implies that a transverse spin current would coexist with the transverse charge current produced by the anomalous Hall Effect (AHE), which is the reciprocal of the ISHE in a ferromagnet. A direct measurement of spin current or spin accumulation from the AHE is important to spintronics, because the interplay between the spin current from AHE and the anisotropic magnetoresistance in a ferromagnetic metal is predicted to lead to versatile spin transfer switching [17]. The spin-orbit effects that give rise to

AHE can also induce additional torques in the spin dynamics driven by short magnetic pulses [18].

However, the ferromagnetic nature of Py complicates experimental efforts of probing the spin current that accompanies AHE. Previous relevant work was conducted in the context of ISHE and has used bilayers of Py and ferromagnetic insulator yttrium iron garnet (YIG). A pure spin current from YIG is produced by a temperature gradient via spin Seebeck effect [14, 16] or by microwave excitation via spin pumping [15]. Because of the ISHE, a charge voltage is generated as the pure spin current propagates through Py. The choice of ferromagnetic insulator avoids entanglements of the magneto-resistive effects from otherwise two ferromagnetic metals. However, direct detection of spin accumulation or spin current induced by AHE in a ferromagnet is still lacking.

In this chapter, a nonlocal method is used to directly measure the spin current generated from mesoscopic Py films by AHE. In the same structure, The ISHE in Py is generated and detected *electrically*, complementing previously used spin-Seebeck and spin-pumping methods. With the alternating current (AC) modulation method, the AHE/ISHE signals are extracted from the linear response of the nonlocal voltage difference between two polarities of large magnetic fields. Therefore, the signals are well separated from anomalous Nernst effects, anisotropic magnetoresistance, or regular nonlocal spin signals.

The strength of the SHE/ISHE is often described by a spin Hall angle $\alpha_H = \sigma_H/\sigma = \sigma_H\rho$, where σ_H is the spin Hall conductivity, and σ and ρ are the electrical conductivity and resistivity, respectively. Equally important is the spin diffusion length λ of the SHE/ISHE material. For a thin film that is substantially thicker than λ,

the SHE/ISHE can be enhanced by either increasing α_H or increasing λ. Overestimating one leads to underestimating the other. Furthermore, the spin diffusion length is unlikely to be a material constant, because it varies with the dimension and the resistivity of the material. In this work, we use the product of spin Hall angle and the spin diffusion length $\alpha_H\lambda$, or equvalently $\sigma_H\rho\lambda$, as a figure of merit to quantify the AHE/ISHE in Py.

Accurate quantitative analysis hinges on the accurate determination of all relevant physical quantities, as well as proper treatment of statistical variations between devices. To this end, several (6 - 8) nonlocal AHE/ISHE structures are fabricated on each sample substrate to account for the statistical variations between structures. Supplementary structures (~ 20) are fabricated on the same substrate to provide accurate measurements of the *in-situ* values of Py and Cu resistivity ρ_{Py} and ρ_{Cu}, spin diffusion length λ_{Cu} of Cu, and spin polarizations P and resistance R_i of Py/Cu interfaces. The resistivity of mesoscopic Py films is substantially higher than that of extended films, but decreases as the film thickness increases. By exploring different Py thicknesses, λ_{Py} is found to be $\leq$ 1.0 nm. The value of $\sigma_H\rho_{Py}\lambda_{Py}$ is independent of thickness and resistivity, and comparable to the $\sigma_H\rho_{Pt}\lambda_{Pt}$ obtained previously for mesoscopic Pt films.

5.2 Sample Preparation

The nonlocal AHE/ISHE structures along with two types of supplementary structures are fabricated simultaneously on a single substrate by using shadow mask techniques [19]. Two-layer e-beam resists, PMMA (polymethyl methacrylate) on the top and PMGI (polydimethylglutarimide) at the bottom, are coated on the silicon substrate covered with 200 nm Si_3N_4. Mesoscopic suspended shadow masks are

formed in the resist layers after electron beam (e-beam) lithography, because large undercut develops in the PMGI layer. The shadow mask for the AHE/ISHE structures is illustrated in Fig. 5.1 (a). On the same substrate, additional shadow masks are formed for supplementary structures, which are the nonlocal spin valves (NLSV) [20-25] and the Py resistivity measurement structures.

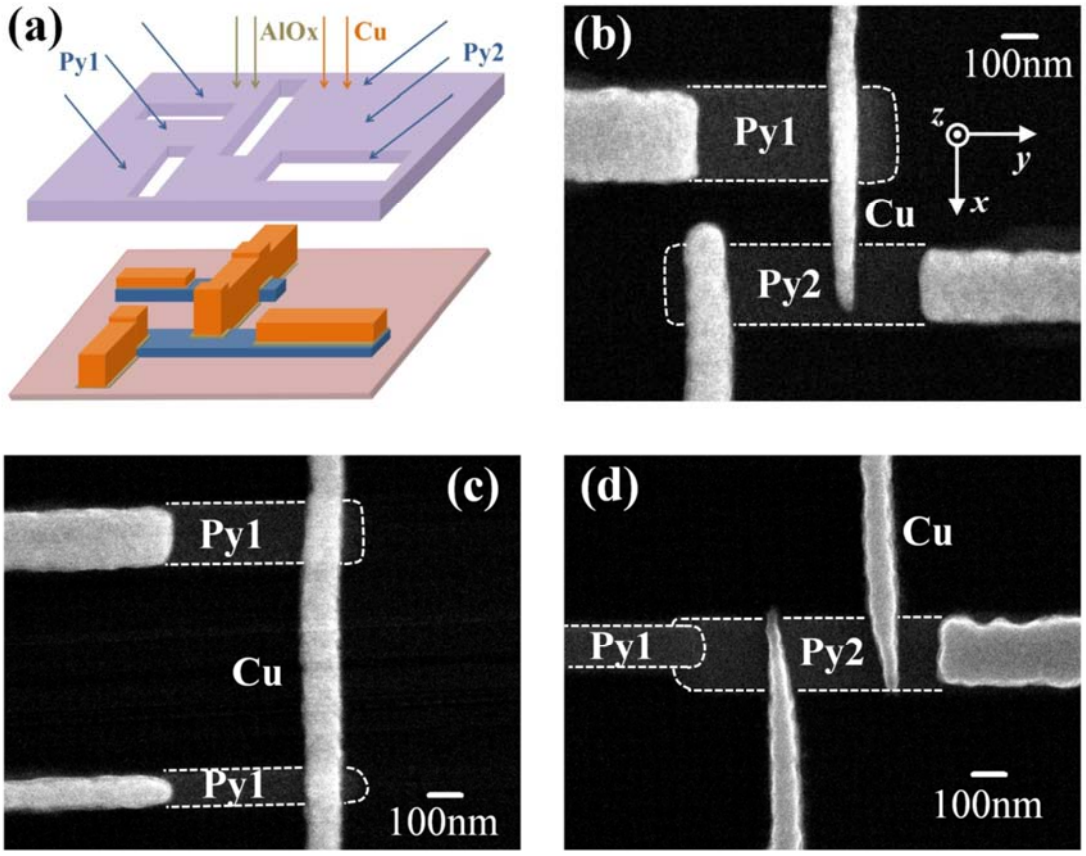

Figure 5.1: (a) Angle evaporation through a mesoscopic suspended shadow mask designed for the AHE/ISHE structures. SEM images for (b) an AHE/ISHE structure, (c) a NLSV and (d) a Py resistivity measurement structure. All structures are fabricated on the same substrate.

Deposition of various materials through the shadow masks is carried out from different angles to form the structures without breaking vacuum. First, Py is evaporated from opposite oblique angles to form two Py pads, designated as Py1 and Py2, as shown in Fig. 5.1 (a) - (d). Subsequently 3 nm AlO_x and 110 nm Cu are deposited along the substrate normal direction. Therefore, all interfaces and materials are formed in high vacuum to ensure efficient spin transport. The scanning electron microscope (SEM) images of finished AHE/ISHE structures, NLSVs, and Py resistivity measurement structures are shown in Fig. 5.1 (b), (c), and (d), respectively. More details of shadow evaporation method can be found elsewhere [26-29].

For the AHE/ISHE structure in Fig. 5.1 (b), the Py1 is the spin injector for ISHE measurement or the spin detector for the AHE measurement, and the thickness remains 12 nm for all samples. The Py2 electrode is the anomalous/spin Hall material in which the AHE or ISHE is generated, and thicknesses of 4 nm, 8 nm, and 12 nm are used on different sample substrates. The Cu channel is used to transport a pure spin current between Py1 and Py2. The widths for Py1, Py2, and Cu are ~250 nm, ~ 230 nm, and ~ 80 nm, respectively.

The NLSV, shown in Fig. 5.1 (c), consists of two Py1 electrodes (an injector and a detector) and a Cu channel, and is used to determine the spin polarization P at the Py1/AlO_x/Cu interfaces and the spin diffusion length $\lambda_{Cu}$and resistivity ρ_{Cu} of Cu channel. The Py resistivity measurement structure, shown in Fig. 5.1 (d), is a mesoscopic Py2 stripe with four electrical probes. It is used to determine the resistivity ρ_{Py} of the mesoscopic Py2 film. The P, λ_{Cu}, ρ_{Cu}, and ρ_{Py} determined from the supplementary structures are the same as those in the AHE/ISHE structures, because

all structures undergo identical fabrication procedures. The lateral dimensions of all structures are characterized by SEM for quantitative analysis.

The 3 nm AlO_x layers in all structures are directly evaporated from AlO_x pellets by electron beam, and the typical resistance for a 100 nm × 100 nm junction is between 5 and 20 Ω. Therefore, it is not a uniform tunnel barrier, which should have much higher resistance. However, it has been demonstrated that the low-resistance AlO_x interfaces are more effective than transparent ohmic interfaces in preventing absorption of spin current into the magnetic electrodes of the NLSV [27, 30-32]. Therefore, a higher spin accumulation can be maintained in the Cu channel, leading to large spin signals in NLSV. In addition, an electric current that flows through the Py2 electrode and generates AHE can be undesirably shunted by the conductive Cu, but the finite resistance of $Cu/AlO_x/Py2$ interfaces reduces this shunting effect.

5.3 Measurements

Measurements are performed in a pulse-tube variable temperature cryostat at 5 K and 295 K. We describe the measurements using the 5 K results for the sample with 8 nm Py2. Fig. 5.2 (a) and (b) illustrate the ISHE and AHE measurements, respectively. The measurement configurations are shown in the insets. For ISHE, an injection current is directed between the Py1 (I+) and the upper end of the Cu channel (I-). The nonlocal voltage is detected between the two ends of the Py2 stripe, with V+ on the left and V- on the right. For AHE, the current flows through the Py2 stripe, with I+ on the right and I- on the left. The nonlocal voltage is measured between the Py1 (V+) and the upper end of Cu channel (V-). An alternating current (*a.c.*) of I_e = 0.2 mA with a frequency of 346.5 Hz is applied, and the nonlocal *a.c.* voltage V_{nl} is

detected by lock-in method. The nonlocal resistance, $R_s = V_{nl}/I_e$, is recorded as a function of the magnetic field B_x, which is applied parallel to the Cu channel.

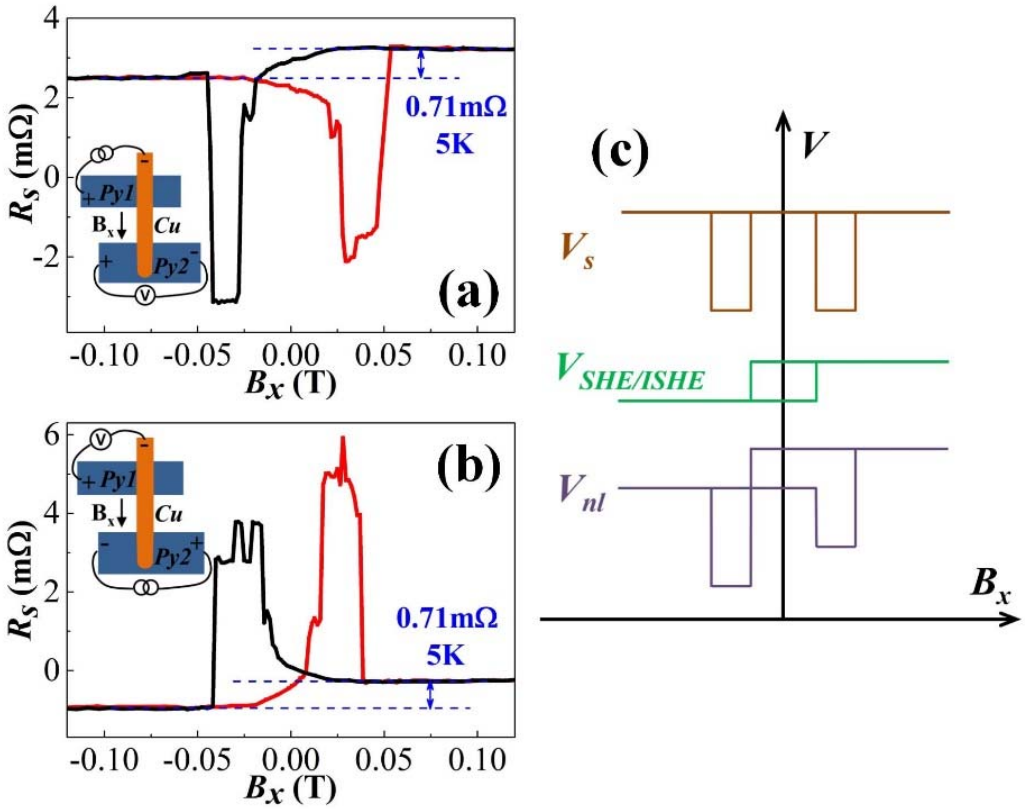

Figure 5.2: The R_s versus B_x curves at 5 K of (a) an ISHE measurement and (b) an AHE measurement from the same AHE/ISHE structure with 8 nm thick Py2. The insets of (a) and (b) show the measurement configurations. The magnetic field is applied parallel to Cu channel ($\pm x$ direction). (c) Illustration of symmetrical nonlocal spin signal (top), asymmetrical SHE/ISHE signal (middle), and their superposition (bottom).

There are two major features of the R_s versus B_x curve in Fig. 5.2 (a). One is the double-dips at the intermediate fields, which results from conventional nonlocal

spin signals. The other feature is the difference of ΔR_S = 0.71 mΩ between positive and negative high fields, which results from the ISHE. The nonlocal spin signal is symmetrical in the sense that the R_s values at large positive and negative fields are equal, as illustrated in the top portion of Fig. 5.2 (c). The SHE/ISHE signals are asymmetrical with different R_s values at large positive and negative fields, as shown in the middle portion of Fig. 5.2 (c). The overall R_s versus B_x curve is a superposition of the symmetrical nonlocal spin signal and the asymmetrical ISHE signal, as illustrated in the bottom portion of Fig. 5.2 (c). Therefore, the ISHE signal can be clearly separated from the conventional nonlocal spin signal.

It is useful to explain why nonlocal spin signals can be detected between the two ends of Py2 electrode, considering that the more standard practice is to measure it between the Py2 detector and the Cu channel. One can imagine that a nonlocal spin signal can be measured in the more standard way between the left end of Py2 and the Cu channel, referring to the inset of Fig. 5.2 (a). Similarly, another nonlocal spin signal can be measured between the right end of Py2 and the Cu channel. The two signals should be the same if the Cu/AlO_x/Py2 interface is a uniform tunnel barrier with large resistance. However, the directly evaporated AlO_x layer is less than ideally uniform and the resistance (typically 5 – 20 Ω for a 100 nm × 100 nm junction) is much lower than that of tunnel barriers. The signals measured from the left and the right are strongly affected by the interface conditions on the two sides of the junction, and typically have different values. Therefore, the signal measured between two ends of Py2, as in this work, is equivalent to a subtraction of the two different signals from left and right. More detailed analysis can be found in our previous work by Chen *et al.* [33].

The nonlocal spin signals are symmetrical because parallel states between the spin injector and spin detector are equivalently reached at large positive and negative fields. For SHE, however, the spin accumulation generated by the charge current is unaffected by a reversal of magnetic field, but the magnetization of the spin detector can be switched by the field. This apparent asymmetry of the system leads to the different (asymmetrical) R_s values at large positive and negative fields, which is the signature for SHE/ISHE in nonlocal structures [7, 28, 34, 35].

The R_s reaches negative values around the dips of the curve in Fig. 5.2 (a). This is routinely observed in a nonlocal measurement, which should have zero charge voltage background in an ideal situation. In experiments, the background voltage (or baseline) is often close to but not exactly zero [27, 36, 37]. Any spin-related signal change, either nonlocal spin signal or SHE/ISHE signal, is likely to swing the measured voltage between positive and negative R_s values. Such change of signal sign is an indication of clean nonlocal measurements rather than artifacts.

In previous work on ISHE in Py with Seebeck method, anomalous Nernst effects can be present and have to be explicitly separated or ruled out [14, 16, 38]. In this nonlocal method, the detected nonlocal voltage is locked to the base frequency of the sinusoidal excitation currents. Thermal effects are excluded, because thermal effects are proportional to the square of excitation current and therefore related to the voltage response at second harmonics.

Fig. 5.2 (b) shows the R_s versus B_x curves in the AHE measurement. Because of the Onsager reciprocal relations, the curve yields the same asymmetrical difference of $\Delta R_s = 0.71$ mΩ and the same magnitude of symmetrical nonlocal signals as compared to Fig. 5.2 (a). The nonlocal signal is inverted (peaks instead of dips)

because the electrical polarities on Py2 are inverted between the AHE and ISHE configurations. Following previously used conventions [7, 34, 35], the AHE/ISHE signal is defined as $\Delta R_{AHE} = \frac{\Delta R_S}{2}$ = 0.305 mΩ. For each Py2 thickness, 6 - 8 AHE/ISHE devices are measured for quantitative analysis.

At positive or negative large fields, the magnetization of Py2 electrode is oriented to opposite directions (± *x*). The transverse charge voltages between the top and bottom surfaces of Py2, induced by the AHE, have opposite signs for opposite magnetizations. However, the spin currents in the *z* direction from AHE should be the same. The majority and minority spins move in opposite directions but contribute positively to the transverse spin current. Reversed magnetization switches the roles of majority and minority spins, but will not alter the net spin current or spin accumulation. Therefore, the treatment of spin accumulation from AHE is identical to that of SHE, and we use the term AHE and SHE interchangeably throughout this chapter.

The resistance R_i of the Cu/AlO_x/Py2 interface is an important quantity to estimate the spin current through the interface and the current shunting effect by the Cu, and it can be measured directly in each AHE/ISHE structure. A current is applied between the right side of Py2 strip and the upper end of Cu channel, referring to Fig. 5.1 (b), and a voltage is detected between the left sides of Py2 and Py1 electrodes. Depending on the size of Cu/AlO_x/Py2 interface, R_i varies between 2 Ω and 130 Ω. The values of R_i for the substrate with 8 nm Py2 are summarized in Table 5.1.

A set (8 – 12) of supplementary NLSVs are used to determine spin polarization P of the Py1/AlO_x/Cu interface as well as λ_{Cu}, and ρ_{Cu}. Spin signals are measured as a function of center-to-center distance L' between two Py1 electrodes. Fig. 5.3 (a) shows

a R_s versus B_y curve of a NLSV at 5 K and the measurement configuration is illustrated in the inset. The high R_s value is associated with the parallel state between the injector and detector, the low R_s is associated with the anti-parallel state, and the difference ΔR_s is the NLSV spin signals. By fitting ΔR_s versus L' with the equation $\Delta R_s = (P^2 \rho_{Cu} \lambda_{Cu} / A_{Cu}') exp(-L'/\lambda_{Cu})$, we are able to extract P and λ_{Cu}. The cross-sectional area of the NLSV Cu channel is $A_{Cu}' = t_{Cu} w_{Cu}'$, where t_{Cu} = 110nm is the thickness and w_{Cu}' is the width. The values of L' and w_{Cu}' are measured by SEM for each device. The value of ρ_{Cu} is determined by sending a current through the Cu channel and detecting the voltage between two Py electrodes. An average ρ_{cu} is determined for devices on each sample substrate and the values are in the range of 1.8 – 2.6 μΩ•cm at 5 K. These values are reasonably small because of the large thickness of Cu. Fig. 5.3 (b) shows the ΔR_s versus L' plot, and the fitting yields P = 16.5% and λ_{Cu} = 900 nm at 5 K for the sample substrate with 8 nm Py2.

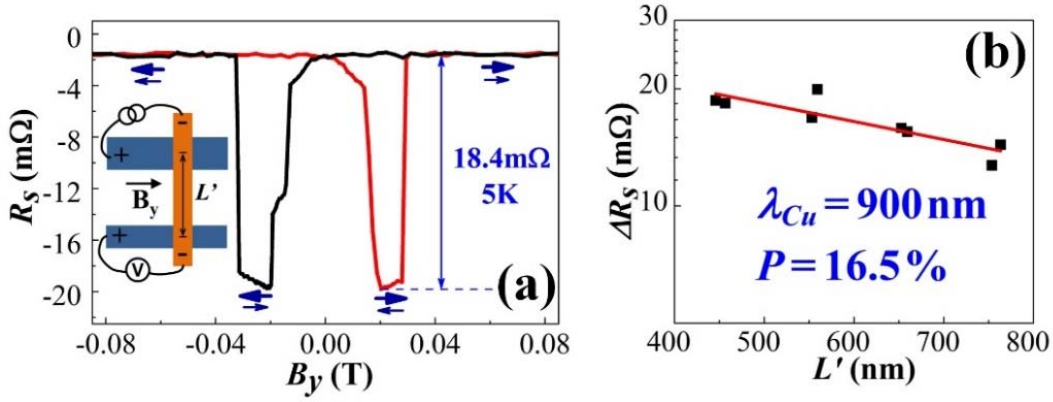

Figure 5.3: **:** (a) The R_s versus B_y curve at 5 K for a NLSV with magnetic field B_y applied along the $\pm y$ direction (shown in the inset). The blue arrows indicate the magnetization states of the injector and the detector. (b) The ΔR_s versus L' and a fit (solid red line) for NLSVs on the substrate with 8 nm thick Py2.

Four probe measurements are performed on 8 – 12 Py resistivity structures to determine the average ρ_{Py} of Py2 stripes, which have the same width as the Py2 in AHE/ISHE structures. The measured average ρ_{Py} as a function of the Py2 thickness t_{Py} is plotted in the inset of Fig. 5.4 (a) for 5 K and (b) for 295 K. The values of ρ_{Py} are between 150 μΩ•cm and 470 μΩ•cm, and decrease with an increasing t_{Py}. These values are 4 – 8 time larger than that of thick extended films. Reduction of either thickness or width leads to an increase of resistivity because of surface and edge defects. Therefore, it is important to measure resistivity on films that bear the same thickness and width as the AHE/ISHE structures.

5.4 Results and Analysis

In our previous work presented in chapter 4 [35], we developed an approach to quantitatively analyze the SHE/ISHE of mesoscopic Pt thin films in nonlocal structures. Spin accumulation in Cu channels and Pt thin films can be solved using one-dimensional spin diffusion equations with proper boundary conditions. Also, the spin current across the Cu/AlO_x/Pt interface and charge current/voltage shunting near the interface can be well quantified by the resistance R_i of the Cu/AlO_x/Pt interface.

Using the same method, the AHE/ISHE signal in Py can be expressed as:

$$\Delta R_s = 2\Delta R_{AHE} = \frac{\alpha'_H \gamma \chi \rho_{Py} P}{2w_{Py}} exp\left(-\frac{L}{\lambda_{Cu}}\right) \tag{5.1}$$

with the definition of the apparent spin Hall angle α'_H:

$$\alpha'_H(t_{Py}) = 2\alpha_H \left(\frac{\lambda_{Py}}{t_{Py}}\right)\left(\frac{exp(t_{Py}/\lambda_{Py})-1}{exp(t_{Py}/\lambda_{Py})+1}\right) \tag{5.2}$$

Here, the spin absorption coefficient $\gamma = 2R_{sCu}/(R_{sCu} + R_i)$ describes the amount of spin current across the Cu/AlO_x/Py2 interface, and L is the center-to-center distance between the Py1/AlO_x/Cu and Cu/AlO_x/Py2 junctions. The $R_{sCu} = \rho_{Cu}\lambda_{Cu}/A_{Cu}$ is the

Cu spin resistance with $A_{Cu} = t_{Cu}w_{Cu}$ being the Cu cross-sectional area. The factor $\chi = 4R_i/(4R_i + R_{Py})$ describes the shunting effect to the ISHE voltage or the AHE-inducing current by the highly conductive Cu through the Cu/AlO_x/Py2 interface [35]. The R_{Py} is defined as $R_{Py} = \rho_{Py}w_I/(w_{Py}t_{Py})$, where w_I is the width of Cu above the Cu/AlO_x/Py2 interface and w_{Py} is the overall width of the Py2 stripe. The values of w_{Cu}, w_{Py}, w_I and L are carefully measured by SEM for each AHE/ISHE device.

It is useful to consider two limiting cases for Eq. 5.2. When $t_{Py} \ll \lambda_{Py}$, $\alpha'_H = \alpha_H$ and the apparent spin Hall angle is a constant and equals to spin Hall angle. When $t_{Py} \gg \lambda_{Py}$, $\alpha'_H(t_{Py}) = 2\alpha_H\left(\frac{\lambda_{Py}}{t_{Py}}\right) = \frac{2\sigma_H\rho_{Py}\lambda_{Py}}{t_{Py}}$ and α'_H is inverse proportional to t_{Py}. Even in the case of varying ρ_{Py} with t_{Py}, the value of $\rho_{Py}\lambda_{Py}$ would still be a constant under the assumption of Elliot-Yafet spin relaxation mechanism [39, 40] with fixed spin relaxation rate. Without precise knowledge of λ_{Py}, we first calculate the α'_H from measured ΔR_{AHE} using Eq. 5.1. The obtained α'_H at 5 K for devices on the sample substrate with 8 nm Py2 are shown in Table 5.1. The average α'_H as a function of t_{Py} are shown in Fig. 5.4 (a) for 5 K and Fig. 5.4 (b) for 295 K. For both temperatures, a drastic decay is observed and indicates a short spin diffusion length ($\lambda_{Py} \ll t_{Py}$). The data is fitted well (solid lines) by a $\sim 1/t_{Py}$ dependence. We also attempted to fit the α'_H versus t_{Py} data by using Eq. 5.2 with an assumed λ_{Py} and a free fitting parameter α_H. When using λ_{Py} values lower than 1.0 nm, we could obtain equally good fits. When using $\lambda_{Py} = 1.2$ nm or higher, the fitted curves obviously deviate from experimental data. Therefore, we conclude that λ_{Py} is no more than 1.0 nm and much shorter than the film thickness (4 -12 nm). The short λ_{Py} is also consistent with high resistivity ρ_{Py} measured in mesoscopic Py films, because the

Elliott-Yafet model implies that $\rho\lambda$ is a constant. Note that the fabrication does not involve etching that may degrade the quality of Py films.

Table 5.1: Measured AHE/ISHE signals at 5 K, various parameters, and the obtained apparent spin Hall angle α_H' for 6 AHE/ISHE devices on the substrate with 8 nm thick Py2. The junction size refers to the length of the Cu channel right above the Py2/AlO_x/Cu junction.

Device	***Junction Size***	ΔR_s	L	R_i	χ	γ	α_H'
		mΩ	**nm**	**Ω**			
3-1	50nm	0.44	429	43.1	0.74	0.076	0.017
2-1	50nm	0.30	431	74.2	0.84	0.045	0.017
1-6	100nm	0.52	444	21.5	0.58	0.14	0.014
5-7	150nm	0.57	448	3.6	0.16	0.57	0.015
6-7	150nm	0.61	444	8.8	0.32	0.27	0.017
7-2	200nm	0.71	450	1.5	0.065	0.98	0.025

In the short λ_{Py} limit: the relation between α_H' and t_{Py} can be rewritten as $\alpha_H\lambda_{Py} = \sigma_H\rho_{Py}\lambda_{Py} = \alpha_H' t_{Py}/2$, which allows us to obtain $\alpha_H\lambda_{Py}$ or $\sigma_H\rho_{Py}\lambda_{Py}$ for each t_{Py} from experimental results, without any assumption of fixed values of σ_H, ρ_{Py}, or λ_{Py}, or their products. The obtained average values of $\alpha_H\lambda_{Py}$ are plotted as a function of t_{Py} in Fig. 5.4 (c), giving a constant value $\alpha_H\lambda_{Py} = (0.066 \pm 0.009)$ nm at 5 K and $\alpha_H\lambda_{Py} = (0.041 \pm 0.010)$ nm at 295 K. If λ_{Py} = 1.0 nm, the spin Hall angle α_H would be 0.066 at 5 K and 0.041 at 295 K. For shorter λ_{Py}, the α_H would be higher accordingly. If we continue to assume a constant $\rho_{Py}\lambda_{Py}$, the constant values of $\sigma_H\rho_{Py}\lambda_{Py}$ imply that σ_H is independent of thickness and resistivity. This is consistent with the intrinsic or side jump mechanism in spin Hall or anomalous Hall effects [41].

For skew scattering mechanism, the σ_H is inversely proportional to electrical resistivity. The intrinsic or side jump mechanism is expected to dominate in the moderately dirty conductors with relatively high resistivity.

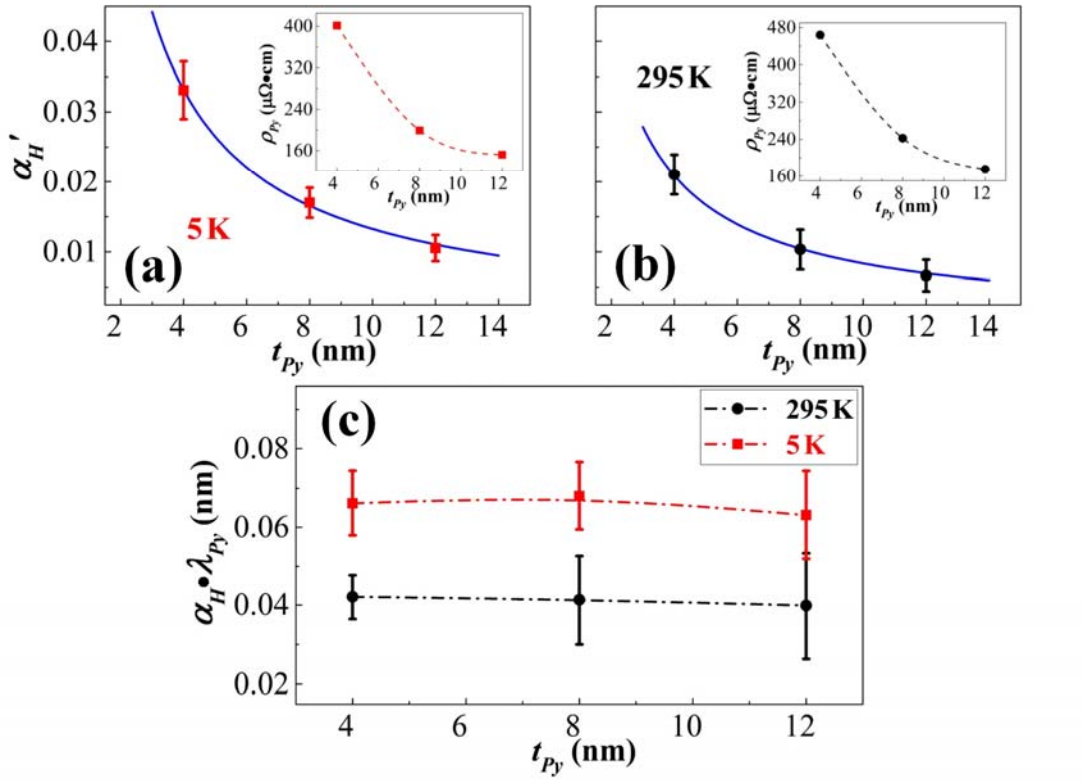

Figure 5.4: The apparent spin Hall α_H' as a function of Py thickness (a) at 5K and (b) at 295K and fits (solid lines). The insets show the Py resistivity ρ_{Py} as a function of Py thickness. (c) The obtained values of $\alpha_H\ \lambda_{Py}$ as a function of t_{Py} at 5 K (red squares) and 295 K (black dots). The dash-dot line is a guidance for the eyes.

Previously, we explored and analyzed the SHE/ISHE in mesoscopic Pt thin films at 5 K using the same method [35]. In Fig. 5.5, we compare the values of $\alpha_H\lambda$ at

5 K for Pt and Py films at different thicknesses. At lower thickness (4 nm), the ratio of two values is $(\alpha_H\lambda)_{Py}/(\alpha_H\lambda)_{Pt}$ ≈0.47; At higher thickness (12 nm), the ratio is 0.93, indicating that the spin current from the AHE in mesoscopic Py films is comparable to that from the SHE in mesoscopic Pt films.

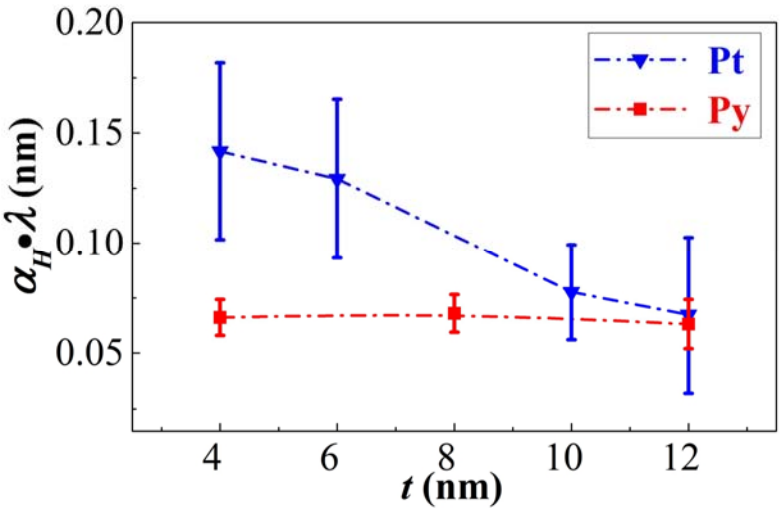

Figure 5.5: A comparison of $\alpha_H\lambda$ between mesoscopic Py and Pt films as a function of film thickness at 5 K.

The value of $\alpha_H\lambda_{Py}$ = 0.041 nm at 295 K can be compared to results obtained on Py/YIG bilayer structures. By using spin Seebeck effects and ISHE, Miao *et al.* [14] reported $\alpha_H = 0.005$ and $\lambda_{Py} = 2.5$ nm, yielding $\alpha_H\lambda_{Py} = 0.0125$ nm. Wang *et al.* [15] used the spin pumping measurements and obtained $\alpha_H = 0.02$ and $\lambda_{Py} = 1.7$ nm, thereby giving $\alpha_H\lambda_{Py} = 0.034$ nm. These values are lower than ours but are on the same order of magnitude.

5.5 Conclusion

In summary, large spin accumulation caused by Anamalous Hall effect has been detected electrically using a nonlocal method in mesoscopic NiFe (Py) thin films. Its reciprocal effects, the inverse spin Hall effects, are also generated and detected. A systematic approach is used to quantify the effects and obtain the product of spin Hall angle and the spin diffusion length: $\alpha_H \lambda_{Py}$= (0.066 ± 0.009) nm at 5 K and (0.041 ± 0.010) nm at 295 K. These values are independent of film thickness and resistivity, and are comparable to that of mesoscopic Pt films.

REFERENCES

[1] M. I. Dyakonov and V. I. Perel, JETP Letters **13**, 467 (1971).

[2] J. E. Hirsch, Physical Review Letters **83**, 1834 (1999).

[3] S. F. Zhang, Physical Review Letters **85**, 393 (2000).

[4] Y. K. Kato, R. C. Myers, A. C. Gossard, and D. D. Awschalom, Science **306**, 1910 (2004).

[5] S. O. Valenzuela and M. Tinkham, Nature **442**, 176 (2006).

[6] E. Saitoh, M. Ueda, H. Miyajima, and G. Tatara, Applied Physics Letters **88**, 182509 (2006).

[7] T. Kimura, Y. Otani, T. Sato, S. Takahashi, and S. Maekawa, Physical Review Letters **98**, 156601 (2007).

[8] K. Ando, S. Takahashi, K. Harii, K. Sasage, J. Ieda, S. Maekawa, and E. Saitoh, Physical Review Letters **101**, 036601 (2008).

[9] K. Ando, Y. Kajiwara, S. Takahashi, S. Maekawa, K. Takemoto, M. Takatsu, and E. Saitoh, Physical Review B **78**, 014413 (2008).

[10] O. Mosendz, J. E. Pearson, F. Y. Fradin, G. E. W. Bauer, S. D. Bader, and A. Hoffmann, Physical Review Letters **104**, 046601 (2010).

[11] I. M. Miron, G. Gaudin, S. Auffret, B. Rodmacq, A. Schuhl, S. Pizzini, J. Vogel, and P. Gambardella, Nature Matererals **9**, 230 (2010).

[12] L. Q. Liu, T. Moriyama, D. C. Ralph, and R. A. Buhrman, Physical Review Letters **106**, 036601 (2011).

[13] L. Q. Liu, O. J. Lee, T. J. Gudmundsen, D. C. Ralph, and R. A. Buhrman, Physical Review Letters **109**, 096602 (2012).

[14] B. F. Miao, S. Y. Huang, D. Qu, and C. L. Chien, Phys. Rev. Lett. Physical Review Letters **111**, 066602 (2013).

[15] H. L. Wang, C. H. Du, P. C. Hammel, and F. Y. Yang, Applied Physics Letters **104**, 202405 (2014).

[16] H. Wu, C. H. Wan, Z. H. Yuan, X. Zhang, J. Jiang, Q. T. Zhang, Z. C. Wen, and X. F. Han, Physical Review B **92**, 054404 (2015).

[17] T. Taniguchi, J. Grollier, and M. D. Stiles, Physical Review Applied **3**, 044001 (2015).

[18] I. Tudosa, arXiv:1702.07153 (2017).

[19] G. J. Dolan, Applied Physics Letters **31**, 337 (1977).

[20] M. Johnson and R. H. Silsbee, Physical Review Letters **55**, 1790 (1985).

[21] F. J. Jedema, A. T. Filip, and B. J. van Wees, Nature **410**, 345 (2001).

[22] F. J. Jedema, H. B. Heersche, A. T. Filip, J. J. A. Baselmans, and B. J. van Wees, Nature **416**, 713 (2002).

[23] S. O. Valenzuela and M. Tinkham, Applied Physics Letters **85**, 5914 (2004).

[24] T. Kimura, J. Hamrle, Y. Otani, K. Tsukagoshi, and Y. Aoyagi, Applied Physics Letters **85**, 3501 (2004).

[25] Y. Ji, A. Hoffmann, J. S. Jiang, and S. D. Bader, Applied Physics Letters **85**, 6218 (2004).

[26] Y. Ji, A. Hoffmann, J. E. Pearson, and S. D. Bader, Applied Physics Letters **88**, 052509 (2006).

[27] X. J. Wang, H. Zou, L. E. Ocola, and Y. Ji, Applied Physics Letters **95**, 022519 (2009).

[28] S. H. Chen, C. Qin, and Y. Ji, Applied Physics Letters **105**, 082402 (2014).

[29] H. Zou, X. J. Wang, and Y. Ji, Journal of Vacuum Science and Technology B **28**, 1314 (2010).

[30] Y. Fukuma, L. Wang, H. Idzuchi, and Y. Otani, Applied Physics Letters **97**, 012507 (2010).

[31] Y. J. Cai, Y. M. Luo, C. Qin, S. H. Chen, Y. Z. Wu, and Y. Ji, Journal of Magnetism and Magnetic Materials **405**, 145 (2016).

[32] Y. J. Cai, Y. M. Luo, C. Zhou, C. Qin, S. H. Chen, Y. Z. Wu, and Y. Ji, Journal of Physics D: Applied Physics **49**, 185003 (2016).

[33] S. H. Chen, C. Qin, and Y. Ji, Journal of Applied Physics **118**, 033901 (2015).

[34] L. Vila, T. Kimura, and Y. Otani, Physical Review Letters **99**, 226604 (2007).

[35] C. Qin, Y. M. Luo, C. Zhou, Y. J. Cai, M. W. Jia, S. H. Chen, Y. Z. Wu, and Y. Ji, Journal of Physics D: Applied Physics **49**, 415002 (2016).

[36] M. Johnson and R. H. Silsbee, Physical Review B **76**, 153107 (2007).

[37] X. J. Wang, H. Zou, and Y. Ji, Physical Review B **81**, 104409 (2010).

[38] D. Tian, Y. F. Li, D. Qu, S. Y. Huang, X. F. Jin, and C. L. Chien, Physical Review B **94**, 020403 (2016)

[39] R. J. Elliott, Physical Review **96**, 266 (1954).

[40] Y. Yafet, Physics Letters A **98**, 287 (1983).

[41] A. Hoffmann, IEEE Transactions on Magnetics **49**, 5172 (2013).

Chapter 6

CONCLUSION AND OUTLOOK

In this dissertation, we reported the electrical detection of SHE in Pt thin film and spin accumulation generated by AHE in Py thin film using the mesoscopic nonlocal structure. With the unique design of the lateral geometry, we are able to measure both SHE and ISHE signals in Pt by simply swapping current and voltage terminals. Also, the signals of the spin accumulation due to AHE and ISHE in Py are well separated from conventional spin signals, therefore can be directly detected using nonlocal method. Furthermore, we presented a quantitative method to characterize the SHE effectively. We can accurately determine the product of spin Hall angle α_H and spin diffusion length λ, and use the product value as a figure of merit to quantify the SHE because it is less prone to errors than the individual values of α_H and λ. A substantial value of $\alpha_H\lambda$ indicates an efficient spin Hall process.

Since the observation of SHEs in semiconductor [1], extensive studies have been carried out to explore the materials with large SHE. The most commonly explored ones are 4d and 5d transition metals with heavy elements. Pt, Au and Pd are the examples among the non-magnetic transition metals, as well as Ta and W [2, 3] that have opposite spin Hall angles compared to Pt. In addition to the transition metals, some alloys also show large SHEs, such as Bi-doped Cu [4], Ir-doped Cu [5] and Au-Cu alloy [6]. It is important to quantify the SHE of various materials correctly, therefore the quantitative study of SHE using nonlocal structures presented in this dissertation provides an effective way to analyze the SHE. At the same time, the

nonlocal electrical detection method makes it possible to explore the spin current generated by AHE in ferromagnetic materials directly.

In recent years, the applications of SHE have been actively pursued in spintronic technology. For a pure spin current, it only carries the flow of spin angular momentum without a charge current. Therefore, the electrical detection of a pure spin current is non-trivial. By utilizing the feature of ISHE, the spin Hall material can be used as a sensitive detector of the spin current, which converts a pure spin current into a transverse charge current. The presence of the pure spin current in ferromagnetic materials generated either by the spin pumping method with microwave or the spin Seebeck effect under a thermal gradient cannot be directly detected. But with the ferromagnet/heavy non-magnetic metal bilayer structures as we have mentioned in Section 2.3.1, the pure spin current in ferromagnetic layer is absorbed into the adjacent heavy non-magnetic layer, and then converted to a transverse charge voltage which is electrically detectable [7-9].

The most fascinating feature of SHE is the spin Hall effect-induced spin transfer torque (SHE-STT) switching. It has been demonstrated by Miron *et al.* [10] and Liu *et al.* [2, 11] in the bilayer system, the pure spin current induced by SHE is large enough to switch the magnetic moment of the adjacent ferromagnetic layer. Based on the SHE-STT switching, Liu *et al.* designed a three-terminal spin Hall effect device, where a MTJ nanopillar is patterned on the top of the Ta layer, as illustrated in Fig. 6.1 (a) [2]. When a charge current is applied through the Ta layer along the long axis, a pure spin current is induced in the vertical direction, causing a spin accumulation on the surface of the Ta layer. The spin accumulation is absorbed into the bottom ferromagnetic layer of the MTJ, and therefore exerts a spin torque to

switch the magnetization direction of the bottom layer. The MTJ nanopillar can be manipulated between parallel and anti-parallel magnetization configurations for the top and bottom ferromagnetic layers, exhibiting either a low or high TMR value shown as Fig. 6.1 (b). The process of a conventional two-terminal spin transfer torque (STT) switching device is different, where the magnetization switching is related to the injected charge current polarized by the fixed ferromagnetic layer. Compared to the conventional STT device, the SHE-STT device doesn't involve a direct injection of the charge current through the tunnel junction. Thus, a lower switching current and better thermal stability are expected in the SHE-STT devices. This may enable a new direction in the design of STT-magnetic random access memories (STT-MRAM) by integrating the SHE-STT device into the structure.

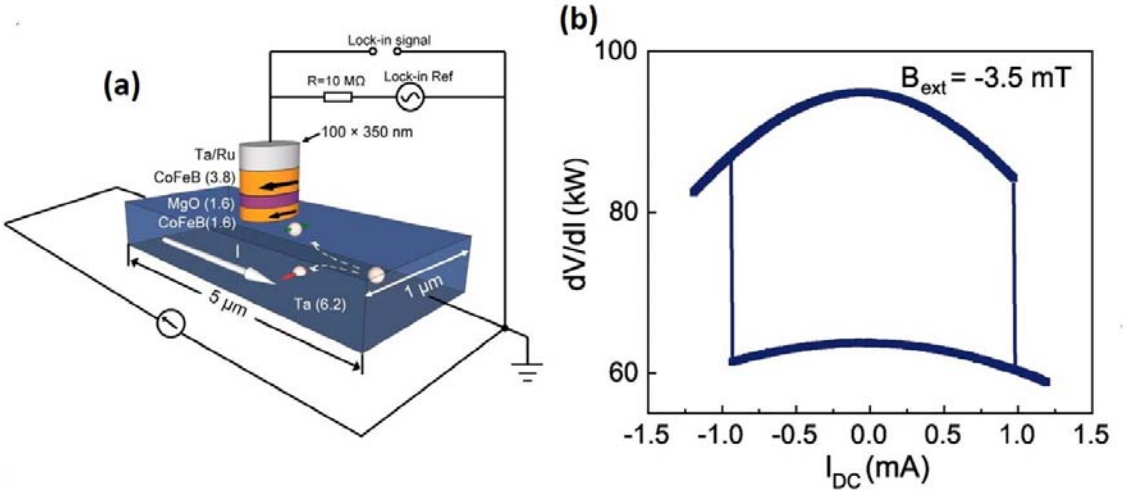

Figure 6.1: (a) Illustration of the three-terminal SHE device and the circuit for measurements. (b) TMR of the MTJ device as a function of applied charge current along the long axis of the Ta layer. Reprinted with permission from Ref. [2].

REFERENCES

[1] Y. K. Kato, R. C. Myers, A. C. Gossard and D. D. Awschalom, Science **306** (5703), 1910 (2004).

[2] L. Q. Liu, C. F. Pai, Y. Li, H. W. Tseng, D. C. Ralph and R. A. Buhrman, Science **336** (6081), 555 (2012).

[3] C. F. Pai, L. Q. Liu, Y. Li, H. W. Tseng, D. C. Ralph and R. A. Buhrman, Applied Physics Letters **101** (12), 4 (2012).

[4] Y. Niimi, Y. Kawanishi, D. H. Wei, C. Deranlot, H. X. Yang, M. Chshiev, T. Valet, A. Fert and Y. Otani, Physical Review Letters **109** (15), 5 (2012).

[5] Y. Niimi, M. Morota, D. H. Wei, C. Deranlot, M. Basletic, A. Hamzic, A. Fert and Y. Otani, Physical Review Letters **106** (12), 126601 (2011).

[6] J. Wu, L. K. Zou, T. Wang, Y. P. Chen, J. W. Cai, J. Hu and J. Q. Xiao, IEEE Transactions on Magnetics **52** (7), 4 (2016).

[7] E. Saitoh, M. Ueda, H. Miyajima and G. Tatara, Applied Physics Letters **88** (18), 182509 (2006).

[8] K. Ando, Y. Kajiwara, S. Takahashi, S. Maekawa, K. Takemoto, M. Takatsu and E. Saitoh, Physical Review B **78** (1), 014413 (2008).

[9] K. Uchida, S. Takahashi, K. Harii, J. Ieda, W. Koshibae, K. Ando, S. Maekawa and E. Saitoh, Nature **455** (7214), 778 (2008).

[10] I. M. Miron, G. Gaudin, S. Auffret, B. Rodmacq, A. Schuhl, S. Pizzini, J. Vogel and P. Gambardella, Nature Materials **9** (3), 230 (2010).

[11] L. Q. Liu, O. J. Lee, T. J. Gudmundsen, D. C. Ralph and R. A. Buhrman, Physical Review Letters **109** (9), 096602 (2012).

Appendix

REPRINT PERMISSION LETTERS

Reprint Permission for Figure 2.6 (a):

AMERICAN PHYSICAL SOCIETY LICENSE TERMS AND CONDITIONS

Sep 28, 2017

This Agreement between Chuan Qin ("You") and American Physical Society ("American Physical Society") consists of your license details and the terms and conditions provided by American Physical Society and Copyright Clearance Center.

License Number	4197900112409
License date	Sep 28, 2017
Licensed Content Publisher	American Physical Society
Licensed Content Publication	Physical Review Letters
Licensed Content Title	Interfacial charge-spin coupling: Injection and detection of spin magnetization in metals
Licensed Content Author	Mark Johnson and R. H. Silsbee
Licensed Content Date	Oct 21, 1985
Licensed Content Volume	55
Type of Use	Thesis/Dissertation
Requestor type	Student
Format	Electronic
Portion	image/photo
Number of images/photos requested	1
Portion description	Fig. 1 (c)
Rights for	Main product
Duration of use	Life of Current Edition
Creation of copies for the disabled	no
With minor editing privileges	no
For distribution to	Worldwide
In the following language(s)	Original language of publication
With incidental promotional use	no
The lifetime unit quantity of new product	0 to 499
The requesting person/organization is:	Chuan Qin

Order reference number	
Title of your thesis / dissertation	QUANTITATIVE STUDY OF SPIN HALL EFFECTS IN MESOSCOPIC THIN FILMS
Expected completion date	Dec 2017
Expected size (number of pages)	120
Requestor Location	Chuan Qin
Total	0.00 USD

Reprint Permission for Figure 2.6 (b):

NATURE PUBLISHING GROUP LICENSE TERMS AND CONDITIONS

Sep 28, 2017

This Agreement between Chuan Qin ("You") and Nature Publishing Group ("Nature Publishing Group") consists of your license details and the terms and conditions provided by Nature Publishing Group and Copyright Clearance Center.

License Number	4197900861775
License date	Sep 28, 2017
Licensed Content Publisher	Nature Publishing Group
Licensed Content Publication	Nature
Licensed Content Title	Electrical spin injection and accumulation at room temperature in an all-metal mesoscopic spin valve
Licensed Content Author	F. J. Jedema, A. T. Filip and B. J. van Wees
Licensed Content Date	Mar 15, 2001
Licensed Content Volume	410
Licensed Content Issue	6826
Type of Use	reuse in a dissertation / thesis
Requestor type	academic/educational
Format	electronic
Portion	figures/tables/illustrations
Number of figures/tables/illustrations	1
Figures	Figure 1
Author of this NPG article	no
Your reference number	
Title of your thesis / dissertation	QUANTITATIVE STUDY OF SPIN HALL EFFECTS IN MESOSCOPIC THIN FILMS
Expected completion date	Dec 2017
Estimated size (number of pages)	120
Requestor Location	Chuan Qin
Total	0.00 USD

Reprint Permission for Figure 2.8:

AIP PUBLISHING LLC LICENSE TERMS AND CONDITIONS

Oct 04, 2017

This Agreement between Chuan Qin ("You") and AIP Publishing LLC ("AIP Publishing LLC") consists of your license details and the terms and conditions provided by AIP Publishing LLC and Copyright Clearance Center.

License Number	4201980454787
License date	Oct 04, 2017
Licensed Content Publisher	AIP Publishing LLC
Licensed Content Publication	Applied Physics Letters
Licensed Content Title	The origin of high surface spin-flip rate in metallic nonlocal spin valves
Licensed Content Author	Han Zou, Yi Ji
Licensed Content Date	Aug 20, 2012
Licensed Content Volume	101
Licensed Content Issue	8
Type of Use	Thesis/Dissertation
Requestor type	Student
Format	Electronic
Portion	Figure/Table
Number of figures/tables	1
Title of your thesis / dissertation	QUANTITATIVE STUDY OF SPIN HALL EFFECTS IN MESOSCOPIC THIN FILMS
Expected completion date	Dec 2017
Estimated size (number of pages)	120
Requestor Location	Chuan Qin
Total	0.00 USD

Reprint Permission for Figure 2.9 (a):

AIP PUBLISHING LLC LICENSE TERMS AND CONDITIONS

Oct 04, 2017

This Agreement between Chuan Qin ("You") and AIP Publishing LLC ("AIP Publishing LLC") consists of your license details and the terms and conditions provided by AIP Publishing LLC and Copyright Clearance Center.

License Number	4201980692332
License date	Oct 04, 2017
Licensed Content Publisher	AIP Publishing LLC
Licensed Content Publication	Applied Physics Letters
Licensed Content Title	Conversion of spin current into charge current at room temperature: Inverse spin-Hall effect
Licensed Content Author	E. Saitoh, M. Ueda, H. Miyajima, et al
Licensed Content Date	May 1, 2006
Licensed Content Volume	88
Licensed Content Issue	18
Type of Use	Thesis/Dissertation
Requestor type	Student
Format	Electronic
Portion	Figure/Table
Number of figures/tables	1
Title of your thesis / dissertation	QUANTITATIVE STUDY OF SPIN HALL EFFECTS IN MESOSCOPIC THIN FILMS
Expected completion date	Dec 2017
Estimated size (number of pages)	120
Requestor Location	Chuan Qin
Total	0.00 USD

Reprint Permission for Figure 2.9 (b):

AMERICAN PHYSICAL SOCIETY LICENSE TERMS AND CONDITIONS

Oct 04, 2017

This Agreement between Chuan Qin ("You") and American Physical Society ("American Physical Society") consists of your license details and the terms and conditions provided by American Physical Society and Copyright Clearance Center.

License Number	4201980888268
License date	Oct 04, 2017
Licensed Content Publisher	American Physical Society
Licensed Content Publication	Physical Review Letters
Licensed Content Title	Electric Manipulation of Spin Relaxation Using the Spin Hall Effect
Licensed Content Author	K. Ando et al.
Licensed Content Date	Jul 18, 2008
Licensed Content Volume	101
Type of Use	Thesis/Dissertation
Requestor type	Student
Format	Electronic
Portion	image/photo
Number of images/photos requested	1
Portion description	Figure 1
Rights for	Main product
Duration of use	Life of Current Edition
Creation of copies for the disabled	no
With minor editing privileges	no
For distribution to	Worldwide
In the following language(s)	Original language of publication
With incidental promotional use	no
The lifetime unit quantity of new product	0 to 499
The requesting person/organization is:	Chuan Qin
Order reference number	
Title of your thesis / dissertation	QUANTITATIVE STUDY OF SPIN HALL EFFECTS IN MESOSCOPIC THIN FILMS
Expected completion date	Dec 2017
Expected size (number of pages)	120
Total	0.00 USD

Reprint Permission for Figure 2.10:

AMERICAN PHYSICAL SOCIETY LICENSE

TERMS AND CONDITIONS

Oct 26, 2017

This Agreement between Chuan Qin ("You") and American Physical Society ("American Physical Society") consists of your license details and the terms and conditions provided by American Physical Society and Copyright Clearance Center.

License Number	4216730823110
License date	Oct 26, 2017
Licensed Content Publisher	American Physical Society
Licensed Content Publication	Physical Review Letters
Licensed Content Title	Current-Induced Switching of Perpendicularly Magnetized Magnetic Layers Using Spin Torque from the Spin Hall Effect
Licensed Content Author	Luqiao Liu et al.
Licensed Content Date	Aug 29, 2012
Licensed Content Volume	109
Type of Use	Thesis/Dissertation
Requestor type	Student
Format	Electronic
Portion	image/photo
Number of images/photos requested	1
Portion description	Fig. 1
Rights for	Main product
Duration of use	Life of Current Edition
Creation of copies for the disabled	no
With minor editing privileges	no
For distribution to	Worldwide
In the following language(s)	Original language of publication
With incidental promotional use	no
The lifetime unit quantity of new product	0 to 499
The requesting person/organization is:	Chuan Qin
Order reference number	
Title of your thesis / dissertation	QUANTITATIVE STUDY OF SPIN HALL EFFECTS IN MESOSCOPIC THIN FILMS
Expected completion date	Dec 2017
Expected size (number of pages)	120
Requestor Location	Chuan Qin 104 THE GRN RM 217 NEWARK, DE 19716 United States Attn: Chuan Qin
Billing Type	Invoice
Billing Address	Chuan Qin 104 THE GRN RM 217 NEWARK, DE 19716 United States Attn: Chuan Qin
Total	0.00 USD

Reprint Permission for Figure 2.11:

NATURE PUBLISHING GROUP LICENSE TERMS AND CONDITIONS

Oct 04, 2017

This Agreement between Chuan Qin ("You") and Nature Publishing Group ("Nature Publishing Group") consists of your license details and the terms and conditions provided by Nature Publishing Group and Copyright Clearance Center.

License Number	4201981396372
License date	Oct 04, 2017
Licensed Content Publisher	Nature Publishing Group
Licensed Content Publication	Nature
Licensed Content Title	Direct electronic measurement of the spin Hall effect
Licensed Content Author	S. O. ValenzuelaandM. Tinkham
Licensed Content Date	Jul 13, 2006
Licensed Content Volume	442
Licensed Content Issue	7099
Type of Use	reuse in a dissertation / thesis
Requestor type	academic/educational
Format	electronic
Portion	figures/tables/illustrations
Number of figures/tables/illustrations	1
High-res required	no
Figures	Figure 3
Author of this NPG article	no
Your reference number	
Title of your thesis / dissertation	QUANTITATIVE STUDY OF SPIN HALL EFFECTS IN MESOSCOPIC THIN FILMS
Expected completion date	Dec 2017
Estimated size (number of pages)	120
Requestor Location	Chuan Qin 104 THE GRN RM 217
Total	0.00 USD

Reprint Permission for Figure 2.12:

AMERICAN PHYSICAL SOCIETY LICENSE TERMS AND CONDITIONS

Oct 04, 2017

This Agreement between Chuan Qin ("You") and American Physical Society ("American Physical Society") consists of your license details and the terms and conditions provided by American Physical Society and Copyright Clearance Center.

License Number	4201990224899
License date	Oct 04, 2017
Licensed Content Publisher	American Physical Society
Licensed Content Publication	Physical Review Letters
Licensed Content Title	Room-Temperature Reversible Spin Hall Effect
Licensed Content Author	T. Kimura et al.
Licensed Content Date	Apr 12, 2007
Licensed Content Volume	98
Type of Use	Thesis/Dissertation
Requestor type	Student
Format	Electronic
Portion	image/photo
Number of images/photos requested	3
Portion description	Figure 1(c) and (e), Figure 2(b), Figure 4(b)
Rights for	Main product
Duration of use	Life of Current Edition
Creation of copies for the disabled	no
With minor editing privileges	no
For distribution to	Worldwide
In the following language(s)	Original language of publication
With incidental promotional use	no
The lifetime unit quantity of new product	0 to 499
The requesting person/organization is:	Chuan Qin
Order reference number	
Title of your thesis / dissertation	QUANTITATIVE STUDY OF SPIN HALL EFFECTS IN MESOSCOPIC THIN FILMS
Expected completion date	Dec 2017
Expected size (number of pages)	120
Requestor Location	Chuan Qin 104 THE GRN RM 217
Total	0.00 USD

Reprint Permission for Figure 2.13:

AMERICAN PHYSICAL SOCIETY LICENSE TERMS AND CONDITIONS

Oct 04, 2017

This Agreement between Chuan Qin ("You") and American Physical Society ("American Physical Society") consists of your license details and the terms and conditions provided by American Physical Society and Copyright Clearance Center.

License Number	4201990349434
License date	Oct 04, 2017
Licensed Content Publisher	American Physical Society
Licensed Content Publication	Physical Review Letters
Licensed Content Title	Inverse Spin Hall Effect in a Ferromagnetic Metal
Licensed Content Author	B. F. Miao et al.
Licensed Content Date	Aug 5, 2013
Licensed Content Volume	111
Type of Use	Thesis/Dissertation
Requestor type	Student
Format	Electronic
Portion	image/photo
Number of images/photos requested	1
Portion description	Figure 3(a) and (b)
Rights for	Main product
Duration of use	Life of Current Edition
Creation of copies for the disabled	no
With minor editing privileges	no
For distribution to	Worldwide
In the following language(s)	Original language of publication
With incidental promotional use	no
The lifetime unit quantity of new product	0 to 499
The requesting person/organization is:	Chuan Qin
Order reference number	
Title of your thesis / dissertation	QUANTITATIVE STUDY OF SPIN HALL EFFECTS IN MESOSCOPIC THIN FILMS
Expected completion date	Dec 2017
Expected size (number of pages)	120
Requestor Location	Chuan Qin 104 THE GRN RM 217
Total	0.00 USD

Reprint Permission for Figure 6.1:

THE AMERICAN ASSOCIATION FOR THE ADVANCEMENT OF SCIENCE LICENSE TERMS AND CONDITIONS

Oct 04, 2017

This Agreement between Chuan Qin ("You") and The American Association for the Advancement of Science ("The American Association for the Advancement of Science") consists of your license details and the terms and conditions provided by The American Association for the Advancement of Science and Copyright Clearance Center.

License Number	4201981198182
License date	Oct 04, 2017
Licensed Content Publisher	The American Association for the Advancement of Science
Licensed Content Publication	Science
Licensed Content Title	Spin-Torque Switching with the Giant Spin Hall Effect of Tantalum
Licensed Content Author	Luqiao Liu,Chi-Feng Pai,Y. Li,H. W. Tseng,D. C. Ralph,R. A. Buhrman
Licensed Content Date	May 4, 2012
Licensed Content Volume	336
Licensed Content Issue	6081
Volume number	336
Issue number	6081
Type of Use	Thesis / Dissertation
Requestor type	Scientist/individual at a research institution
Format	Print and electronic
Portion	Figure
Number of figures/tables	1
Order reference number	
Title of your thesis / dissertation	QUANTITATIVE STUDY OF SPIN HALL EFFECTS IN MESOSCOPIC THIN FILMS
Expected completion date	Dec 2017
Estimated size(pages)	120
Requestor Location	Chuan Qin 104 THE GRN RM 217
Total	0.00 USD